Monolithically integrated tuneable slotted Fabry-Pérot laser, wavelength monitor and modulator

Prasanna Ramaswamy
M. Sc.
112224005

NATIONAL UNIVERSITY OF IRELAND, CORK

School of Engineering

Tyndall National Institute

Thesis submitted for the degree of Doctor of Philosophy

September 2019

Supervisors: Mr Brian Corbett
Dr Brendan Roycroft

Contents

List of Figures

List of Tables

I, Prasanna Ramaswamy, certify that this thesis is my own work and I have not obtained a degree in University College Cork or elsewhere on the basis of the work submitted in this thesis. All external references and sources are clearly acknowledged and identified within the contents. I have read and understood the regulations of University College Cork concerning plagiarism.

Prasanna Ramaswamy

Acknowledgements

The journey of doing a PhD has been an immensely enriching and a great learning experience for me. I must begin this section by thanking my supervisors Mr. Brian Corbett and Dr. Brendan Roycroft for accepting me into their group, providing me with the best possible tools and environment to learn and try new things, for always being available for discussion and guidance, and for being very compassionate outside of work. I could not have asked for better supervisors for my PhD.

My sincere thanks also to Dr. Michael Gleeson and Dr. James O'Callaghan for being my mentors in the initial days of my cleanroom training without which I could not have fabricated the devices in this thesis. I am very grateful to Tyndall National Institute, in general, for providing me with great a great research environment, and great set of people to be around both in terms of technical experience and a jolly atmosphere.

A huge thank you to all my friends, especially Annamaria Fordymacka, Charles Perumal, Meysam Khanghah, Natalia Cañasestrada, Rohini Swaminathan and Stefano Facchin for helping me with (and riding along with me) the ups and downs of our PhDs and life in the past few years.

I wish to thank the colleagues at my current place of employment - Effect Photonics, especially Astrid Engel and Boudewijn Docter for the support and encouragement in seeing my thesis through to the finish line.

I would also like to acknowledge Science Foundation Ireland (SFI) and the EU FP7 project DISCUS for funding this work.

Finally, and most importantly, this work would not have been possible without the support that I received from my family - motivation and prayers from my parents, and constant companionship and a shoulder to lean on from my wife, Arundhathi, who saw me through all the stages excitement, hope and despair during this journey. Thank you!

Abstract

To aid the ever-increasing demand for data bandwidth, tuneable lasers will be a key requirement in transmitter modules of next-generation optical communication networks for data transmission in access networks. The lasers need to be wavelength-stabilised and cost is a critical factor since they will be widely used in consumer products. Currently used tuneable lasers in the downstream direction in access networks are too expensive to be also used widely in consumer products (upstream), and current designs for integrated wavelength monitors use passive waveguides made using spatially selective bandgap engineering techniques which are not cost-effective and make integration with a laser challenging.

This thesis demonstrates a low-cost tuneable transmitter module using a slotted Fabry-Pérot laser, monolithically integrated with a modulator, wavelength monitor and a semiconductor optical amplifier (SOA). The laser is based on a 3-section slotted Fabry-Pérot design and has a discrete tuning range of about 20nm which covers half the C-band. The wavelength can be further fine-tuned by adjusting the temperature between 16-22^{0}C with a sensitivity of approximately 0.1nm/^{0}C. The modulator is an absorbing section with Ground-Signal-Ground (GSG) pads that is capable of delivering data rates of up to 10 Gb/s with a peak-to-peak driving voltage of 1V using Non-return-to-zero on-off-keying (NRZ-OOK) modulation. Error free transmission was achieved for distances up to 50km of single mode fibre. The module also incorporates an integrated semiconductor optical amplifier (SOA) which provides an optical gain control of up to 20dB with a drive current of 30mA. The wavelength monitor has a linear working range of approximately 25nm and can provide a sensitivity of 13-15GHz ($\sim$0.1nm). It employs the same epitaxial structure as the tuneable laser, thus requiring no regrowth, making monolithic integration possible. Along with the fact that the slots required for tuning of the laser are fabricated in the same step as the ridge waveguide, presenting no additional complexity during the fabrication process, makes the whole transmitter module low-cost and compatible for use in Optical Network Units (ONUs) in the consumers' premises in a Fibre-to-the-Home (FTTH) scenario in access networks.

The thesis also explores the challenges of integration such as electrical, optical and thermal crosstalk between the various active components within a single device and suggests design considerations that will help mitigate this crosstalk. For future work, the performance of the modulator section could be enhanced by the use of quantum well intermixing and also reducing its pad capacitance by introducing high-k dielectrics. After fabrication, the common substrate could be stripped off from underneath the entire device and the various components could be 'printed' separately on other substrates and optically connected via passive waveguides using novel transfer-printing technology, which could help reduce crosstalk further by eliminating substrate coupling.

Chapter 1

Introduction

The internet plays a major role in connecting the world. With the recent advances in hand-held device technologies and growing popularity of video streaming services, the demand for data bandwidth is increasing rapidly. It is projected that in the next five years, global internet traffic will grow at a Compound Annual Growth Rate (CAGR) of 24% (Fig. 1.1) and by 2021, the number of connected devices will be three times the world population[1]. Optical networking is at the core of today's long-haul communication systems. This increase in demand can only be met by advances in the underlying optical transceiver designs and in turn the semiconductor laser technology that goes into making the transceivers. Next-generation network standards are looking towards being adaptive and reconfigurable on-the-fly and this translates into wavelength-tuneable components being deployed at the far end of the access network arms such as in 5G towers for data back-haul and at consumers' premises. There is a great need, given the location and volume of these components, for low-cost technological solutions. This thesis presents a low-cost upstream transmitter and the challenges associated with realising the same.

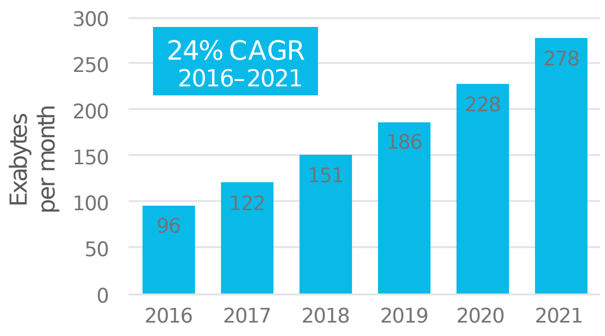

Figure 1.1: Global IP traffic forecast from CISCO[1]

1.1 Optical Telecommunication Systems

Modern-day long haul and high capacity data transmission in made possible to a large extent by the high bandwidth offered by using light as the carrier of data. Fundamentally optical telecommunication is achieved by using light from a laser, modulating it using the required data to be transmitted, sending the modulated light through an optical fibre and using a photodiode at the receiver end to detect the signal. Lasers (especially semiconductor lasers) are used as light sources because of their high monochromaticity, low spectral linewidth and compact size. Thus, chromatic and modal dispersion along the fibre can be reduced and very large transmission distances can be achieved.

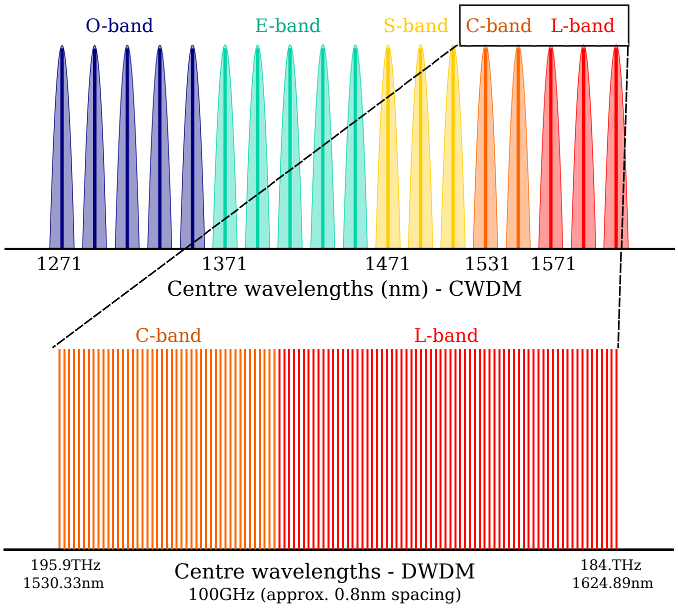

Figure 1.2: Wavelengths in Coarse and Dense WDM systems

Silica optical fibres used in long-haul networks have a low attenuation of 0.2dB / km [2] in a window centred around a wavelength of 1.55μm. Data can be encoded onto multiple wavelength channels simultaneously within this window to fully exploit the available optical bandwidth. This technique is known as Wavelength Division Multiplexing (WDM). In the past decade, Coarse WDM was used with the wavelength channels separated by 20 nm in with the wavelength span ranging from 1271 to 1611 nm split between various sub-bands as illustrated in Figure 1.2. With the increase in demand for bandwidth, coarse WDM are being increasingly replaced by Dense WDM (DWDM). Typically, DWDM systems have a channel spacing of 100 GHz (0.8nm) with some systems even going down to 50 or 25 GHz channel spacing [3]. The use of Erbium-doped Fibre Amplifiers (EDFAs) which work in the C-band (1525-1565 nm) or L-band (1570-1610 nm) really accelerated the use of DWDM systems. Figure 1.2 shows the centre wavelengths of coarse and dense WDM systems.

1.2 Tuneable lasers

Given the use of multiple wavelength channels, it is clear that wavelength-tuneable lasers are an integral part of WDM systems. Research into tuneable lasers were ongoing since the invention of the laser in the 60s, but the term Dynamic Single Mode laser (DSM laser) was first used in 1981[4].

Starting from a simple Fabry-Pérot cavity, a number of mode selection mechanisms can be used for selecting a single mode for the laser operation, the most popular of which is a grating. The two main categories of lasers that use a grating structure for their operation are Distributed Bragg Reflector (DBR) and Distributed Feedback (DFB) lasers. While DBR designs have a separate gain section and a grating section, DFB lasers have them combined into one. Extensive work on DFB and DBR lasers were done since the early 1970s [5, 6, 7]. Demonstration of dynamic single mode lasers at 1.5 μm in 1981 by Utaka et al., was a milestone in long distance optical communication since it was at the low-loss wavelength region of silica optical fibers [8]. Since then DFB and DBR lasers and their later variants such as Sampled-Grating DBRs and Super-Structure-Grating DBRs continue to dominate the tunable laser segment.

1.2.1 DFB Laser Arrays

DFB Laser arrays are a direct logical extension of the single mode lasers. An array of single mode DFB lasers is fabricated each having a different wavelength and depending on the desired wavelength, a particular device is excited. In order to achieve wavelengths in between the different discrete wavelengths of the devices in the array, the array is tuned thermally. The output is collected at the end of an interference coupler or through an external mirror. The use of the latter eliminates the 1/N loss from the interference coupler, but since it is an external solution, it adds to the complexity of the device. Some examples of DFB laser arrays can be found in products from companies like Fujitsu [9], NTT [10], Furukawa Electric [11], NEC [12] and Santur Corporation (acquired by NeoPhotonics in 2011) [13], Santur's design involves a MEMS-actuated external mirror for the wavelength selection. Figure 1.3(a) shows the DFB array module from NEC [12] and Figure 1.3(b) shows Santur's solution [13].

The main advantages of DFB array solutions are good control of wavelength, the use mature and reliable DFB technology and stable wavelength output with no mode hops. On the other hand, the disadvantages are slow tuning, relatively bigger chip size, power consumption, coupling loss in the case of MMI couplers and moving parts and high voltage circuits in the case of the external MEMS solution [14].

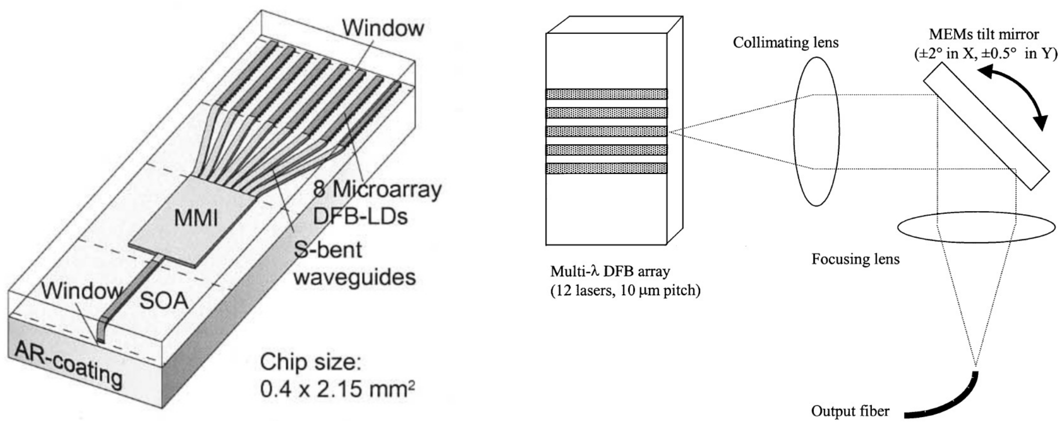

(a) (b)

Figure 1.3: DFB Laser arrays with (a) MMI coupler from NEC [12] (b) external MEMS mirror from Santur [13]

1.2.2 DBR-based devices

Drawing from the concepts of normal DBR lasers, there have been further developments to make the laser tunable and to improve their performance parameters. One of these devices is the Sampled-Grating DBR laser (SG-DBR) commercialized by Agility Inc. [15]. The device consists of two reflector sections with a slightly different reflectance combs as shown in Figure 1.4(a). This gives rise to a vernier effect and the product of these combs give the laser a very good Side Mode Suppression Ratio (SMSR). Devices based on similar physics have also been developed at NTT called Super-Structure-Grating DBR lasers (SSG-DBR) [16] and by Bookham (acquired by Oclaro) called Digital Supermode DBR laser (DS-DBR) [17], but differential gain and output power are not as good because of grating losses during tuning by current injection. An additional gain section in the form of an optical amplifier needs to be added to the device to compensate for the losses, and after such an improvement, fiber-coupled optical output powers of around 40mW have been achieved. Syntune (acquired by Finisar) has developed a solution based on a similar vernier effect, but with a key difference - both the tuning elements are on the same side of the gain block as opposed to the gain block being sandwiched by the two tuning sections in the other devices [18] as shown in Figure 1.4(b). This structure is called Modulated-Grating Y-Branch (MG-Y). MG-Y lasers tend to have higher output power levels (13 dBm) without the need for additional amplification. On the other hand, tuning is not continuous and they exhibit higher phase noise compared to other designs [14], for example the design by Coretek (acquired by Nortel) [19] which is a vertical cavity laser whose top mirror is mounted on a MEMS arm and can be moved up and down leading to wavelength tunability. This device also needs an optical pump co-packaged with it. Although VCSELs have a good reputation at lower wavelengths, they suffer from lower optical power and wider linewidth at telecommunication wavelengths [20]. Another design combining the wide tuning capabilities of a grating-assisted coupler with a sampled-grating reflector is the Grating-Coupled Sampled-Reflector (GCSR) laser [21]. GCSR devices have been shown to have >100nm tuning range [22] and SMSR is excess of 35dB [23].

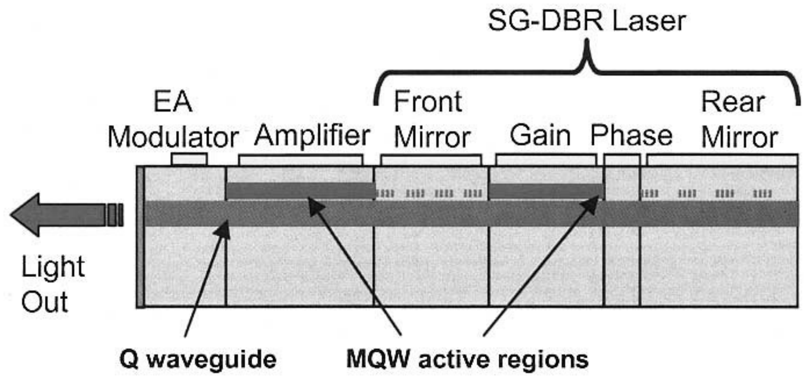

(a)

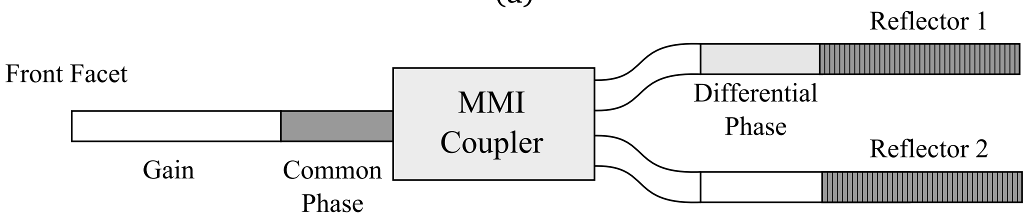

(b)

Figure 1.4: Schematic of a (a) SG-DBR Laser [20] and (b) MG-Y Laser[18]

1.2.3 External Cavity Solutions

External cavity tuneable lasers involve a multi-mode laser diode that acts as the gain block and an external mode selection filter to achieve the single-mode operation. In most cases, the light is coupled between the gain and mode selection blocks with the help of bulk optical elements like lenses and mirrors. Iolon Inc. (acquired by Coherent in 2005) demonstrated an external cavity tunable laser with a MEMS grating as the wavelength selective element [24]. NEC also offers an external cavity tunable laser using a liquid- crystal based tunable mirror [25]. The MEMS grating solution from Iolon has a wide tuning range (100nm) and good optical power (>10dBm). The downside of Iolon's solution is that it can be modulated only upto 3.2 Gb/s, and the liquid-crystal solution from NEC suffers from slow tuning and the requirement of additional liquid crystal drivers [14]. In addition to the above, there exist solutions based on tunable filters. Fujitsu has a tunable laser based on an Acousto-optical tunable filter (AOTF) [26]. Intel has demonstrated a tunable laser (acquired from New Focus) based on a temperature tuned etalon [27]. The AOTF-based approach proved to have a very wide tuning range and good tuning speed, but it is fabricated on $LiNbO_3$ the device is very large in size (~5cm). While Intel's design has a low power consumption, its tuning speed is slow due to the thermally tuned etalon [14].

1.2.4 Other Tunable Laser Designs

Although currently DBR-based and DFB array based devices own a big share of the tunable laser market for telecommunications, there are many more designs being proposed at the research level. NTT has demonstrated a tunable laser design with ring resonators as wavelength selective elements [28]. The devices show a good tuning range covering the C-band with low power consumption. They also show wavelength drifts of less than 5 GHz during thermal transients. These devices do not require electron beam lithography, and thus are easier to fabricate than SG-DBR lasers, but they do require one regrowth process. Another concept of a tunable laser comes from JDSU using a tunable-MMI [29] which has good optical power outputs without the use of an amplifier. Just like the previous design, this device suffers from the use of a regrowth process and also the use of sophisticated lithography processes since it uses a sampled grating to provide the comb reflectance.

Table 1.1: Summary of State-of-the-art performances of various monolithic widely tunable lasers

Type	Tuning Range	Output Power	SMSR	References
SSG-DBR	140 nm	10 dBm	40	[30]
DS-DBR	50 nm	8-9 dBm	50	[31]
GCSR	114 nm	1-2 mW	20	[22]
MG-Y	45 nm	13 dBm	40	[18]

Table 1.1 summarises the key performance parameters of the various main types of monolithic tuneable lasers. With the advent of wavelength division multiplexing and dynamic wavelength-reconfigurable optical networks, tuneable lasers were greatly in demand. But there has always been stiff competition from the fixed wavelength DFB switch were preferred over tuneable lasers for their lower cost and better performance. But the increased penetration of the internet and the growth in demand for bandwidth every year, has led to the need for more wavelength channels and concepts like Dense and Ultra-Dense WDM. This means that, if individual fixed frequency DFBs are used, albeit being cheaper, they need different wavelength specific line cards and other related equipment. This increases the total cost of the optical network considerably and has led to the present situation where for similar performance specifications, the market would prefer a tuneable laser solution compared to a fixed wavelength DFB, even if it comes with a small premium in the cost [20]. Besides the market-driven reasons for the need for tunable lasers described above, there also exist technological reasons to push forward research in tuneable lasers. Tuneable transmitter components are essential in ROADMs (Reconfigurable Optical Add-Drop Multiplexers) that reduce the cost of adding and/or dropping small amounts of information to/from a fiber optic link. Tuneable lasers are also very important components in optical switches where they are used in wavelength conversion [32]. Their importance is not only limited to optical telecommunication, but they are also very useful in sensing applications where the sensors need to sweep the wavelength of the optical source over different frequencies [20] e.g. gas sensing and Optical Coherence Tomography (OCT).

1.3 Motivation for this work

As discussed at the outset of this chapter, the demand for bandwidth continues to increase at a rapid rate every year. In the past decade, access networks which connect the subscribers to their internet service provider have been transitioning from the use of copper cables (e.g. DSL - Digital Subscriber Line) to optical fibres (Fibre to the x - FTTX) which provide much higher bandwidth.

Currently, the most commonly deployed optical access network technologies such as EPON, GPON etc. use a fixed wavelength for data transmission in the upstream direction. But looking towards the future, next-generation access network standards such as NG-PON2 will require tunable laser sources in the Optical Networking Units (ONUs) so that upstream wavelength can be chosen dynamically to balance loads in the network. Since these ONUs are situated at the consumers' premises, cost is a very critical factor. This means that Bragg-reflector based designs for the tunable lasers, which are used commonly in the downstream direction, are too expensive for such widespread use in consumer products especially with the added cost of packaging and calibration. Integrating all the components of the transmitter such as the laser, modulator and wavelength monitor offers further ONU cost reduction in comparison to discrete components. This forms the motivation for this thesis which attempts to describe the realisation of such an integrated low-cost tunable transmitter module - a microscope image of which is shown below in Figure 1.5.

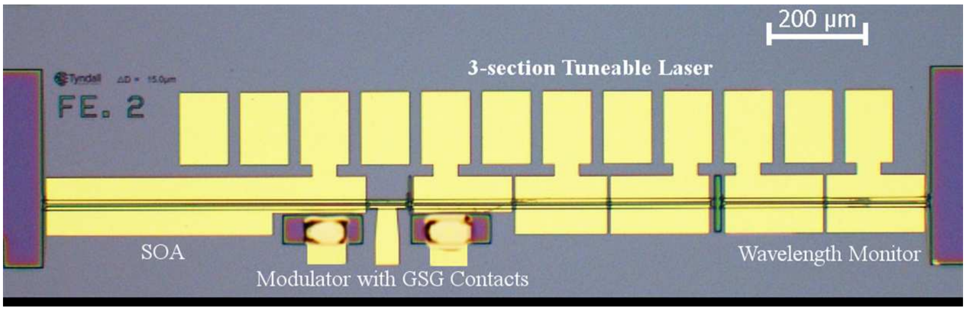

Figure 1.5: Microscope image the fully integrated transmitter device developed in this thesis work

1.4 Thesis outline

A concise organisational structure of this dissertation is as follows:

Chapter 2 introduces Slotted Fabry-Pérot lasers, the chosen technology in this thesis for the low-cost tunable laser. It presents the theory behind the technology, device structure and fabrication of this type of lasers, and experimental results from the same.

Chapter 3 discusses the need for wavelength monitoring. It presents the theory and design of the wavelength monitor that can be conveniently integrated with the tuneable laser, its performance characteristics as a standalone device along with its polarisation sensitivity.

Chapter 4 presents the integrated device containing the laser and wavelength monitor from Chapters 1 and 2 respectively along with an optical modulator and a semiconductor optical amplifier (SOA) booster. Experimental results showing performances up to 10Gb/s are presented.

Chapter 5 discusses the electrical, optical and thermal crosstalk issues in the integrated device and possible strategies to overcome this.

Finally **in Chapter 6**, a conclusive summary of the thesis is presented along with possible directions of future work.

References

[1] "CISCO Visual Networking Index: Forecast and Methodology, 2016–2021." http://www.cisco.com/c/en/us/solutions/collateral/service-provider/visual-networking-index-vni/complete-white-paper-c11-481360.html. (Accessed on 15-July-2019).

[2] "G.692: Optical interfaces for multichannel systems with optical amplifiers." https://www.itu.int/rec/T-REC-G.692-199810-I/en. (Accessed on 01-Sep-2019).

[3] "G.694.1: Spectral grids for WDM applications: DWDM frequency grid." https://www.itu.int/rec/T-REC-G.694.1/. (Accessed on 01-Sep-2019).

[4] Y. Suematsu and K. Iga, "Integrated GaInAsP/InP laser," *1st European Conference on Integrated Optics*, pp. 70–75, September 1981.

[5] M. Nakamura, A. Yariv, H. Yen, S. Somekh, and H. L. Garvin, "Optically pumped GaAs surface laser with corrugation feedback," *Applied Physics Letters*, vol. 22, no. 10, pp. 515–516, 1973.

[6] F. K. Reinhart, R. A. Logan, and C. V. Shank, "GaAs-$Al_xGa_{1-x}As$ injection lasers with distributed bragg reflectors," *Applied Physics Letters*, vol. 27, no. 1, pp. 45–48, 1975.

[7] K. Aiki, M. Nakamura, and J. Umeda, "Frequency multiplexing light source with monolithically integrated distributed-feedback diode lasers," *Applied Physics Letters*, vol. 29, no. 8, pp. 506–508, 1976.

[8] K. Utaka, K. Kobayashi, and Y. Suematsu, "Lasing characteristics of 1.5-1.6μm GaInAsP/InP integrated twin-guide lasers with first-order distributed bragg reflectors," *IEEE Journal of Quantum Electronics*, vol. 17, pp. 651–658, May 1981.

[9] M. Bouda, M. Matsuda, K. Morito, S. Hara, T. Watanabe, T. Fujii, and

Y. Kotaki, “Compact high-power wavelength selectable lasers for WDM applications,” in *Optical Fiber Communication Conference, 2000*, vol. 1, pp. 178–180 vol.1, 2000.

[10] H. Ishii, H. Oohashi, K. Kasaya, K. Tsuzuki, and Y. Tohmori, “High-power (40 mW) L-band tunable DFB laser array module using current tuning,” in *Optical Fiber Communication Conference, 2005. Technical Digest. OFC/NFOEC*, vol. 2, pp. 3 pp. Vol. 2–, 2005.

[11] T. Mukaihara, Y. Nagakawa, H. Nasu, H. Kambayashi, M. Oike, S. Yoshimi, T. Kurobe, T. Kimoto, K. Maranushi, T. Nomura, and A. Kasukawa, “High power, low noise, low power consumption, 25 GHz x 180 ch thermally tunable DFB laser module integrated with stable wavelength monitor,” in *Eur. Conf. Optical Communication ECOC, Rimini, Italy*, pp. 718–719, 2003.

[12] H. Hatakeyama, K. Naniwae, K. Kudo, N. Suzuki, S. Sudo, S. Ae, Y. Muroya, K. Yashiki, K. Satoh, T. Morimoto, K. Mori, and T. Sasaki, “Wavelength-selectable microarray light sources for S-, C-, and L-band WDM systems,” *IEEE Photonics Technology Letters*, vol. 15, pp. 903–905, July 2003.

[13] B. Pezeshki, E. Vail, J. Kubicky, G. Yoffe, S. Zou, J. Heanue, P. Epp, S. Rishton, D. Ton, B. Faraji, M. Emanuel, X. Hong, M. Sherback, V. Agrawal, C. Chipman, and T. Razazan, “20-mW widely tunable laser module using DFB array and MEMS selection,” *IEEE Photonics Technology Letters*, vol. 14, pp. 1457–1459, Oct 2002.

[14] J. Buus and E. Murphy, “Tunable lasers in optical networks,” *Lightwave Technology, Journal of*, vol. 24, no. 1, pp. 5–11, 2006.

[15] B. Mason, J. Barton, G. Fish, L. Coldren, and S. P. DenBaars, “Design of sampled grating DBR lasers with integrated semiconductor optical amplifiers,” *Photonics Technology Letters, IEEE*, vol. 12, no. 7, pp. 762–764, 2000.

[16] Y. Tohmori, Y. Yoshikuni, H. Ishii, F. Kano, T. Tamamura, Y. Kondo, and M. Yamamoto, “Broad-range wavelength-tunable superstructure grating (SSG) DBR lasers,” *Quantum Electronics, IEEE Journal of*, vol. 29, no. 6, pp. 1817–1823, 1993.

[17] A. Ward, D. Robbins, G. Busico, E. Barton, L. Ponnampalam, J. Duck, N. Whitbread, P. Williams, D. C. J. Reid, A. Carter, and M. Wale, “Widely

tunable DS-DBR laser with monolithically integrated SOA: design and performance," *Selected Topics in Quantum Electronics, IEEE Journal of*, vol. 11, no. 1, pp. 149–156, 2005.

[18] J.-O. Wesstrom, G. Sarlet, S. Hammerfeldt, L. Lundqvist, P. Szabo, and P.-J. Rigole, "State-of-the-art performance of widely tunable modulated grating Y-branch lasers," in *Optical Fiber Communication Conference, 2004. OFC 2004*, vol. 1, pp. 389–, 2004.

[19] K. Knopp, D. Vakhshoori, P. Wang, M. Azimi, M. Jiang, P. Chen, Y. Matsui, K. McCallion, A. Baliga, F. Sakhitab, M. Letsch, B. Johnson, R. Huang, A. Jean, B. DeLargy, C. Pinzone, F. Fan, J. Liu, C. Lu, J. Zhou, H. Zhu, R. Gurjar, P. Tayebati, D. MacDaniel, R. Baorui, R. Waterson, and G. VanderRhodes, "High power MEMS-tunable vertical-cavity surface-emitting lasers," in *Digest of the LEOS Summer Topicals*, pp. 2 pp.–, 2001.

[20] L. A. Coldren, G. A. Fish, Y. Akulova, J. S. Barton, L. Johansson, and C. W. Coldren, "Tunable semiconductor lasers: a tutorial," *Journal of Lightwave Technology*, vol. 22, pp. 193–202, Jan 2004.

[21] M. Oberg, S. Nilsson, K. Streubel, J. Wallin, L. Backbom, and T. Klinga, "74 nm wavelength tuning range of an InGaAsP/InP vertical grating assisted codirectional coupler laser with rear sampled grating reflector," *IEEE Photonics Technology Letters*, vol. 5, pp. 735–737, July 1993.

[22] P.-J. Rigole, S. Nilsson, L. Backbom, T. Klinga, J. Wallin, B. Stalnacke, E. Berglind, and B. Stoltz, "114-nm wavelength tuning range of a vertical grating assisted codirectional coupler laser with a super structure grating distributed Bragg reflector," *IEEE Photonics Technology Letters*, vol. 7, pp. 697–699, Jul 1995.

[23] P. J. Rigole, S. Nilsson, L. Backbom, T. Klinga, J. Wallin, B. Stalnacke, E. Berglind, and B. Stoltz, "Access to 20 evenly distributed wavelengths over 100 nm using only a single current tuning in a four-electrode monolithic semiconductor laser," *IEEE Photonics Technology Letters*, vol. 7, pp. 1249–1251, Nov 1995.

[24] D. Anthon, J. Berger, and A. Tselikov, "C+L band MEMS tunable external cavity semiconductor laser," in *Optical Fiber Communication Conference, 2004. OFC 2004*, vol. 1, pp. 761–, 2004.

[25] J. De Merlier, K. Mizutani, S. Sudo, K. Naniwae, Y. Furushima, S. Sato,

K. Sato, and K. Kudo, "Full C-band external cavity wavelength tunable laser using a liquid-Crystal-based tunable mirror," *Photonics Technology Letters, IEEE*, vol. 17, no. 3, pp. 681–683, 2005.

[26] K. Takabayashi, K. Takada, N. Hashimoto, M. Doi, S. Tomabechi, T. Nakazawa, and K. Morito, "Widely (132 nm) wavelength tunable laser using a semiconductor optical amplifier and an acousto-optic tunable filter," *Electronics Letters*, vol. 40, no. 19, pp. 1187–1188, 2004.

[27] W. B. Chapman, A. J. Daiber, M. McDonald, M. Finot, and W. J. Kozlovsky, "Temperature tuned external cavity diode laser with micromachined silicon etalons," in *Conference on Lasers and Electro-Optics/International Quantum Electronics Conference and Photonic Applications Systems Technologies*, p. CWC2, Optical Society of America, 2004.

[28] T. Segawa, S. Matsuo, T. Kakitsuka, T. Sato, Y. Kondo, and R. Takahashi, "Semiconductor Double-Ring-Resonator-Coupled Tunable Laser for Wavelength Routing," *Quantum Electronics, IEEE Journal of*, vol. 45, no. 7, pp. 892–899, 2009.

[29] H. G. Bukkems, R. Strijbos, J. J. M. Binsma, H. de Vrieze, M. Larson, M. Smit, E. A. J. M. Bente, and B. Verbeek, "A Tunable-MMI-Coupler-Based Wavelength Adjustable Laser," *Quantum Electronics, IEEE Journal of*, vol. 43, no. 7, pp. 614–621, 2007.

[30] N. Fujiwara, R. Yoshimura, K. Kato, H. Ishii, F. Kano, Y. Kawaguchi, Y. Kondo, K. Ohbayashi, and H. Oohashi, "140-nm Quasi-Continuous Fast Sweep Using SSG-DBR Lasers," *IEEE Photonics Technology Letters*, vol. 20, pp. 1015–1017, June 2008.

[31] A. J. Ward, D. J. Robbins, G. Busico, N. D. Whitbread, P. J. Williams, D. C. J. Reid, and J. R. Rawsthorne, "Modelling of phase-grating based wideband tuneable lasers with simplified quasi-digital wavelength selection," *IEE Proceedings - Optoelectronics*, vol. 150, pp. 199–204, April 2003.

[32] D. J. Blumenthal, B. E. Olsson, G. Rossi, T. E. Dimmick, L. Rau, M. Masanovic, O. Lavrova, R. Doshi, O. Jerphagnon, J. E. Bowers, V. Kaman, L. A. Coldren, and J. Barton, "All-optical label swapping networks and technologies," *Journal of Lightwave Technology*, vol. 18, pp. 2058–2075, Dec 2000.

Chapter 2

Slotted Fabry-Pérot Lasers

As seen from Chapter 1, the need for low-cost tuneable lasers is increasing with the deployment of Fibre-to-the-x (FTTx) networks and in general with the use of adaptive optical telecom protocols. This chapter presents the *Slotted Fabry-Pérot* technology (Figure 2.1) as a solution to this need.

The first mention of slots along the ridge waveguide of a laser in the literature was made in the 1980's by Coldren *et al*, who called it *grooves* in their paper [1]. Since then slots have been used in making tuneable single (longitudinal) mode lasers in various forms [2, 3]. The first section of this chapter describes the theory behind the operation of slotted Fabry-Pérot lasers. The second section describes, in detail, the fabrication process for these type of lasers, which is low-cost and foundry compatible requiring no selective area bandgap engineering techniques. The third section presents experimental results obtained from these wavelength-agile lasers. And in the final section, a summary of the chapter is presented along with a discussion about the potential applications for slotted Fabry-Pérot lasers.

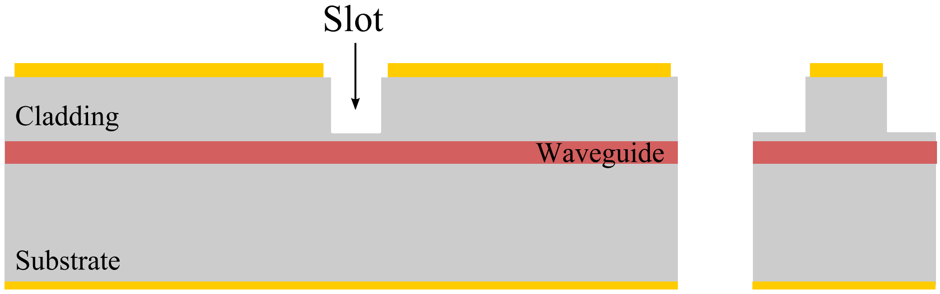

Figure 2.1: Cross-sections of a typical slotted Fabry-Pérot laser

2.1 Theory of Operation

2.1.1 Semiconductor Heterostructures

The first demonstration of coherent light emission from a semiconductor diode (based on Gallium Arsenide) was done by Hall *et al* [4] and Nathan *et al* [5] in 1962. These lasers and the other common designs of that era were homojunction lasers, i. e. the active core layer and the cladding were both made from the same material (GaAs) and thus had the same bandgap and refractive index. They had threshold current densities of about 1000 A/cm^2 at a low temperature of 77K, but at room temperature of 300K, the threshold current densities were orders of magnitude higher at about 100000 A/cm^2. This is mainly due to the fact that electrons and holes are free to diffuse, i.e. there is poor carrier confinement which results in poor gain. This meant that the lasers could operate at continuous wave (CW) mode only at low temperatures and could exhibit only pulsed mode operation at room temperature.

The concept of a heterojunction was introduced in 1954 by Kroemer [6] where two different semiconductor materials with varying bandgaps could be used. In a heterojunction, the bandgap of the p-type layer could be raised above that of the n-type layer underneath. This helps in creating a large potential barrier for minority carriers thus essentially only injecting the majority carriers from the wider bandgap material to the lower one. This achieves better optical confinement compared to homojunctions thus reducing the threshold current. In the mid 1960s, with the advance of epitaxial methods, in particular the possibility of liquid phase epitaxy of aluminium gallium arsenide, heterojunctions could now be created. Despite the increase in carrier confinement, the threshold current density could only be reduced around 10 times still making single-heterojunction lasers unable to exhibit CW lasing at room temperature [7].

The solution to achieving even better carrier confinement than a single heterojunction is to sandwich the active material on both sides with a higher bandgap material, which came to be known as a *double heterostructure* (DH) laser, as illustrated in Figure 2.2. This concept of a DH laser diode was first introduced by Kroemer [8] and Alferov *et al* [9] in 1963, and the first semiconductor lasers to demonstrate CW operation at room temperature were indeed based on a double heterostructure in 1970 [10, 11]. Kroemer and Alferov went on to receive the Nobel prize for physics in the year 2000.

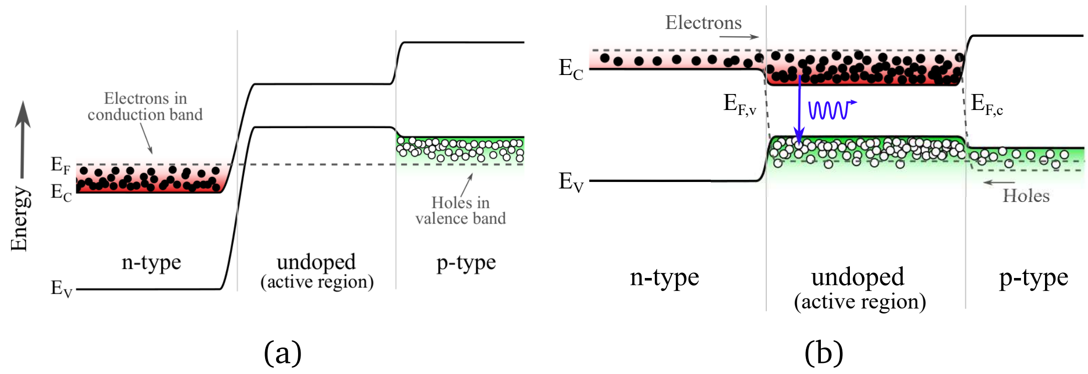

Figure 2.2: Illustrations (simplified) of band structure in a double heterostructure at (a) equilibrium - unbiased and (b) forward bias

When a double heterostructure is forward biased, electrons are injected into the active region from the n-type semiconductor and holes are injected into the active region from the p-type semiconductor. The higher bandgap on both sides ensures that electrons cannot escape into the p-type material and holes cannot escape into the n-type material. Thus electrons and holes are forced to recombine in the active region, leading to emission of photons. The carrier confinement can thus be obtained in DH diodes for a bandgap difference of at least 0.25 eV between the active and the cladding regions [12].

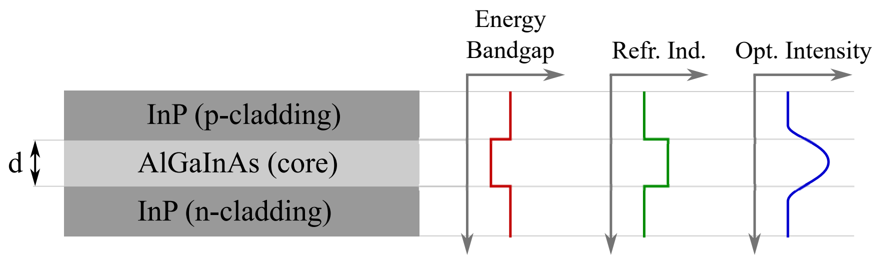

Figure 2.3: Illustration of the bandgap, refractive index and optical intensity profiles along a double heterostructure

Along with carrier confinement, another important requirement for an efficient laser diode is optical confinement. A convenient coincidence that can be exploited in this context is that the refractive index at a wavelength decreases with increase in bandgap. This means in a DH scenario, when a material with a lower bandgap is sandwiched by materials with higher bandgaps, the refractive index is highest in the middle layer and lower in the outer cladding layer on either side. The light that is generated in the active layer is confined well inside itself owing to the fact that an optical waveguide is formed in the transverse direction resulting from the refractive index profile as illustrated in Figure 2.3.

2.1.1.1 Semiconductor Material Systems

In order to choose the appropriate material system for the fabrication of the laser, we need to take into consideration a few key points. A semiconductor double heterostructure is grown using epitaxial methods needing high crystalline quality, which requires that the materials should be lattice matched perfectly. This requirement means that substrates could be binary III-V compound semiconductors like GaAs or InP since their lattice constants are defined unambiguously by stoichiometry. And depending on the substrate used, ternary or quaternary alloys can be used as the lower bandgap material. For example, AlGaAs can be lattice matched to GaAs and alloys like InGaAsP and AlInGaAs can be lattice-matched to an InP substrate.

It is also beneficial if the difference in bandgap energy between the two materials in the DH structure is as large as possible for better efficiency. In this context, quaternary alloys may have an edge as they have two parameters to vary compared to one in ternary alloys. For example, in $Al_xGa_yIn_{1-x-y}As$ the mole fractions of aluminium (x) and Gallium (y) can be varied, whereas in $Al_xGa_{1-x}As$ only the mole fraction of aluminium (x) can be varied. Having two variables lets us choose from different bandgap energies while simultaneously trying to satisfy the lattice matching requirement. In practice, the most widely used material systems for semiconductor lasers are AlGaAs on GaAs and InGaAsP/AlInGaAs on InP. Material systems involving GaAs substrates cover wavelength ranges below 900nm whereas the ones using InP substrates cover wavelengths over 1200nm. In this work, since we deal with wavelengths for telecommunication applications, which are around the 1550nm region, we choose a material system based on an InP substrate. Furthermore, AlInGaAs on InP was preferred over InGaAsP on InP because the conduction band offset is larger in the former ($\Delta E_c = 0.72\Delta E_g$ compared to $\Delta E_c = 0.40\Delta E_g$ in the latter) and the fact that electrons have a lower $m*$ which lead to improved electron confinement confinement [13, 14].

2.1.2 Optical Waveguiding

2.1.2.1 Transverse Waveguiding

Using a double heterostructure as described above, an optical waveguide in the transverse direction can be formed. The optical modes supported by this waveguide can be *guided* or *radiation* modes. We shall concentrate on the guided modes, which can be further classified into *Transverse Electric* (TE) or *Transverse Magnetic* (TM) modes. In these modes only the electric field component (for TE) or the magnetic field component (for TM) lies in the plane perpendicular to the direction of propagation.

It is useful to define a parameter known as the *optical confinement factor*, which is a measure of the optical power confined in the active region compared to the total optical power. Using the vertical direction in Figure 2.3 as the x-coordinate beginning from $-\infty$ at the bottom, passing through 0 at the lower interface between InP and AlGaInAs and increasing in the upwards direction, we can write the confinement factor, Γ as:

$$\Gamma = \frac{\int_0^d |E(x)|^2 \, dx}{\int_{-\infty}^{\infty} |E(x)|^2 \, dx} \tag{2.1}$$

Usually exact confinement factors are calculated numerically, but there exists a good analytical approximation (for symmetric heterostructures) proposed by Botez [15], which is given by:

$$\begin{gathered} \Gamma \approx \frac{\Gamma'}{1+\Gamma'} \\ \text{where } \; \Gamma' = 2\pi^2 \left(n_1^2 - n_2^2\right) \left(\frac{d}{\lambda}\right)^2 \end{gathered} \tag{2.2}$$

where n_1 and n_2 are the refractive indices of the core and the cladding materials respectively, and λ is the wavelength. For a wavelength of 1550nm and a cladding material of InP (with n_2 = 3.167), the confinement factor is plotted in Figure 2.4 using Equation 2.2 for different values of n_2. In the devices presented in this thesis, the active region is AlInGaAs which has a refractive index of around 0.3 higher than InP, which corresponds to the red curve in Figure 2.4. We can see that for higher values of d, the confinement factor is higher - which is desirable. But optical telecommunication systems typically use single-moded fibre for transmission as they do not exhibit modal dispersion resulting in longer distance transmission capabilities.

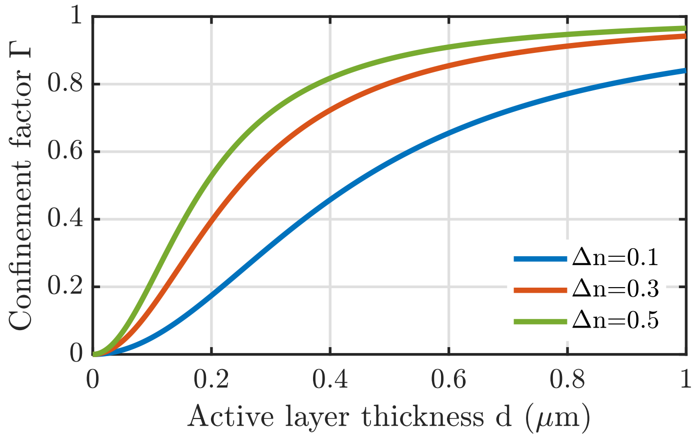

Figure 2.4: Confinement factor vs active layer thickness (bulk) for different refractive index contrasts at 1550nm for an InP substrate

Thus, the the epitaxial structure is also designed such that only the fundamental mode is guided in the waveguide. The condition for this to occur is [12]:

$$d < \frac{\lambda}{2\sqrt{n_1^2 - n_2^2}} \tag{2.3}$$

In our case, this translates to an active layer of thickness less than 550 nm.

2.1.2.2 Lateral Waveguiding

In the previous section, we have discussed transverse waveguiding in the laser structure. However, for stable and well-defined laser operation, it is also necessary to have waveguiding in the lateral direction [12]. This can be achieved in two ways, known as *index guiding* (IG) and *gain guiding* (GG). In IG structures, a ridge-type geometry is fabricated in the lateral direction, thus forming a waveguide with the higher-index semiconductor as the core and the lower-index semiconductor as the cladding layer. Along with the epitaxial structure in the transverse direction, this effectively forms a two dimensional waveguide. On the other hand, in GG structures, there are no geometrical features in the lateral direction. The waveguiding in the lateral direction is entirely based on confining the gain to a narrow region. This is achieved by a stripe metal contact where the injected current is restricted to a few microns.

The waveguiding in GG lasers is absent compared to IG lasers. This causes many impairments such as beam instabilities, astigmatic fields, multi-modal behaviour and higher threshold currents [12]. Hence for application in optical communication, index guided lasers are mandatory which are also used in this thesis work.

2.1.3 Quantum-Well Laser Diodes

The first semiconductor DH laser materials were grown using liquid phase epitaxy (LPE). During the growth process, the wafer had to be quickly moved in the LPE machine between different melts of materials - the n-type, p-type and undoped material. This had to be done rapidly since the active region had to be less than a micron thick. With the advance in epitaxial techniques, especially molecular beam epitaxy (MBE) and metal organic vapour phase epitaxy (MOVPE) it was possible to control the epitaxial growth at almost atomic layer, capable of producing very thin layers, which are called *quantum well* (QW) structures [12]. If the thickness of the core layer is smaller than the de Broglie wavelength of the carriers (about 15nm) quantisation effects start to appear. The density of states is modified as illustrated in Figure 2.5, and this leads to an increase in the differential gain since the injected carriers are now spread over a narrower energy range due to the quantisation.

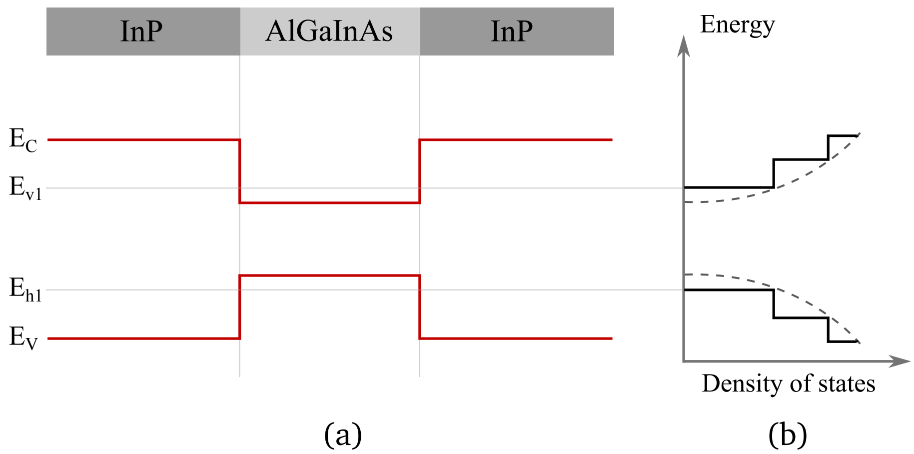

Figure 2.5: Illustration of the (a) conduction band and valence band edges and (b) the density of state in a quantum well (solid curve) and bulk semiconductor (dashed)

The requirement of lattice matching in quantum well structures can be more relaxed than bulk structures owing to the extreme small thickness of the grown layer. Hence, a small amount of strain, f, can be tolerated where f is given by:

$$f = \frac{a - a_0}{a_0} = \frac{\Delta a}{a_0} \tag{2.4}$$

where a_0 is the lattice constant of the substrate and a is the lattice constant of the layer grown on top of it. The critical thickness, h_c up to which the strained layer can be grown without damaging the entire crystal structure is given by [16]:

$$h_c = \frac{a}{32\sqrt{2}\pi f^2} \frac{1+\nu}{1-\nu} \ln\left(\frac{\sqrt{2}h_c}{a}\right) \tag{2.5}$$

where ν is the Poisson ratio, which is approximately 0.33 for most semiconductors [12]. Combining Equations 2.4 and 2.5 we can write:

$$h_c = \frac{a_0}{32\sqrt{2}\pi} \left(\frac{1+f}{f^2}\right) \frac{1+\nu}{1-\nu} \ln\left(\frac{\sqrt{2}h_c}{a_0(1+f)}\right) \tag{2.6}$$

Substituting the lattice constant a_0 = 0.587 nm of InP and ν = 0.33, we get:

$$h_c(nm) = 0.00206 \frac{1+f}{f^2} \ln\left(\frac{2.4092h_c}{1+f}\right) \tag{2.7}$$

The analytic form of the above equation can be expressed as:

$$h_c(nm) = 0.4150(1+f)e^{-W_{-1}(-201.49f^2)}nm \tag{2.8}$$

where W_{-1} is the lower branch of the Lambert-W function. Equation 2.8 is plotted in Figure 2.6.

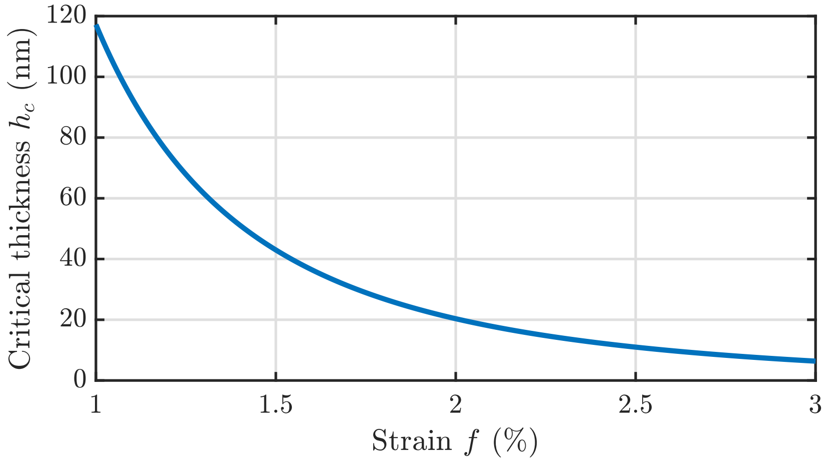

Figure 2.6: Critical thickness vs Strain for an indium phosphide substrate

We can see that strain values of around 2.5-3% can be tolerated by the core layer whose thickness is in the range of 10nm (as is required for the quantisation effects). Strained layers exhibit improved performance mainly due to the fact that the degeneracy of light hole and heavy hole valence bands is lifted by the strain. Hence, the density of states at the bottom of the valence band decreases resulting in population inversion for lower current densities [12, 17]. Thus, with the strain we have an additional degree of freedom for the design of the epitaxial layers and engineering the bandgap of the materials in order to achieve better efficiency. The devices presented in this thesis are fabricated on an epitaxial structure with a compressive strain of about 1.2% in the quantum wells and a thickness of 6 nm, which is well under the critical thickness.

As we seen from the previous section on optical waveguides (Equation 2.2 and Figure 2.4)the optical confinement goes down as the active layer thickness decreases (for small values of the active layer thickness). We can see this illustrated in Figure 2.7 (a) which shows the carrier wavefunction along with the photon distribution. The optical confinement can be improved by adding an additional wave-guiding layer around the quantum well as shown in Figure 2.7 (b). This is usually known as *separate confinement heterostructure* quantum well (SCHQW) structures. Optical confinement and gain can be further increased by increasing the number of quantum wells - by the use of multiple quantum well (MQW) structures. The SCH structure can be made to have a constant composition (as in Figure 2.7 (b))or a graded composition, which leads to a graded refractive index. This is referred to as a GRIN (Graded Index) SCH QW structure. In a GRINSCH structure, the carrier confinement is achieved by the quantum well and the optical confinement is achieved by the surrounding waveguide structure, thus effectively decoupling the electronic and optical effects [18].

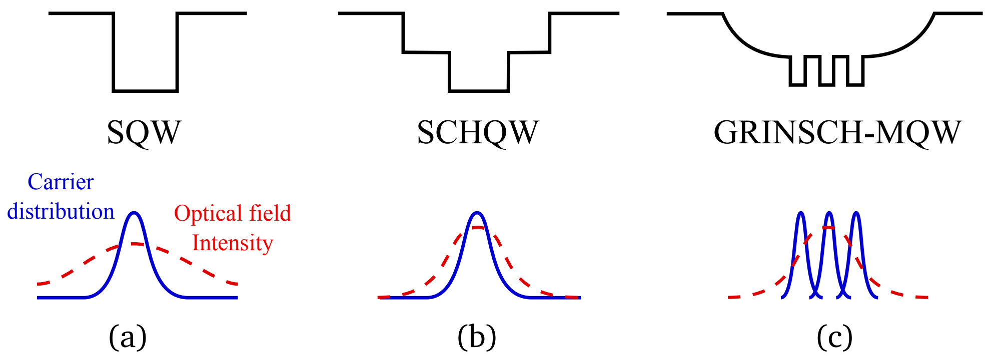

Figure 2.7: Illustration of carrier distribution and optical field intensity in (a) a single quantum well (b) an SCH-QW and (c) a GRINSCH-MQW

The substrates used for fabrication of the devices in this thesis are based on GRINSCH-MQW, i. e. a combination of a GRINSCH structure along with multiple quantum wells, which is schematically shown in Figure 2.7 (c). The refractive index of the material, which is inversely proportional to the bandgap energy, is shown in Figure 2.8 for the epitaxial layer structure used in this thesis.

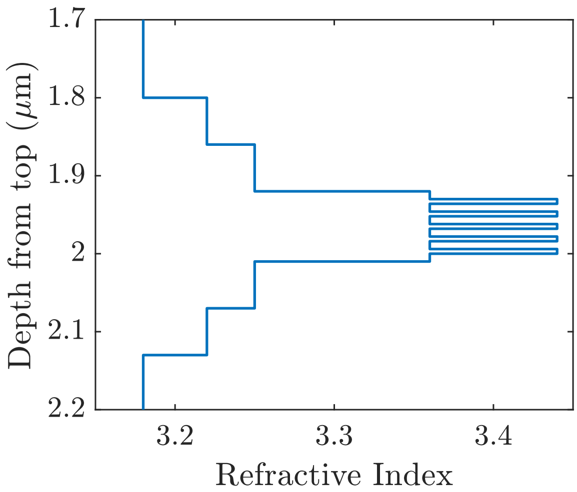

Figure 2.8: Refractive index profile of the epitaxial layer structure used in this thesis work

2.1.4 Waveguide Slot

In the previous sections techniques for optical waveguiding in the lateral and transverse directions have been introduced. To complete the design of a laser, we need a resonator in the longitudinal direction which is the third geometrical dimension. The ridge waveguide used for lateral confinement can be demarcated at the two ends forming a Fabry-Pérot (FP) cavity. Most laser diodes are based on a FP cavities, which are well documented in literature. The resonance condition for an FP cavity of length L is that the phase change after a complete round trip must be an integer multiple of 2π. This leads to a set of longitudinal lasing modes with wavelengths defined by:

$$\lambda_N = \frac{2n_{\text{eff}}L}{N} \tag{2.9}$$

where N in the mode number and n_{eff} is the effective refractive index. Usually for edge-emitting lasers, the dimension of the laser cavity is much larger than the operating optical wavelength. This leads to a large number of longitudinal modes. Hence under this approximation ($N \gg 1$), we can define a constant mode spacing given by [12]:

$$\Delta\lambda_m = \lambda_N - \lambda_{N+1} \approx \frac{\lambda_N^2}{2n_{\text{g,eff}}L}$$
$$\text{where} \quad n_{\text{g,eff}} = n_{\text{eff}}(\lambda_N) - \lambda_N \left.\frac{dn_{\text{eff}}}{d\lambda}\right|_{\lambda=\lambda_N} \tag{2.10}$$

where $n_{\text{g,eff}}$ is the effective group index. Typically in an FP laser, these longitudinal modes are enveloped by the gain curve of the active medium. The width of this curve for AlInGaAs/InP material is several tens of nanometres. As illustrated in Figure 2.9, this leads to multiple longitudinal modes.

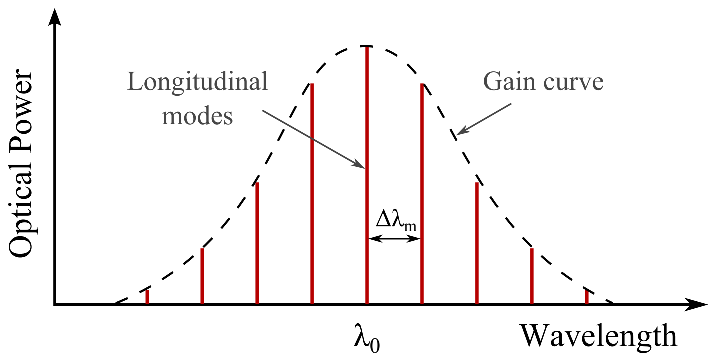

Figure 2.9: Longitudinal modes in a Fabry-Pérot laser

For applications in communication, we require lasers with a single wavelength output which translates to a single longitudinal mode. In order to achieve this we must make the gain curve sufficiently narrow so that only one mode is selected and the rest are filtered out. This *mode selection* can be done using various methods. As seen from Chapter 1, periodic structures such a Bragg gratings are used as mode selectors in single-mode laser designs such as the Distributed Bragg Reflector (DBR) and Distributed Feedback (DFB) lasers. In this work, we use *slots* along the Fabry-Pérot waveguide.

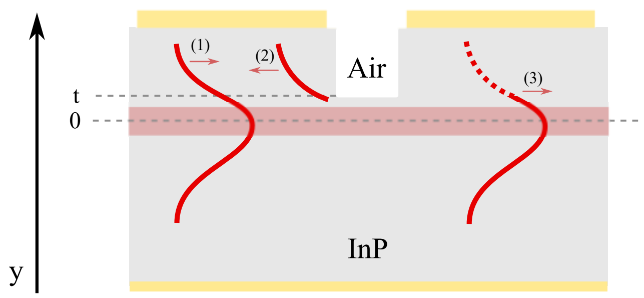

Figure 2.10: Illustration of reflection and transmission at a slot along the waveguide

Figure 2.10 provides an illustration of a slot etched into the ridge waveguide, which makes it a *Slotted Fabry-Pérot (SFP) Laser*. These slots provide reflections within the cavity which are wavelength dependent and thus aid in mode-selection to achieve single longitudinal mode lasing. In order to better understand the working of an SFP laser, we must first look at the reflections that arise from a slot. Figure 2.11 (a) and (b) show the optical field intensity inside a ridge waveguide simulated using a commercial mode solver (Lumerical FDTD). We can observe that the intensity is a symmetric Gaussian-shaped beam around the quantum well region. This is schematically shown in Figure 2.10 marked as (1). At a slot, part of this field is reflected at the InP/air interface (marked as (2) in Figure 2.10) with a reflectivity value dictated by the refractive index difference between InP and air. The truncated field propagates forward as shown marked as (3) in Figure 2.10. This is justified from the numerical simulations of the optical field intensity at the slot, shown in Figure 2.11 (c) and (d), where we observe that the mode is pushed further into the substrate and is truncated rapidly going above the InP/air interface at the bottom of the slot.

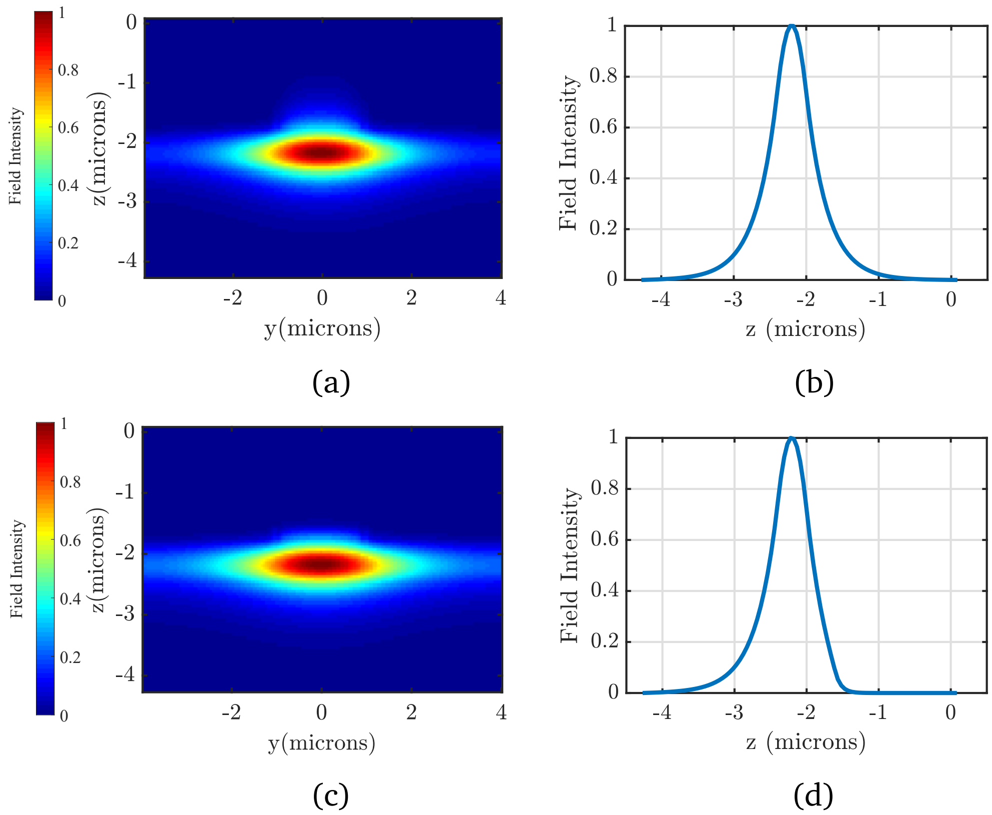

Figure 2.11: Mode profiles at (a) waveguide and (b) slot, and (c and d) the corresponding slices at y=0 location

To calculate the reflectance of a slot r_s, we compute the overlap integral of the fundamental mode of the waveguide and the reflected field, given by [1]:

$$r_s = r\frac{\displaystyle\int_{-\infty}^{\infty}\Psi_r(y)\Psi^*(y)dy}{\displaystyle\int_{-\infty}^{\infty}\Psi(y)\Psi^*(y)dy} \tag{2.11}$$

and the transmittance, t_s, of a slot is given by:

$$t_s = \frac{\displaystyle\int_{-\infty}^{\infty}\Psi_t(y)\Psi^*(y)dy}{\displaystyle\int_{-\infty}^{\infty}\Psi(y)\Psi^*(y)dy} \tag{2.12}$$

where r is the bulk reflectivity at the air/InP interface given by

$$r = \frac{n_{\text{InP}} - 1}{n_{\text{InP}} + 1} \tag{2.13}$$

and $\Psi(y)$ is the fundamental mode field which corresponds to the curve in Figure 2.11 (b), and $\Psi_r(y)$ and $\Psi_t(y)$ are the reflected and transmitted optical fields respectively, which are given by (in the truncation approximation):

$$\Psi_r(y) = \begin{cases}\Psi(y) & ;\ y \geq t\\ 0 & ;\ y < t\end{cases} \tag{2.14}$$

$$\Psi_t(y) = \begin{cases}0 & ;\ y \geq t\\ \Psi(y) & ;\ y < t\end{cases} \tag{2.15}$$

where t is the remaining thickness above the active layer after etching the slot. We assume that the remaining optical field which is neither reflected nor transmitted through at the slot, is lost into air at the InP/air interface. This loss incurred at the slot can be written as:

$$\eta_s = 1 - r_s^2 - t_s^2 \tag{2.16}$$

Using the above equations and the fundamental mode field given by Figure 2.11 (b), we can calculate the reflectance and transmittance of the slots as a function of the remaining cladding thickness above the slot, t, which are plotted in Figure 2.12.

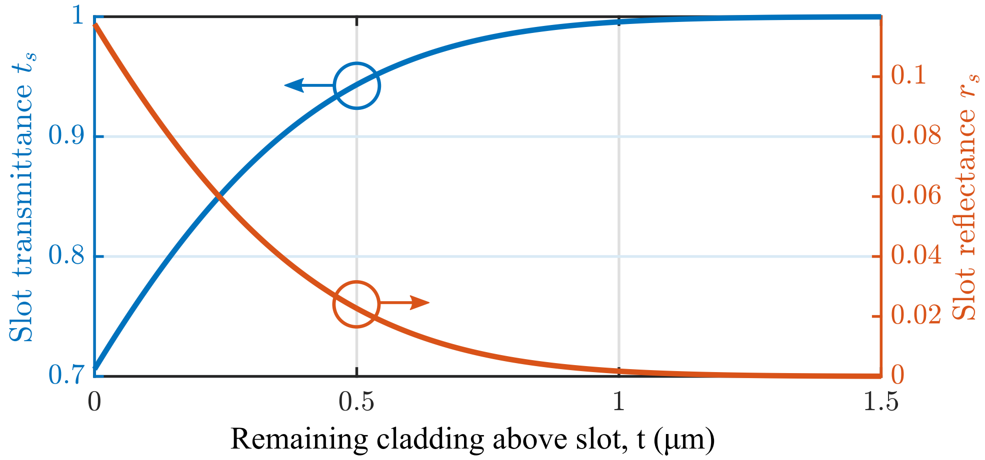

Figure 2.12: Calculated reflectance and transmittance of a slot vs remaining cladding above the slot, t

From these calculations, the highest value of the achievable slot reflectance is observed to be around 0.118, which corresponds to a transmittance value of 0.706, leading to a loss (η_s) of 0.49 . It is important to note from this discussion that loss due to the slot is directly proportional to the slot depth whereas the reflectance of the slot is inversely proportional to the slot depth. For effective single mode selection, we need high reflectance at the slot, but at the same time we also require low loss to achieve high optical output power. Hence, there is a trade-off between the single-mode behaviour and output power while choosing the etch depth of the slot. Another important aspect to be noticed is for low values of t, the slot reflectance is highly sensitive to any change in the value of t, or in other words, the any variation in the etch depth of the slot can cause a change in the mode-selection and thus the output wavelength of the laser. This limits the repeatability of the tuning characteristics for such SFP lasers during different fabrication runs for the same design, where small changes in slot etch depths can result in quite different tuning maps.

2.1.5 Modelling Slotted Lasers

Etching a reflective slot into the waveguide essentially creates sub-cavities in the optical resonator which are coupled by the underlying active region waveguide. This creates a coupled-cavity effect which is well-known in literature [19, 20]. There exist various methods to model SFP lasers based on the coupled-cavity effect. When the slots were first proposed by Coldren *et al* [1], the truncation approximation described in the previous section was used. As single-mode lasers became more widely-studied in the following decades, there was a need to model them more accurately. The first of these methods was based on one-dimensional transmission matrices [21]. This method could not estimate scattering losses and also could not match the reflection coefficient with experimental measurements [22]. An improved two-dimensional scattering matrix method was proposed later [23] which could take into account the propagation and the transverse directions simultaneously. Yet another approach to modelling SFP lasers is the Time Domain Travelling Wave (TDTW) model [24]. In this approach the time-domain coupled-wave equations are solved at many discrete points along the length of the laser cavity as illustrated in Figure 2.13.

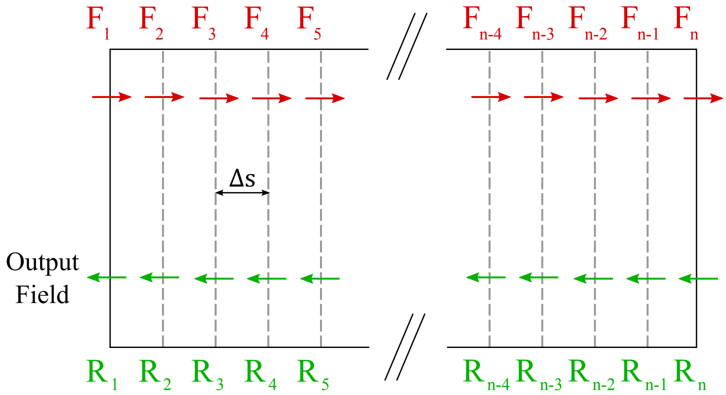

Figure 2.13: Discretisation used for the TDTW model

The forward and backward travelling fields are represented by $F(z,t)$ and $R(z,t)$ respectively, which can be written as:

$$\begin{aligned} \frac{1}{v_g}\frac{\partial F(z,t)}{\partial t} + \frac{\partial F(z,t)}{\partial z} &= (\Gamma g - \alpha - j\Delta\delta)F(z,t) + S_F(z,t) \\ \frac{1}{v_g}\frac{\partial R(z,t)}{\partial t} - \frac{\partial R(z,t)}{\partial z} &= (\Gamma g - \alpha - j\Delta\delta)R(z,t) + S_R(z,t) \end{aligned} \tag{2.17}$$

where v_g is the group velocity in the material, Γ is the optical confinement factor, g is the optical gain, α is the propagation loss in the waveguide and $\Delta\delta$ is the detuning factor. S_F and S_R are the spontaneous emission noise present in the waveguide in the forward and backward directions respectively, which is Gaussian-distributed. The time-dependent carrier rate equation is give by:

$$\frac{dN}{dt} = \frac{I}{eV} - \frac{N}{\tau} - BN^2 - CN^3 - 2v_g g\left(|F|^2 + |R|^2\right) \tag{2.18}$$

where I is the injected current, N is the carrier density, τ is the carrier lifetime,

V is the active region volume and B and C are the bimolecular and Auger recombination coefficients respectively. The optical gain g is given by:

$$g = \frac{g_N(N - N_0)}{2\left[1 + \epsilon\left(|F|^2 + |R|^2\right)\right]} \tag{2.19}$$

where g_N is the differential gain, N_0 is the transparency carrier density and ϵ is the nonlinear gain coefficient. The boundary conditions at the slot/air interface are given by the following:

$$\begin{aligned} F_m^n &= t_f F_m^{-n} - r_f^- R_m^{-n} \\ R_m^n &= t_f R_m^n + r_f^- F_m^{-n} \\ F_{m+1}^n &= t_b F_{m+1}^{-n} + r_b^+ R_{m+1}^n \\ R_{m+1}^n &= t_b R_{m+1}^n - r_b^- F_{m+1}^{-n} \end{aligned} \tag{2.20}$$

where t_f and t_b, and r_f and $r_b$are the transmittivities and reflectivities at the front and back facets of the slot respectively, with the superscripts $-$ and $+$ denoting looking from the left and right side respectively. The superscripts $-n$ and n on the optical fields denotes the time period and the subscripts denote the m^{th} and $(m+1)^{th}$ section at a slot as illustrated in Figure 2.14.

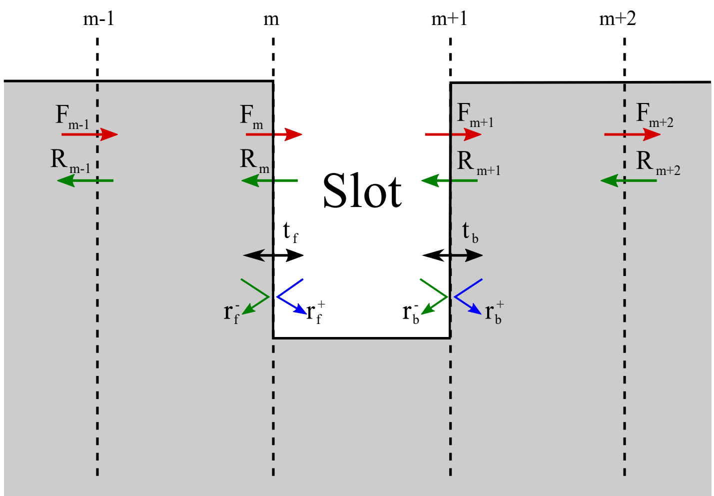

Figure 2.14: Reflection and transmission at a slot at time period n

A simulation model was implemented in MATLAB®using Equations 2.17, 2.18, 2.19 and 2.20. This model is able to generate basic characteristics of slotted Fabry-Pérot lasers that can aid in the design of such lasers. Further work is necessary in order to close the loop between simulation and experiment in order to make this model robust which is beyond the scope of this thesis work.

2.2 Etched Facets

The two important components of laser diodes are a material that provides optical gain and a mechanism for optical feedback. Typically for edge-emitting lasers the optical feedback is provided by cleaving the ends of the waveguide along the crystalline plane of the semiconductor material which results like mirror-like edges. And furthermore, after cleaving, thin-film coatings can be deposited on the facets to improve the reflectivity for greater optical feedback. Since the mirrors are essential to the working of the laser devices, this results in them not being testable on the wafer until they have been cleaved out and the coatings have been deposited. The handling of these fragile cleaved bars and testing them can lead to a significant incurred cost during mass production of such cleaved facet lasers.

An alternative to cleaved facet lasers is the *etched facet* approach. Here the mirrors are formed not by cleaving but by etching vertical facets at the end of the laser waveguides. There are numerous advantages to etched facets over cleaved facets. Since the facets are lithographically defined, the lengths of the waveguides can be controlled precisely. This eliminates errors due to mechanical cleaving of the facets. Furthermore, anti-reflection (AR) or high-reflection (HR) coatings can be deposited on the wafer instead of thin bars as is the case with the cleaved facet devices. Also, a deep facet etch exposes the underlying n-doped substrate which can be used to make n-contacts on the top side of the devices, along with the p-contacts. Having p and n contacts on the same side reduces complexity associated with wire-bonding and packaging of the device, especially for high-speed applications. Finally, as described earlier etched facets enable testing at the wafer level before dicing the devices which brings down the cost substantially [25].

In this work, etched facets not only form the end mirrors of the laser but also the separation between the laser section and the other active sections in the device such as the wavelength monitor and modulator. Although for a laser one would like to maximise the reflectivity of the facets, there could be cases where a low reflectivity is desired - such as in a Semiconductor Optical Amplifier (SOA). This can be achieved by etching the facets tilted at an angle to the waveguide and thus reduce optical feedback avoiding the creation of a resonant cavity. This is further explained in the following chapters.

2.3 Device Fabrication

2.3.1 Epitaxial Structure

The results presented in the following sections of this chapter are based on a device fabricated on a commercially available off-the-shelf wafer from the company IQE [1]. Figure 2.15 shows a schematic of the epitaxial structure. The material is based on an indium phosphide (InP) substrate and is designed to have light emission at 1.55 μm. The epitaxial structure contains five compressively strained AlInGaAs quantum wells. The upper cladding is p-doped with Zinc and is around 1.6 μm thick, with an InGaAs layer on top to facilitate good metallic contact on the p-side. The structure incorporates a thin InGaAsP layer just above the active layer which is used as an etch-stop layer while etching the ridge waveguide geometry on the structure. This is further explained in the following section along with the other process steps. The substrate is about 400 μm thick and is n-doped using silicon. Optical confinement in the vertical direction is achieved by having the active region (higher refractive index) surrounded by the upper cladding and lower substrate materials with lower refractive index. The light is confined in the lateral direction using a ridge waveguide structure. The injection current is also delivered in a confined way through the use of the ridge waveguide. Table A.1 summarises the epitaxial structure of the wafer and more comprehensive description of these layers in the epitaxial structure can be found in the appendix.

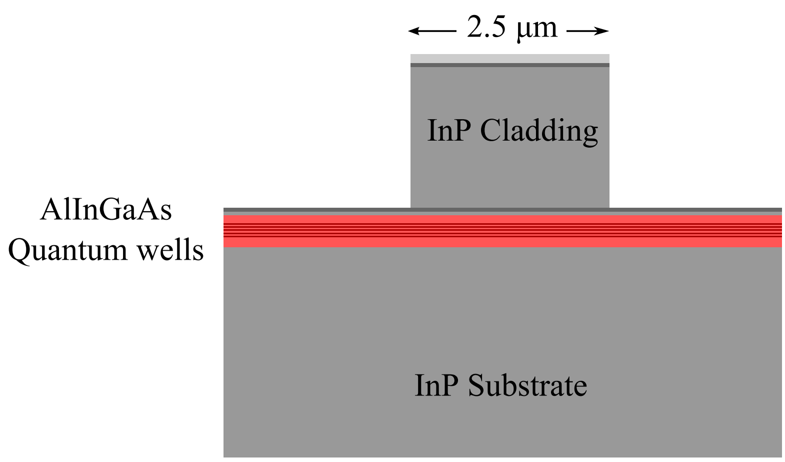

Figure 2.15: Schematic cross-section of the ridge waveguide showing the epitaxial layer structure

[1]https://www.iqep.com

The entire epitaxial growth was performed commercially at IQE before the device was processed in-house as part of this thesis work. The process flow does not involve any epitaxial re-growth, which is common to conventional tuneable laser technologies. The absence of regrowth allows the use of AlInGaAs quantum wells which have higher conduction band offset compared to InGaAsP, which leads to higher optical gain and weaker temperature dependence [26, 27]. The aluminium content would otherwise make epitaxial re-growth challenging.

Table 2.1: Epitaxial structure of laser material from IQE

Material	**x**	**y**	**Thickness (μm)**	**Dopant**
GaIn(x)As	0.53		0.2	Zinc
GaIn(x)As(y)P	0.71	0.62	0.05	Zinc
InP			1.6	Zinc
GaIn(x)As(y)P	0.85	0.33	0.02	Zinc
InP			0.05	Zinc
[Al(x)Ga]In(y)As	0.90	0.53	0.06	Zinc
[Al(x)Ga]In(y)As	0.90-0.72	0.53	0.06	Undoped
[Al(x)Ga]In(y)As	0.44	0.49	0.01	Undoped
[Al(x)Ga]In(y)As	0.24	0.71	0.006	Undoped
[Al(x)Ga]In(y)As	0.44	0.49	0.01	Undoped
[Al(x)Ga]In(y)As	0.72-0.90	0.53	0.06	Undoped
[Al(x)Ga]In(y)As	0.90	0.53	0.06	Silicon
[Al(x)Ga]In(y)As	0.90-0.86	0.53	0.01	Silicon
InP			$\sim$ 400	Silicon

2.3.2 Processing Flow

The fabrication of the lasers is done on quartered pieces of a 2-inch wafer with the epitaxial structure described above. The six main steps are described briefly below. A comprehensive description of the processing flow along with the exact parameters can be found in the appendix.

1. p-Metal Depostion

In this step, the p-contact metal on top of the ridge waveguide is deposited. This is done as the first step to help minimise the contact resistance between the p-metal and the semiconductor. A liftoff resist is spin-coated on to the wafer, above which a photoresist is spun on. A contact lithography is then performed on the photoresist using a mask aligner with UV-illumination. The photoresist is developed after the exposure, leaving the liftoff resist underneath exposed at the places where we desire the metal to be deposited. The liftoff resist is then developed using its own developer solution until it leaves a discernible undercut. 10nm of Titainum and 110nm of Gold is deposited on the whole wafer using a thermal evaporator. Finally the resists are stripped off using a photoresist-remover solution. This is schematically illustrated in Figure 2.16.

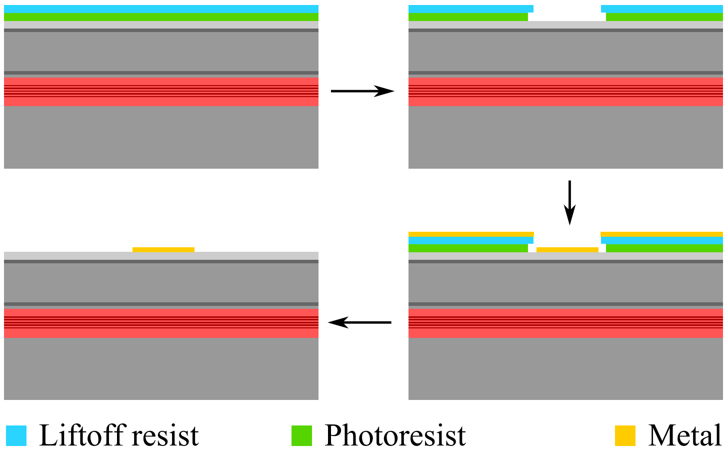

Figure 2.16: Liftoff process for p-metal deposition

2. Ridge Definition

A layer of silicon dioxide (SiO_2) is deposited over the whole wafer by the means of plasma enhanced chemical vapour deposition (PECVD). Photoresist is now spin-coated on top of the SiO_2 layer and patterned using photolithography, leaving the resist on places corresponding to the top of the ridge waveguide. Using the remaining photoresist as the mask, the SiO_2 is etched away using CF_4 and CHF_3 gases in an inductively couple plasma (ICP) etching process. Next, the photoresist is completely stripped off. We are now left with a SiO_2 hard mask protecting the top of the desired ridge waveguide. Next, the waveguide etch is etched using a mixture of Cl_2, H_2 and CH_4 gases in an ICP etcher. The etching rate of this chemistry for the semiconductor epitaxial layers is about 10 times faster than for the SiO_2 mask. This dry etch defines the ridge waveguide along with the reflective slots needed for wavelength control. We etch down to around 1.6 - 1.7 μm. This should leave us in the InP layer just above the InGaAsP layer in the epitaxial structure (Table A.1). As seen from the previous section, the depth of this etch is crucial is determining the reflectivity of the slots. In order to achieve the exact desired depth, a wet etch is carried out using a solution of phosphoric acid and hydrochloric acid (1:4 H_3PO_4:HCl). The solution selectively etches InP but not InGaAsP. Thus, we can make sure that the final depth of the ridge exactly matches up to the InGaAsP layer 1.85 μm below the top of the wafer, i.e. just above the active layer to ensure maximum slot reflectivity, with no additional optical loss. Finally, the SiO_2 hard mask is etched away using the same CF_4 and CHF_3 ICP etch as described earlier. The entire process of ridge definition is schematically illustrated in Figure 2.17. Scanning Electron Microscope (SEM) images of the etched ridge were taken in order to inspect their quality as show in Figure 2.18.

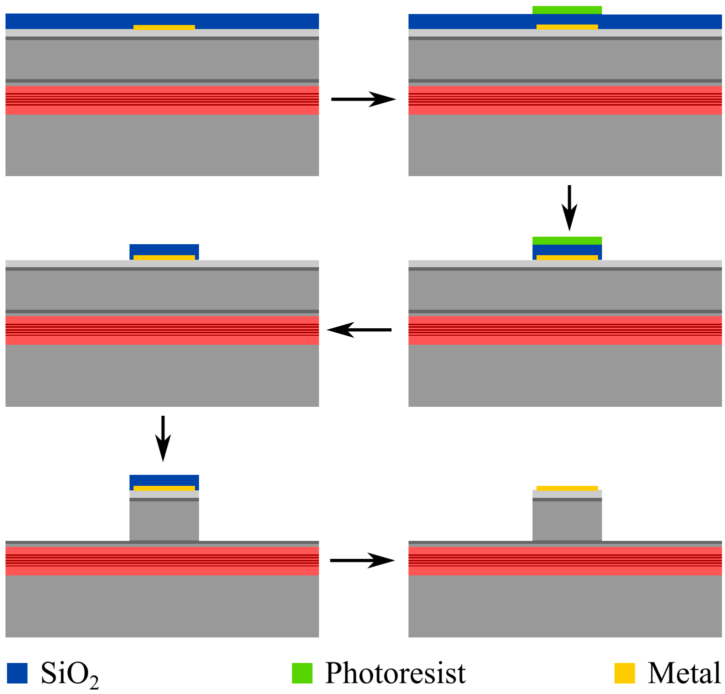

Figure 2.17: Ridge definition using an ICP etch

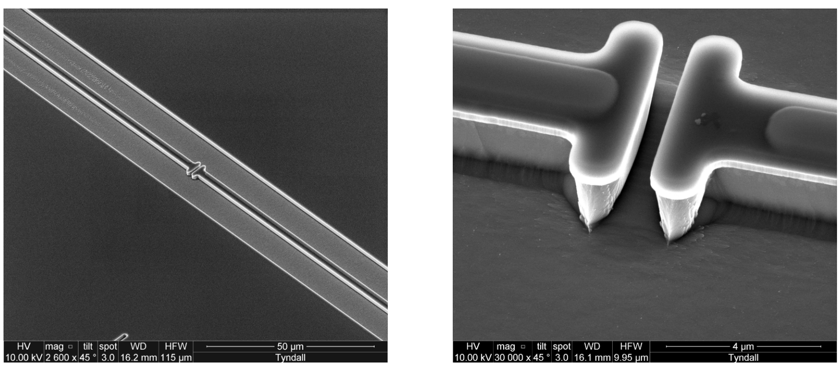

Figure 2.18: SEM images of the ridge waveguide and a slot

3. Facet Definition

Some lasers on the chip have one or both of their end mirrors using etched rather than cleaved facets. One of the reasons for having the rear mirror as an etched facet is the possibility to incorporate an integrated wavelength monitor behind the tuneable laser. The wavelength monitor is discussed in detail in the following chapter. Defining the etched facets follows a similar procedure as the ridge definition described in the previous step. A layer of SiO_2 is deposited using PECVD. A photoresist mask is then created, which helps in patterning the SiO_2 layer underneath. After the desired hard mask is created on the SiO_2 layer using a CF_4/CHF_3 ICP etch and the photoresist is stripped off, the semiconductor is etched using a Cl_2, H_2 and CH_4 ICP etch until a depth of about 5 μm. Finally, the SiO_2 hard mask is etched away. The entire process of facet definition is schematically illustrated in Figure 2.19. SEM images of the etched facet were taken in order to inspect their quality as show in Figure 2.20.

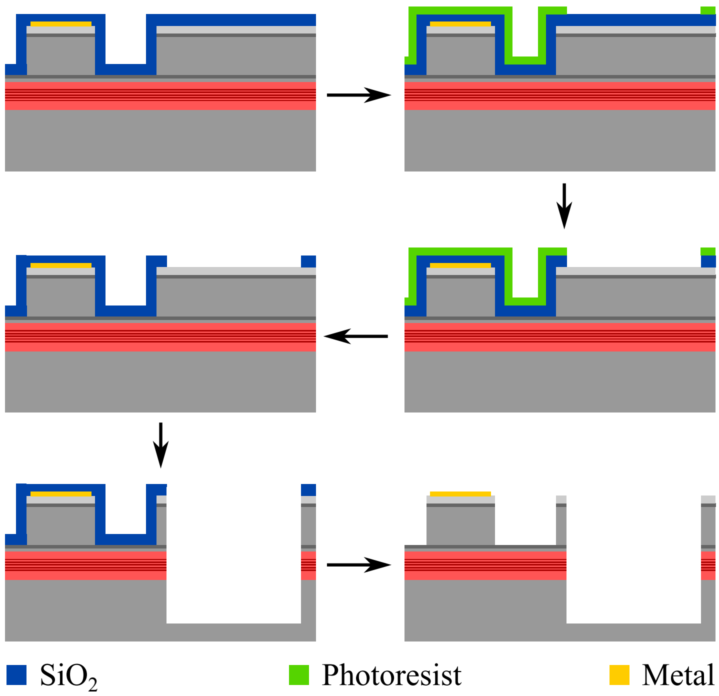

Figure 2.19: Facet definition using an ICP etch

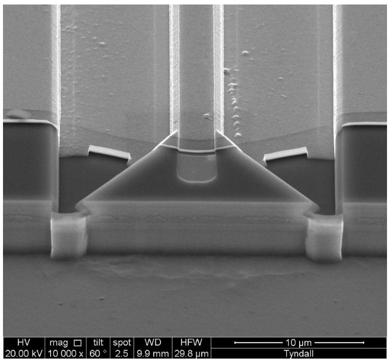

Figure 2.20: SEM image of an etched facet of the ridge waveguide laser

4. Oxide Opening

To protect the sidewalls of the ridge waveguide, the entire structure is coated with a layer of SiO_2 using PECVD. This ends up covering the top of the ridge as well which has the p-metal contact. The metal needs to be exposed and available for probing in order to send in drive currents to the laser. In order to achieve this, the SiO_2 needs to be removed from the top of the waveguide. This is done by patterning a photoresist mask by photolithography, using which the SiO_2 is etched away using a CF_4/CHF_3 ICP etch. Since this ICP etch can damage the metal contact underneath the SiO_2, care is taken such that the ICP etch is stopped with a few nanometres of SiO_2 still remaining above the metal, which will be removed in the next step before depositing the p-metal contact pads. This process of oxide opening is schematically illustrated in Figure 2.21.

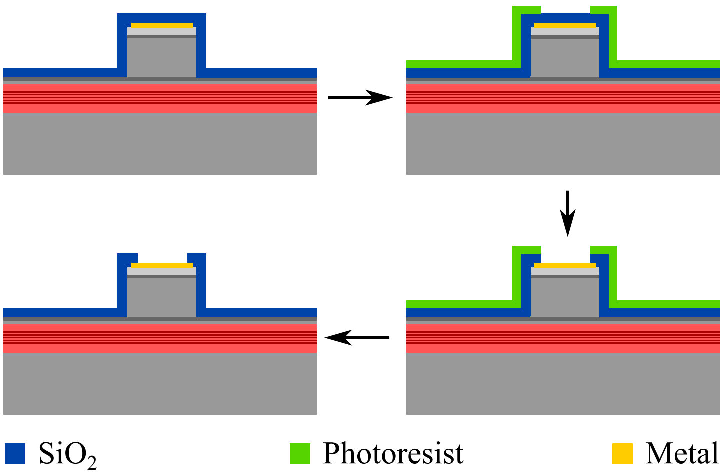

Figure 2.21: Liftoff process for p-metal deposition

5. p-Contact Pads Depostion

In this step, metal contact pads are deposited which connect to the top of the waveguide. In theory, the existing p-metal on top of the ridge can be probed to send in drive currents for the laser. But since physically probing the ridge is an extremely delicate process with a high probability of damage to the waveguide, it is better to have larger contact pads away from the ridge waveguide. This is done using a liftoff process similar to the first step in the fabrication process. A liftoff resist and a photoresist are spin-coated on the wafer and patterned. The liftoff resist is developed a little longer to leave an undercut beneath the photoresist. 10nm of Titanium and 340nm of Gold is deposited in a thermal evaporator using an angled and rotating holder, so that the metal can run along the sidewalls from the top to the bottom of the ridge. This process is schematically illustrated in Figure 2.22.

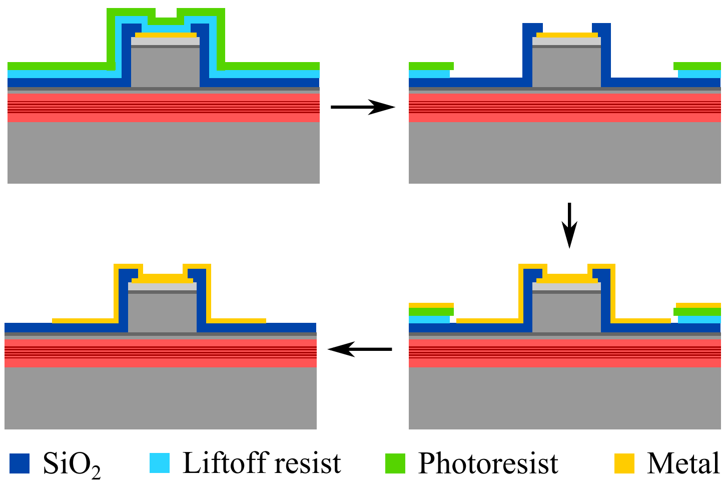

Figure 2.22: Liftoff process for p-metal contact pad deposition

6. Substrate Thinning and n-Metal Deposition

The next step of the fabrication process is to reduce the thickness of the substrate from around 400 μm to approximately 120 μm. This is essential to ensure good quality cleaving of individual devices as a thicker substrate can make the wafer hard to cleave. In order to achieve this, the wafer is first glued on to a glass carrier using black wax with its substrate facing upwards. The substrate is then treated to a Chemical Mechanical Polishing (CMP) process to get rid of its roughness using a commercially available sodium hypochlorite based polishing liquid (Logitech Chemlox). Next, the substrate is thinned using a solution of bromine and methanol (Br_2 / CH_3OH) to the desired thickness of 120

μm. Next, the n-metal, which is a combination of gold, germanium and nickel (Au:Ge:Au:Ni:Au 14:14:14:10:150nm) is deposited on to the substrate using a thermal evaporator. Finally the devices are cleaved out for further testing.

2.4 Experimental results

2.4.1 Effect of slots

To determine the effect of slot width and the number of slots on the optical characteristics, slotted Fabry-Pérot laser devices were fabricated using the process described in Section 2.3.2 with slot widths ranging from 0.8μm to 2μm, with zero slots to 8 slots equally spaced along a given length of the Fabry-Pérot cavity. The devices had a single metal contact on the p-side through which current was injected into the entire 500μm length of the Fabry-Pérot cavity. A typical device is shown in Figure 2.23. The optical output was fibre-coupled into an optical spectrum analyser. A typical optical spectrum is shown in Figure 2.24. The effect of the slots can be observed in the periodic side-bands in the spectrum. The threshold currents are plotted in Figure 2.25 (a), peak optical power in Figure 2.25 (b) while Figure 2.25 (c) shows the percentage of single-moded (with SMSR > 15dB) optical spectrum for a sweep of the injection current from 0 to 90mA in steps of 2mA.

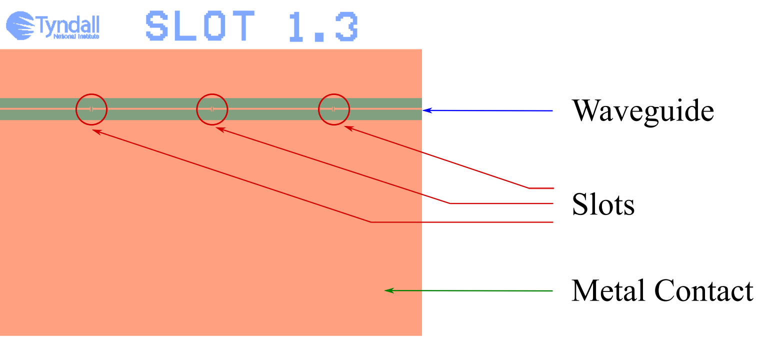

Figure 2.23: Slotted Fabry-Pérot laser of length 500μm with three slots equally spaced along the cavity and a single metal contact

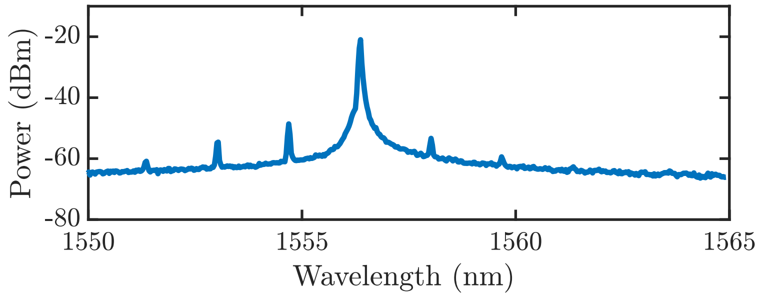

Figure 2.24: Typical optical spectrum fromn a Slotted Fabry-Pérot laser

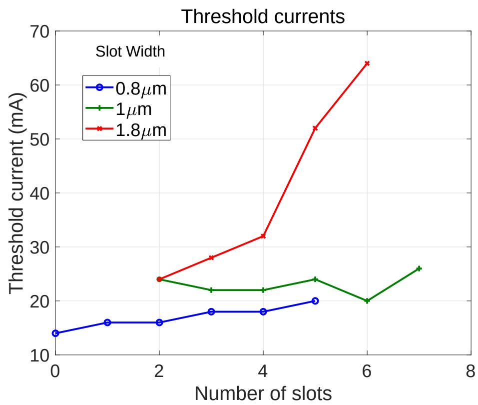

(a)

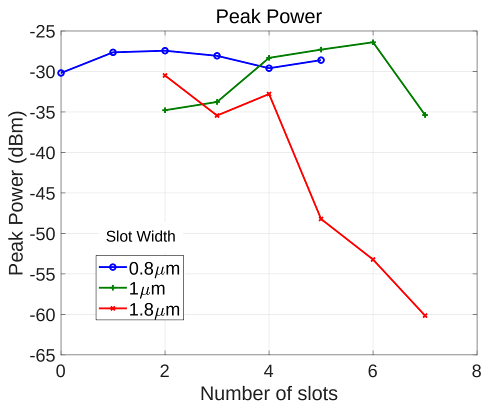

(b)

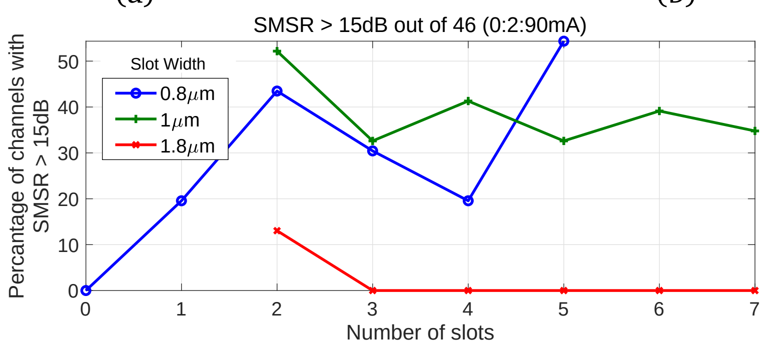

(c)

Figure 2.25: (a) Threshold current (b) Peak optical power (c) Percentage of single-mode lasing as a function of slot width and number of slots

We observe from Figure 2.25 (a) and (b) that a slot width of 1.8μm results in larger threshold currents and poor optical output power, especially as the number of slots increases. And from Figure 2.25 (c), it can be seen that slots with a width of 1.8μm perform very poorly in terms of single-modedness, whereas slots of widths around 1μm lase show better single mode lasing characteristics. From Figure 2.25 (a), (b) and (c), we can infer that slots of width of around 1μm and 2 slots along the length of the Fabry-Pérot cavity result in good performance of the device in terms of threshold current, power and single-modedness.

2.4.2 Multi-section slotted Fabry-Pérot lasers

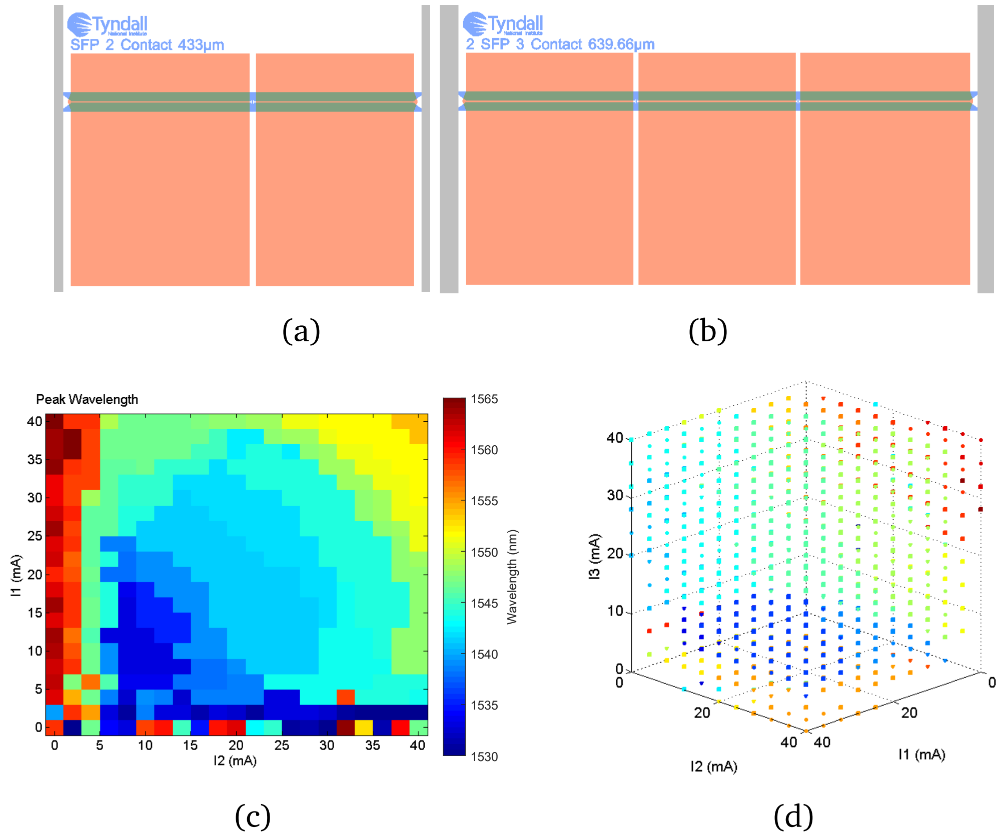

Figure 2.26: Typical (a) 2-section (b) 3-section slotted Fabry-Pérot lasers. Tuning map – peak wavelength from (c) 2-section (d) 3-section slotted Fabry-Pérot laser at 20°C

Figure 2.26 (a) shows a typical 2-section slotted Fabry-Pérot laser fabricated using the process described in Section 2.3.2. The two sections of the Fabry-Pérot cavity are separated by one slot and metal contacts on the p-side of the device are also separated so that the two sections can be injected with different currents. The lengths of the two sections are 229μm and 203μm. The lengths are chosen to be different to avoid possibility of resonances from cavities of equal length. Currents were injected into the two sections ranging from 0 to 40mA in each section in steps of 2mA. The output facet was fibre-coupled into an optical spectrum analyser. Figure 2.26 (c) shows the peak wavelength as a function of the two currents. We can observe bands of different peak wavelengths in the plot which tends to shift to longer wavelengths as the total current in the device increases. Figure 2.26 (b) shows a similar device but with 2 slots and hence 3 sections. The lengths of the sections are 215, 195, 217μm. And Figure 2.26 (d) is a 3-dimensional plot that shows the peak wavelength as a function of the three currents in the different sections of the device.

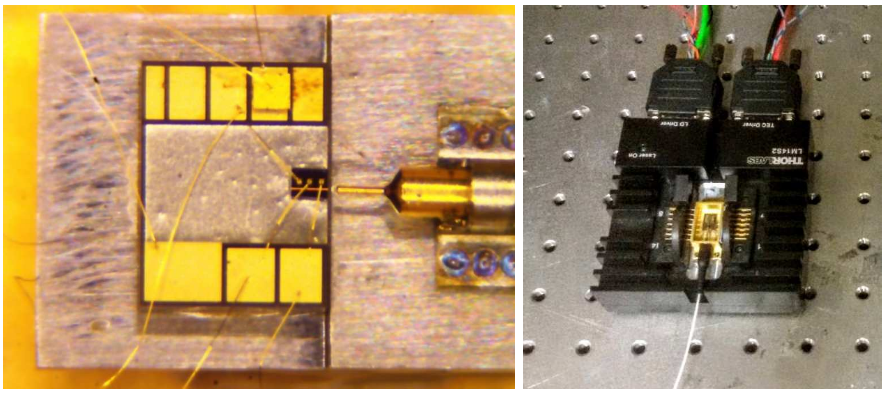

Figure 2.27: Three-section slotted Fabry-Pérot laser in a butterfly package

A 3-section slotted Fabry-Pérot device was mounted inside a butterfly package with the help of the Photonics Devices Packaging group in Tyndall National Institute. The laser chip was glued onto an Aluminium Nitride submount containing a thermo-electric cooler (TEC), a lensed-fibre was aligned to its facet and its contact pads were wire-bonded to the arms of the butterfly package. A picture of this package is shown in Figure 2.27. The currents in the three sections of the laser were varied between 0 and 40mA in steps of 2mA. The resultant wavelength channels are shown in Figure 2.28. This is a coarse sweep that shows the range and behavior of a typical device. It should be noted that there are considerable gaps in the tuning maps which can be accessed by a smaller step size in the current sweep which takes considerably longer to obtain. For instance, a sweep between 0 and 40mA with a step size of 2mA for the three currents results in a dataset with 9261 points (21x21x21) which takes about 3.5 hours to run. The bottleneck is the sweep of the OSA which takes about 1.3 seconds. A sweep with a smaller step size of 1mA was executed taking about 28 hours that resulted in a dense channel map as shown in Figure 2.29 (a).

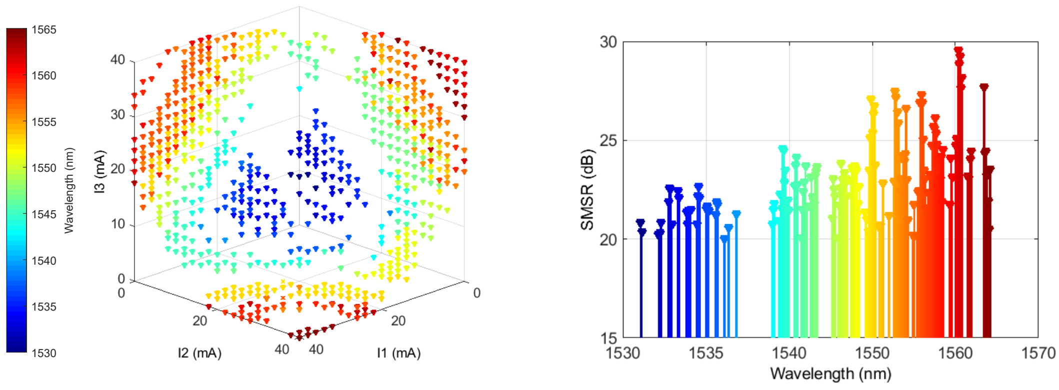

(a) (b)

Figure 2.28: (a) Tuning map – peak wavelength as a function of three section currents and (b) the corresponding wavelength channels and their SMSRs

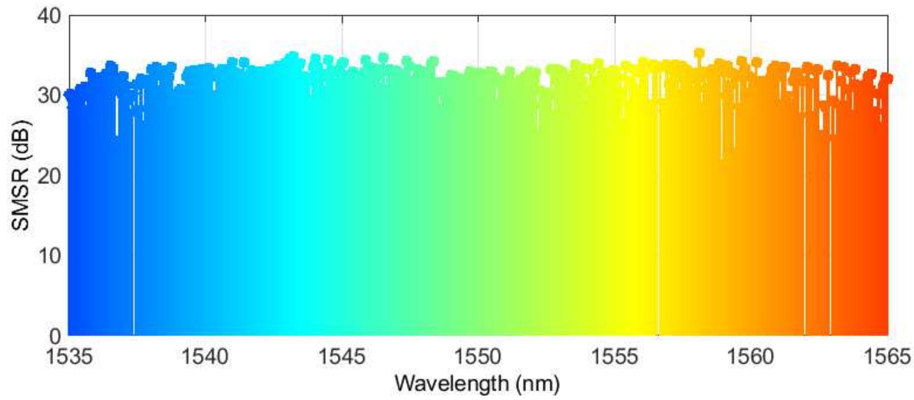

(a)

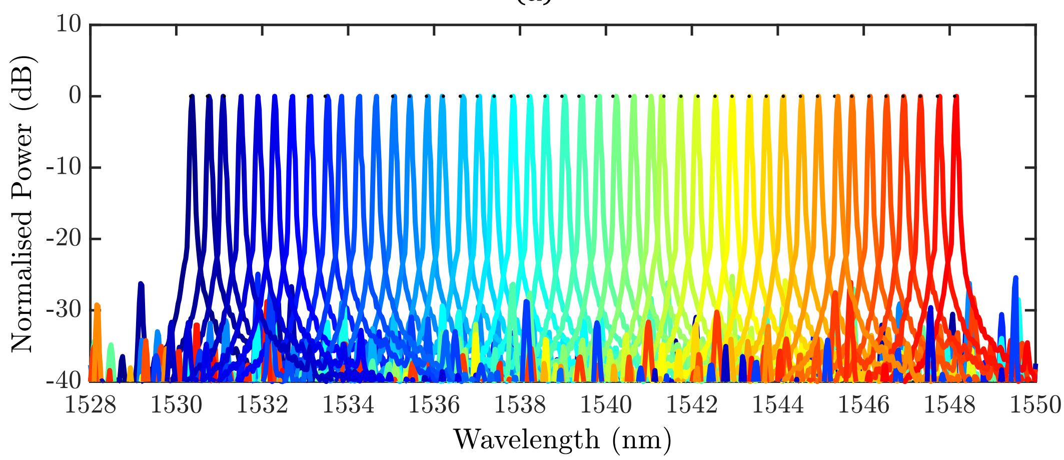

(b)

Figure 2.29: (a) Dense wavelength channels and (b) channels from the ITU-T 50 GHz grid obtained using the 3-section slotted Fabry-Pérot laser mounted in the butterfly package

For telecommunication applications, it is useful to have the laser tuned to the standard wavelengths set by the International Telecommunication Union (ITU-T) [28]. From the dense channel map in Figure 2.29(a), it is evident that wavelengths close to these channels can be obtained for certain values of current combinations. When tuning the three currents is not enough to exactly hit a wavelength channel in the ITU-T grid, the temperature of the device can be altered by controlling the TEC making this a fine-tuning control knob in addition to the currents. Figure 2.29(b) shows the resultant spectra of the all the channels of the ITU-T 50GHz grid in the lower half of the C-band by using the temperature control between 16C and 22C. The obtained SMSRs for all the channels were near 30 dB making this a good candidate for a tuneable laser in telecommunication applications.

2.5 Summary

In this chapter, the theory behind slotted Fabry-Pérot lasers was presented explaining the benefits of a multi quantum well layer structure to obtain good optical gain and waveguiding, and how slots along the waveguide introduce reflections that aid in longitudinal mode selection. A time-domain travelling wave model was presented that can simulate the behaviour of slotted lasers. The steps involved in the fabrication of the device were presented in detail. Finally, experimental results were presented showing a tuneable slotted slotted Fabry-Pérot laser mounted on a butterfly package being able to tune across about 20nm covering half the C-band. It should be noted that although Figure 2.29 can be reproduced for devices across different fabrication runs, the exact drive currents needed to produce a certain wavelength channel cannot be reproduced consistently. This is due to several factors like slot etch depth, the precision of the injection currents and temperature of the different sections. Reproducibility of the slot etch depth can be addressed through finer fabrication control - for example by use of end-point detection systems during the slot etch. Injection current steps of 1 - 2 mA were used in these plots in order to reduce data collection time. Finer adjustment of injection currents may possibly reveal further clues in order to achieve better reproducibility. Further investigation is also required into the self-heating of the different sections leading to varying localised thermal profiles, which also affects reproducibility. It should also be noted that the linewidth of the laser was not measured as part of this thesis work. The results from this chapter show that these lasers can be used as a low-cost solution for telecom lasers especially in the optical networking units (ONUs) in next-generation passive optical networks (NG-PONs). For a more complete solution for an optical transmitter in the ONUs, these lasers need to be integrated with a modulator and also wavelength monitoring / locking device. In the following chapters, integration of these components with the slotted Fabry-Pérot lasers is discussed in detail.

References

[1] L. Coldren, K. Ebeling, B. Miller, and J. Rentschler, "Single longitudinal mode operation of two-section GaInAsP/InP lasers under pulsed excitation," *IEEE Journal of Quantum Electronics*, vol. 19, pp. 1057–1062, June 1983.

[2] B. Corbett and D. McDonald, "Single longitudinal mode ridge waveguide 1.3 μm fabry-perot laser by modal perturbation," *Electronics Letters*, vol. 31, pp. 2181–2182, Dec 1995.

[3] W. Guo, Q. Lu, M. Nawrocka, A. Abdullaev, J. O'Callaghan, M. Lynch, V. Weldon, and J. F. Donegan, "Integrable Slotted Single-Mode Lasers," *IEEE Photonics Technology Letters*, vol. 24, pp. 634–636, April 2012.

[4] R. N. Hall, G. E. Fenner, J. D. Kingsley, T. J. Soltys, and R. O. Carlson, "Coherent light emission from GaAs junctions," *Phys. Rev. Lett.*, vol. 9, pp. 366–368, Nov 1962.

[5] M. I. Nathan, W. P. Dumke, G. Burns, F. H. D. Jr., and G. Lasher, "Stimulated emission of radiation from GaAs p-n junctions," *Applied Physics Letters*, vol. 1, no. 3, pp. 62–64, 1962.

[6] H. Kroemer, "Zur theorie des diffusions und des drifttransistors; III. dimensionierungsfragen," *Arch. Elektr. Übertrag*, vol. 8, pp. 499–504, 1954.

[7] H. Kroemer, "The Double-Heterostructure Concept: How It Got Started," *Proceedings of the IEEE*, vol. 101, pp. 2183–2187, Oct 2013.

[8] H. Kroemer, "A proposed class of hetero-junction injection lasers," *Proceedings of the IEEE*, vol. 51, pp. 1782–1783, Dec 1963.

[9] Z. I. Alferov and R. F. Kazarinov. Author's certificate no. 1032155/26-25 USSR, 1963.

[10] I. Hayashi, M. B. Panish, P. W. Foy, and S. Sumski, "Junction lasers

which operate continuously at room temperature," *Applied Physics Letters*, vol. 17, no. 3, pp. 109–111, 1970.

[11] Z. I. Alferov, V. M. Andreev, D. Z. Garbuzov, Y. V. Zhilyaev, E. P. Morozov, E. L. Portnoi, and V. G. Trofim, "Investigation of the influence of the AlGaAs-GaAs heterostructure parameters on the laser threshold current and the realization of the continuous emission at the room temperature," *Sov. Phys. Semiconductors*, vol. 4, 1970. Translated from Fiz. Tekh. Poluprovodn. 4.

[12] J. Buus, M. Amann, and D. Blumenthal, *Tunable Laser Diodes and Related Optical Sources*. Wiley, 2005.

[13] T. Higashi, S. J. Sweeney, A. F. Phillips, A. R. Adams, E. P. O'Reilly, T. Uchida, and T. Fujii, "Observation of reduced nonradiative current in 1.3μm AlGaInAs-InP strained MQW lasers," *IEEE Photonics Technology Letters*, vol. 11, pp. 409–411, April 1999.

[14] Y.-K. Kuo, S.-H. Yen, M.-W. Yao, M.-L. Chen, and B.-T. Liou, "Numerical study on gain and optical properties of AlGaInAs, InGaNAs, and InGaAsP material systems for 1.3μm semiconductor lasers," *Optics Communications*, vol. 275, no. 1, pp. 156 – 164, 2007.

[15] D. Botez, "Analytical approximation of the radiation confinement factor for the TE_0 mode of a double heterojunction laser," *IEEE Journal of Quantum Electronics*, vol. 14, pp. 230–232, April 1978.

[16] R. People and J. C. Bean, "Calculation of critical layer thickness versus lattice mismatch for Ge_xSi_{1-x}/Si strained layer heterostructures," *Applied Physics Letters*, vol. 47, no. 3, pp. 322–324, 1985.

[17] P. J. A. Thijs, L. F. Tiemeijer, P. I. Kuindersma, J. J. M. Binsma, and T. V. Dongen, "High-performance 1.5μm wavelength InGaAs-InGaAsP strained quantum well lasers and amplifiers," *IEEE Journal of Quantum Electronics*, vol. 27, pp. 1426–1439, Jun 1991.

[18] W. T. Tsang, "A graded-index waveguide separate confinement laser with very low threshold and a narrow Gaussian beam," *Applied Physics Letters*, vol. 39, no. 2, pp. 134–137, 1981.

[19] W. T. Tsang, N. A. Olsson, R. A. Logan, J. A. Ditzenberger, I. P. Kaminow, and J. Ko, "Single-longitudinal-mode performance character-

istics of cleaved-coupled-cavity lasers," *Applied Physics Letters*, vol. 43, no. 11, pp. 1003–1005, 1983.

[20] L. A. Coldren, S. W. Corzine, and M. L. Mašanović, *Photonic Integrated Circuits*, ch. Eight, pp. 451–507. Wiley-Blackwell, 2012.

[21] S. O'Brien and E. P. O'Reilly, "Theory of improved spectral purity in index patterned Fabry-Pérot lasers," *Applied Physics Letters*, vol. 86, no. 20, p. 201101, 2005.

[22] P. Lambkin, C. Percival, and B. Corbett, "Reflectivity measurements of intracavity defects in laser diodes," *IEEE Journal of Quantum Electronics*, vol. 40, pp. 10–17, Jan 2004.

[23] Q. Y. Lu, W. H. Guo, R. Phelan, D. Byrne, J. F. Donegan, P. Lambkin, and B. Corbett, "Analysis of Slot Characteristics in Slotted Single-Mode Semiconductor Lasers Using the 2-D Scattering Matrix Method," *IEEE Photonics Technology Letters*, vol. 18, pp. 2605–2607, Dec 2006.

[24] J. Zhao, K. Shi, Y. Yu, and L. P. Barry, "Theoretical Analysis of Tunable Three-Section Slotted Fabry-Perot Lasers Based on Time-Domain Traveling-Wave Model," *IEEE Journal of Selected Topics in Quantum Electronics*, vol. 19, pp. 1–8, Sept 2013.

[25] P. Vettiger, M. K. Benedict, G. L. Bona, P. Buchmann, E. C. Cahoon, K. Datwyler, H. P. Dietrich, A. Moser, H. K. Seitz, O. Voegeli, D. J. Webb, and P. Wolf, "Full-wafer technology-a new approach to large-scale laser fabrication and integration," *IEEE Journal of Quantum Electronics*, vol. 27, pp. 1319–1331, Jun 1991.

[26] C.-E. Zah, R. Bhat, B. N. Pathak, F. Favire, W. Lin, M. C. Wang, N. C. Andreadakis, D. M. Hwang, M. A. Koza, T.-P. Lee, Z. Wang, D. Darby, D. Flanders, and J. J. Heieh, "High-performance uncooled 1.3 μm $Al_xGa_yIn_{1-x-y}As$/InP strained-layer quantum-well lasers for subscriber loop applications," *IEEE Journal of Quantum Electronics*, vol. 30, pp. 511–523, Feb 1994.

[27] J. C. L. Yong, J. M. Rorison, R. V. Penty, and I. H. White, "Material gain comparison for InGaAsP, AlGaInAs and InGaAsN for 1.3 micron laser diode," in *Technical Digest. Summaries of papers presented at the Conference on Lasers and Electro-Optics. Postconference Technical Digest (IEEE Cat. No.01CH37170)*, pp. 479–480, May 2001.

[28] "G.694.1: Spectral grids for WDM applications: DWDM frequency grid." `https://www.itu.int/rec/T-REC-G.694.1/`. (Accessed on 01-Sep-2019).

Chapter 3

Wavelength monitoring

Due to the ever-increasing demand for bandwidth, Wavelength Division Multiplexing (WDM) and Dense-WDM (DWDM) optical communication systems have now become very prevalent. To maintain low inter-channel crosstalk, ITU-T standards for wavelength stability in DWDM systems can sometimes be as low as $\pm$20pm for 50 GHz grid spacing and even $\pm$10pm for 25 GHz grid spacing [1]. This means that the wavelength of the laser source needs to be monitored very carefully. Even fixed-wavelength single mode lasers can exhibit their wavelengths drifts over time due to temperature changes, ageing or change in drive currents, and in the case of tuneable lasers, which are the ones most commonly used in WDM networks the case for the monitoring their wavelengths becomes even more obvious due to the presence of multiple wavelengths.

This chapter introduces and compares various existing technologies used for wavelength monitoring, and a low-cost monolithically integrable structure is proposed for the same. The theory of operation is presented along with experimental characterisation discussing various aspects such as power, polarisation and temperature stability.

3.1 Existing technologies

In a laboratory setup, Optical Spectrum Analysers (OSAs) are usually used to measure the wavelength of an optical signal. Typically, OSAs have a fiberised input connection which feeds the light into a rotating grating and fixed detector setup. Other than being very bulky and expensive, they often require frequent calibration as their wavelength sensitivity can drift. Hence, these are not ideal candidates for deployment in the field. The following paragraphs describe existing devices for wavelength monitoring which are compact and more feasible for integration with the current telecommunication systems and mostly based on semiconductor technologies.

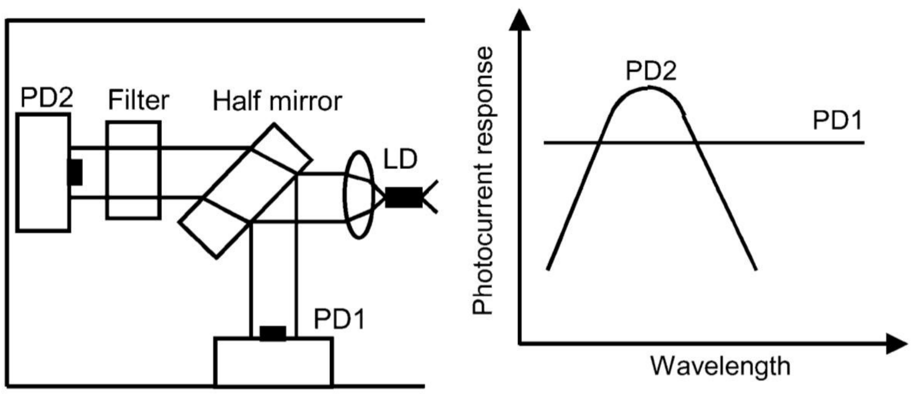

(a) (b)

Figure 3.1: Schematic of a typical FP etalon based wavelength monitoring scheme [2]

Wavelength monitoring schemes can broadly be classified into two sorts: in-package and on-chip. In-package schemes employ wavelength measuring devices within the package assembly of the laser / transmitter, whereas on-chip schemes employ fully integrated devices which are present on the same chip as the laser source. Typically in the case of in-package schemes, the light is coupled from the source to the wavelength monitor either using bulk optics such as lenses or fibres. Figure 3.1 (a) shows a typical in-package wavelength monitoring / stabilising scheme using a wavelength selective filter [3]. In this case, the laser output light is split into two parts with one part passing through the wavelength filter. The optical power is measured using a photodetector in each of the arms. Comparing the ratio of the powers with and without the filter, it is possible to ascertain the operating wavelength as illustrated in Figure 3.1 (b). Among in-package solutions, some of the common schemes used as wavelength filters are Fabry-Pérot etalons [3], fibre gratings [4] and birefringent filters [5]. On the other hand, on-chip wavelength measurement schemes typically utilise wavelength selective elements like interferometric couplers [6, 7] or arrayed waveguide gratings (AWGs) [8]. These elements usually need to be optically passive since the measurement technique for the wavelength exploits the transparent nature of the material. Table 3.1 summarises the key characteristics of the different type of wavelength monitoring schemes in the literature.

Table 3.1: Comparison of different wavelength monitors

Type	**Size**	**Sensitivity**	**Reference**
In-package			
FP etalon	$\sim$5 mm	4 pm	[3]
Fibre grating	$\sim$20 mm	10 pm	[4]
Birefringent filter	$\sim$5 mm	7 pm	[5]
On-chip			
Interferometric coupler 1	0.05 mm^2	0.44 nm	[6]
Interferometric coupler 2	0.01 mm^2	0.2 nm	[7]
AWG	$\sim$1 mm^2	20 pm	[8]

In case of in-package solutions, the cost is driven higher due to the use of bulk optics and its associated costs with alignment and packaging. On the other hand, most of the on-chip solutions employ active and passive components on the same chip. This requires the use of spatially selective bandgap engineering techniques like epitaxial regrowth or quantum well intermixing. To monitor and stabilise the wavelengths of the sources in a WDM system, in-package solutions such similar to the one shown in figure 3.1 are most commonly used in practice. Since the tuneable sources in current-generation optical networks are usually present on the optical line termination (OLT) side, which is in the business end of the network, the extra costs associated with the alignment and packaging of these wavelength monitoring schemes is not of huge concern. Some commercial examples of a tuneable laser integrated with a wavelength monitor at a package level which are widely used in practice are the JDSU-4245 [9] which costs about $2650 and Finisar's S7500 [10] which costs about $2300, both of which are based on a FP etalon based configuration. It is obvious that with price tags such as these it would be highly impractical to have these in devices at consumers' premises. To keep the costs as low as possible and in the range of a few dollars / euros, it is essential that both the laser and wavelength monitor are integrated on the same chip and furthermore that cost saving techniques are employed such as regrowth-free monolithic integration, foundry-compatible fabrication processes and avoidance of use of bulk optics. A wavelength monitoring solution addressing these issues is presented in the following sections of this chapter.

3.2 2-section Wavelength Monitor

An inline quauntum-well photodetector based device was first proposed by Wu *et al* [11]. The incoming light is coupled into the waveguide which consists of a pair of inline photodiodes (Figure 3.2). A fraction of this incoming light is absorbed in the first section, and the rest is transmitted through to the second section where it gets absorbed. These photocurrents generated by this absorption in the two sections can be measured. Near the material's band-edge, its transparency goes from opaque to transparent as the wavelength increases. This means that, for shorter wavelengths, the light will be absorbed more in the first section and for longer wavelengths, the light will travel further to the second section, making the ratio of the photocurrents a very sensitive indicator of the wavelength as shown in figure 3.3.

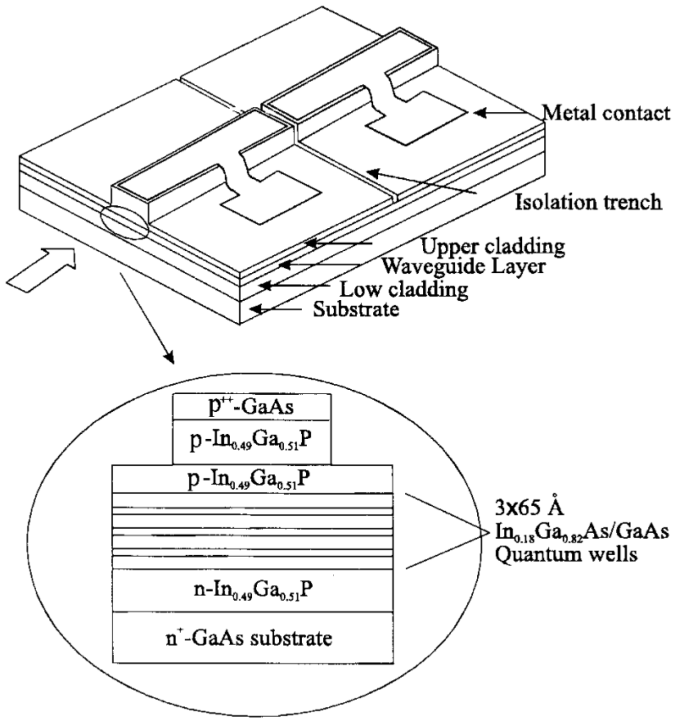

Figure 3.2: An inline quantum well photodetector based device for wavelength monitoring[11]

The following section outlines the theory behind the operation of this two section wavelength monitor.

3.2.1 Theory of operation

To calculate the photocurrents generated in a waveguide photodetector we define Responsivity, $\mathcal{R}$, which is the generated photocurrent per unit of optical power, as follows [12]

$$\mathcal{R} = \frac{I}{P} = \frac{e}{h\nu}\eta_{ext} \tag{3.1}$$

where I is the generated photocurrent, P is the optical power, η_{ext} is the external quantum efficiency and h is the Planck's constant and ν is the optical frequency. In terms of the wavelength of light, Equation 3.1 can be written as:

$$\mathcal{R} = \frac{e\lambda}{hc}\eta_{ext} \tag{3.2}$$

The external quantum efficiency, η_{ext} can be written as [12]:

$$\eta_{ext} = \frac{\Gamma\alpha^{int}}{\alpha}\eta(1 - e^{-\alpha L}) \tag{3.3}$$

where Γ is the optical confinement factor, α^{int} is the interband absorption coefficient of the quantum wells, L is the waveguide length, η is the internal quantum efficiency and α is the total loss coefficient of the propagating mode through the waveguide. Assuming the device is operating in a standalone setting, the coupling coefficient κ into the waveguide from an external fibre and the reflection of the facet, R, can be included in equation 3.3 and can be rewritten as:

$$\eta_{ext} = \kappa(1 - R)\frac{\Gamma\alpha^{int}}{\alpha}\eta(1 - e^{-\alpha L}) \tag{3.4}$$

Combing equations 3.2 and 3.4, the generated photocurrent is given by:

$$I = \frac{e\lambda}{hc}P\kappa(1 - R)\frac{\Gamma\alpha^{int}}{\alpha}\eta(1 - e^{-\alpha L}) \tag{3.5}$$

Considering a multi segment photodetector, the optical power reaching the i'th segment, P_i is given by:

$$P_i = Pe^{-\sum_{k=1}^{i-1}\alpha_k(\lambda)L_k} \tag{3.6}$$

where P is the input optical power and α_k and L_k are the absorption coefficient and the length of the k'th segment respectively. Combining equations 3.5 and 3.6, we obtain the generated photocurrent in the i'th segment as:

$$I_i = \frac{e\lambda}{hc}P\kappa(1 - R)\eta\frac{\Gamma\alpha^{int}(\lambda)}{\alpha(\lambda)}e^{-\sum_{k=1}^{i-1}\alpha_k(\lambda)L_k}(1 - e^{-\alpha_i(\lambda)L_i}) \tag{3.7}$$

Considering a two segment photodetector with equal lengths, ignoring any scattering losses between the two sections, and assuming a single pass of the optical field with negligible reflection from the back facet, the photo-currents in the front (I_{front}) and rear (I_{rear}) sections can be written, from equation 3.7, as

$$\begin{aligned} I_{front} &\propto \lambda(1 - e^{-\alpha(\lambda)L}), \\ I_{rear} &\propto \lambda(1 - e^{-\alpha(\lambda)L})e^{-\alpha(\lambda)L} \end{aligned} \tag{3.8}$$

and the photocurrent ratio between the two sections is given by

$$\frac{I_{rear}}{I_{front}} = e^{-\alpha(\lambda)L} \tag{3.9}$$

Using Urbach's empirical rule [13] for $\alpha(\lambda)$ near the band edge,

$$\alpha(\lambda) \propto e^{\left(\frac{E(\lambda)-E_g}{kT}\right)} \tag{3.10}$$

the photocurrents obtained from equations 3.8 and 3.9 are plotted in Figures 3.3(a) and 3.3(b) respectively, where $E(\lambda)$ is the photon energy, E_g is the bandgap, k is Boltzmann's constant and T is the temperature.

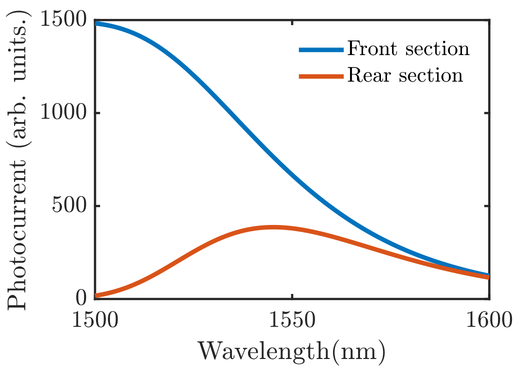

(a)

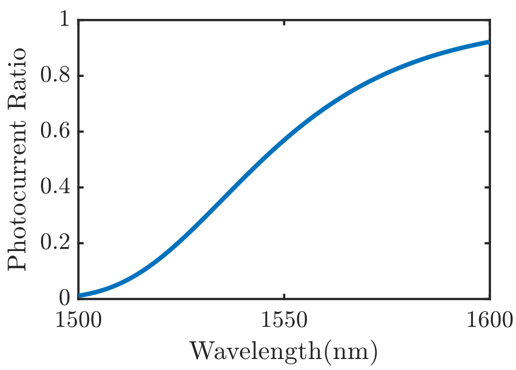

(b)

Figure 3.3: (a) Simulated photocurrents in the two sections and (b) Photocurrent ratio calculated theoretically in a 2-section wavelength monitor

From equation 3.9 it is evident that this photocurrent ratio is independent of many factors such as input optical power, coupling efficiency, facet reflections and dependent only on the absorption coefficient and the lengths of the photodetector segments. Since the absorption coefficient α is strongly dependent on the wavelength near the band edge, this ratio provides a sensitive measure of the wavelength. However, it is important to note that this relation of the photocurrent ratio to the band edge could lead it to be dependent on polarisation, since the epitaxial material structure could have different band edges for different optical polarisations.

3.2.1.1 Sensitivity analysis

In the previous section, the physics behind the ideal performance of a 2-section wavelength monitor was discussed. When it comes to practical use in the real world, non-idealities in the device must also be considered.

In a scenario where the two sections of the device would have asymmetric response to the incident optical field, the photocurrent ratio will be affected. For example, an unbalanced electrical leakage current in the two sections or unsaturable waveguide losses will have a wavelength-independent term in the expression for photocurrent in equation 3.7. Accounting for this, the simulated photocurrents and the photocurrent ratio are plotted in Figure 3.4 (a) and (b) respectively.

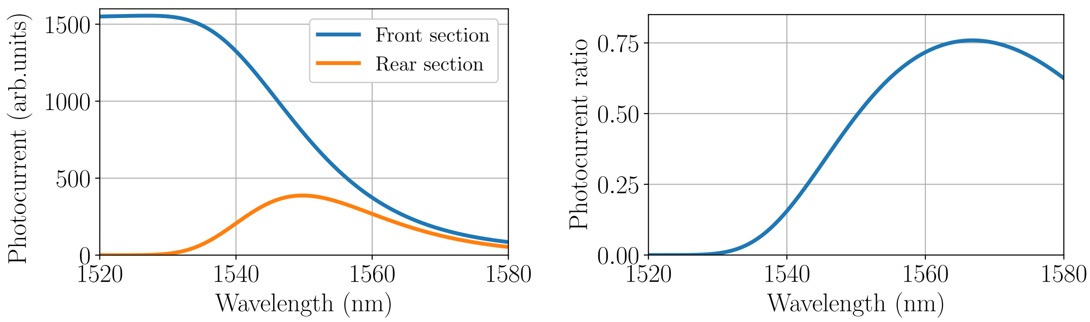

(a) (b)

Figure 3.4: (a) Simulated photocurrents in the two sections and (b) Photocurrent ratio calculated theoretically with a non-ideal asymmetry between the two sections

This non-ideality causes the photocurrents in the two sections not to converge at longer wavelengths and in turn the photocurrent ratio experiences a roll-off. Although it is interesting to understand this scenario, the actual operating wavelength range in our case is below this roll-off. Hence, this would not affect the performance of the wavelength monitor adversely. The other important factor to consider is the operating temperature of the device. The bandgap of the quantum well materials shifts with temperature and this results in change in the absorption spectrum $\alpha(\lambda)$ in equation 3.10. The shift in bandgap with temperature can be modelled using the relation proposed by Varshni[14]:

$$E_g(T) = E_g(0) - \frac{\gamma T^2}{T + \delta} \tag{3.11}$$

Substituting values for the parameters $E_g(0) = 0.811$, $\gamma = 3.4 \times 10^{-4}$ and $\delta = 50$ from literature[15] for InGaAsP/InP into equation3.11 and plugging in the resulting $E_g(T)$ into equation3.10, we can simulate the photocurrent ratio for different temperatures as shown in Figure 3.5 (a).

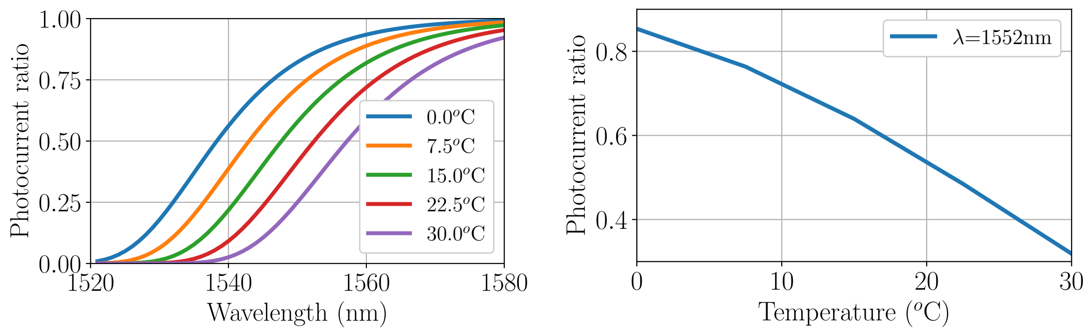

(a) (b)

Figure 3.5: Simulated photocurrent ratio as a function of (a) wavelength for different temperatures (b) temperature for a particular wavelength

We observe that the photocurrent ratio curve shifts to longer wavelengths with increase in temperature. This is to be expected since the bandgap decreases, i.e. shifts to longer wavelengths with increase in temperature. For a constant wavelength (1552 nm), the photocurrent ratio is plotted versus temperature in Figure 3.5 (b). Approximating a linear behaviour, the ratio changes by about 0.018 per degree Celsius. This translates into a wavelength 'error' of about 0.5 nm or 62 GHz which is a very considerable amount. We can conclude from this analysis that temperature control of this device is of critical importance.

Other than temperature, the bandgap of the quantum well material is also different for different polarisations of the incident optical field. This polarisation dependence of the bandgap is a function of the nature and amount of strain the the quantum well layers. This means that, in theory, it could be possible to get rid of the polarisation dependence of the wavelength monitor if we could engineer a correct amount of tensile strain on the wells to match the TE and TM bandgaps with each other.

3.2.2 Standalone Performance

The 2-section wavelength monitor was fabricated using the process described in Chapter 2 as a standalone device. Light from an Agilent 81600B Tuneable Laser Source (TLS) was passed through a polarisation controller to select pure TE polarised light was injected into the device via a lensed fibre. The two sections of the device were biased at 0 Volts and the generated photocurrents were read out using a Keithley SourceMeter®. The schematic of this measurement setup is shown in Figure 3.6. The wavelength of the TLS was swept keeping the optical power constant at a value of 1mW and the resulting photocurrents and the photocurrent ratio are plotted in Figure 3.7. Comparing this with Figure 3.3, we can see good agreement between the theoretical and experimentally obtained performance of the wavelength monitor. Additionally comparing with Figure 3.4, we observe the the currents in the two sections not converging to the same value thus resulting in a rollover for the photocurrent ratio as predicted by the simulations described in the previous section.

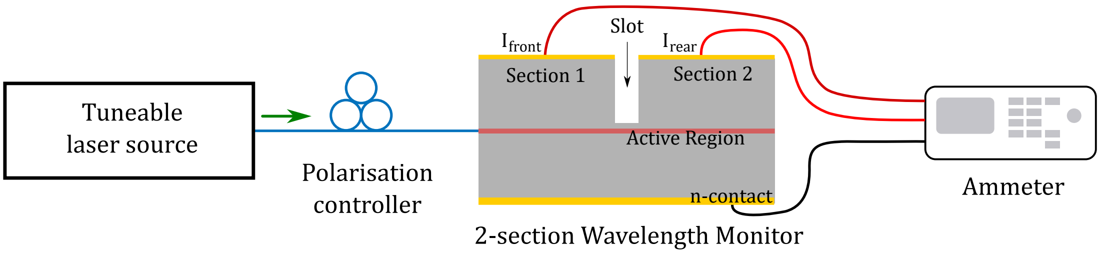

Figure 3.6: Schematic of the measurement setup

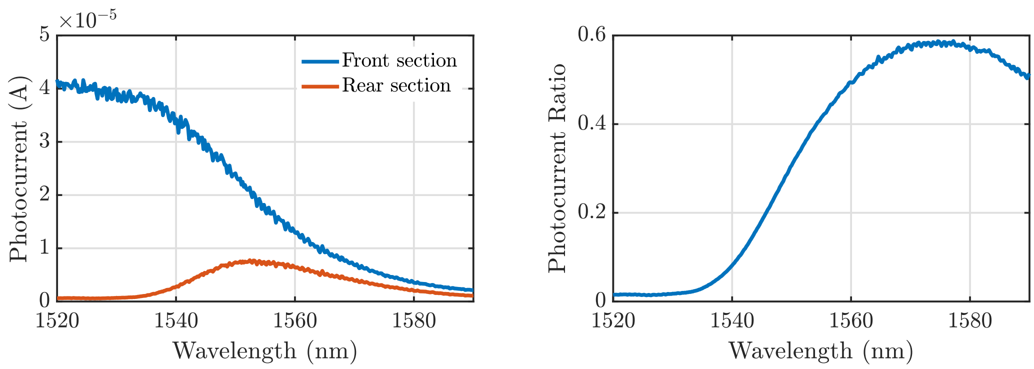

(a) (b)

Figure 3.7: (a) Photocurrents from front and rear sections and (b) Ratio of photocurrents as a function of wavelength at 20^{o}C

According to equation 3.9, the photocurrent ratio is theoretically independent of optical input power. This was tested and plotted in Figure 3.8. We observe that while the photocurrents in the individual sections go down as the input power decreases, the ratio between them remains constant and thus independent of the optical power, thus making it a robust indicator for sensing the input wavelength. Once again, the rollover behaviour at longer wavelengths is observed in the same proportion for all optical powers, hinting that this rollover is most probably caused by as asymmetrical electrical leakage current between the two sections.

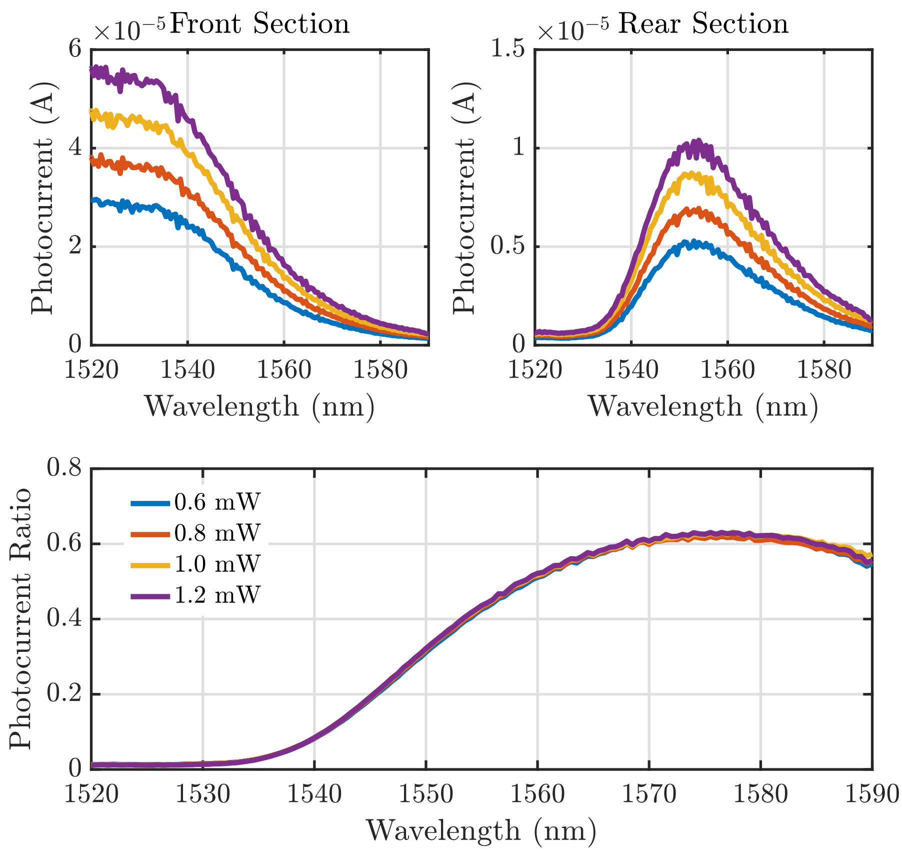

Figure 3.8: Readouts from the wavelength monitor as a function of input optical power

3.2.2.1 Wavelength monitoring of a 2-section Slotted Fabry-Pérot Laser

The wavelength-tuneable slotted Fabry-Perót laser described Chapter 2 and the wavelength monitor described in the section above were mounted on separate butterfly packages. The light was coupled between them using a single mode optical fibre (patch cord). The tuneable laser was placed on a mount with a thermo-electric cooler (TEC). As the wavelength of the laser is tuned using its drive currents, the photocurrents in the wavelength monitor are read out and fed into a LabVIEW™ program. This program then sets the temperature of the TEC mount underneath the laser accordingly, which fine-tunes and stabilises the lasing wavelength.

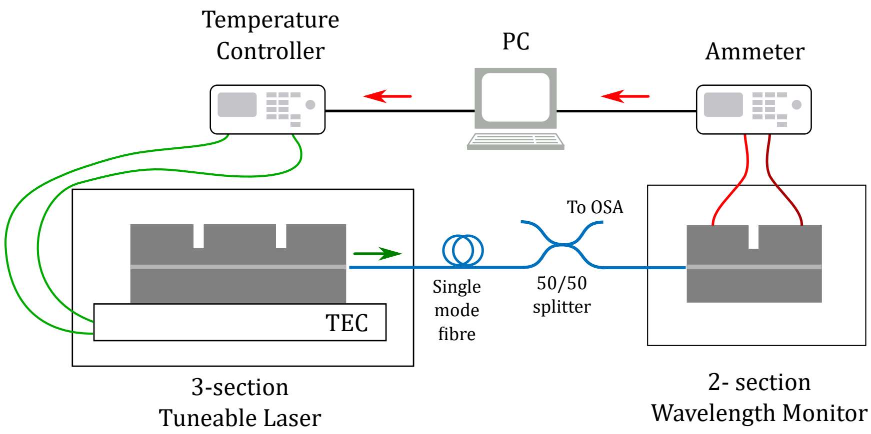

Figure 3.9: Schematic of the wavelength stabilisation setup

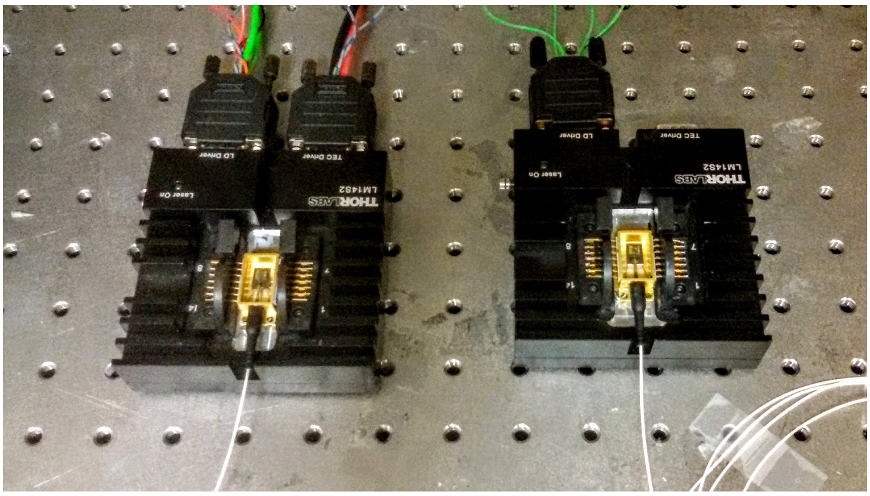

Figure 3.10: Photograph of a 3-section tuneable laser and a 2-section wavelength monitor mounted in separate butterfly packages

The schematic of this setup is shown in Figure 3.9, and the readout from the wavelength monitor is shown in Figure 3.11. The red curve is the value of the photocurrent ratio theoretically resulting from the setting of the wavelength of the tuneable laser. The laser was tuned between three diferent wavelengths λ_1, λ_2 and λ_3 which were 1546.18nm, 1546.3nm and 1546.58nm respectively. The black curve shows the measured value of the photocurrent ratio resulting from the stabilisation of the laser using a PID controller in the feedback loop. There is evident ringing in the photocurrent ratio, and thus the wavelength. The main reason for this is the slow response of the thermal feedback implementation resulting from a double PID loop: one in LabVIEW and one within the TEC which sets the temperature using its internal PID controller. In practice, it would be theoretically possible to optimise this using custom-made electronics for the feedback loop between heating and the photocurrent ratio, resulting in wavelength stabilisation times of around milliseconds. Additionally from the noise in the photocurrent ratio, it can be inferred that the wavelength can be stabilised with a precision of 0.12nm (ex: λ_1 and λ_2) or about 15 GHz, which can also be further improved by on-board integrated electronics.

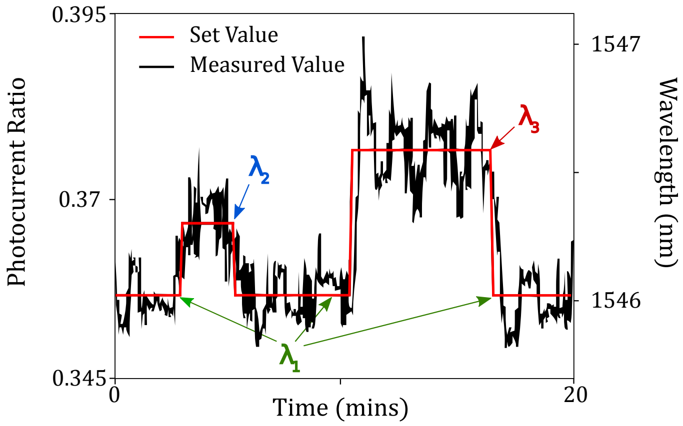

Figure 3.11: Photocurrent ratio from the wavelength monitor for three different wavelengths

Figure 3.12, shows screenshots from a LabVIEW™program where the wavelength of the 3-section tuneable slotted Fabry-Pérot laser is tuned between 1537nm and 1550nm. The instantaneous optical spectrum is shown in Figure 3.12(a), the wavelength sweep in (b) and the resultant photocurrent ratio in (c). It can be observed that although the wavelengths are linearly spaced, the corresponding photocurrent ratio is non-linear, as is to be expected. Additionally, it should be noted that the time axes on sub-figures (b) and (c) in Figure 3.12 are not identical since the plot was reset at a later time sub-figure (c) than in (b). Hence, the photocurrent ratio (c) only shows about 5 sweeps whereas the wavelength plot (b) shows about 40 sweeps.

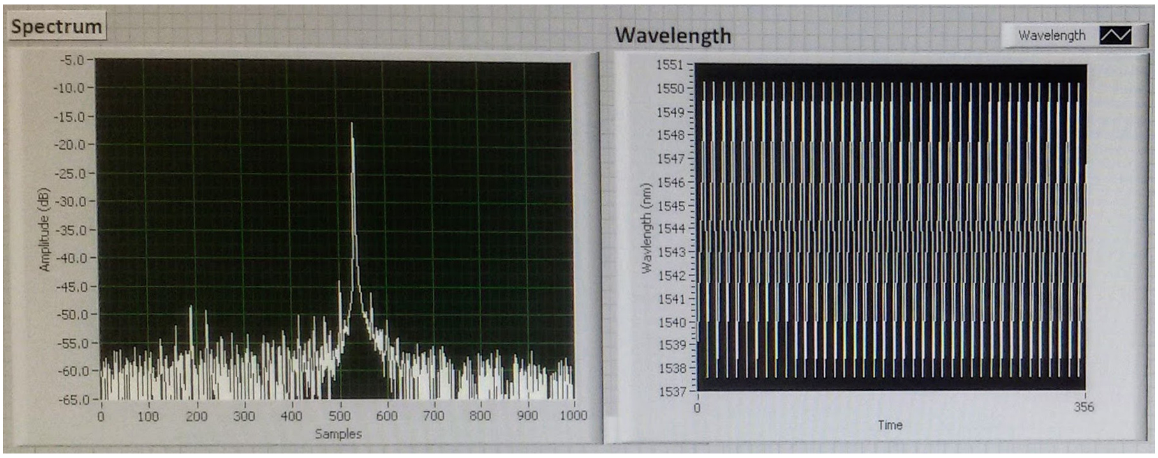

(a) (b)

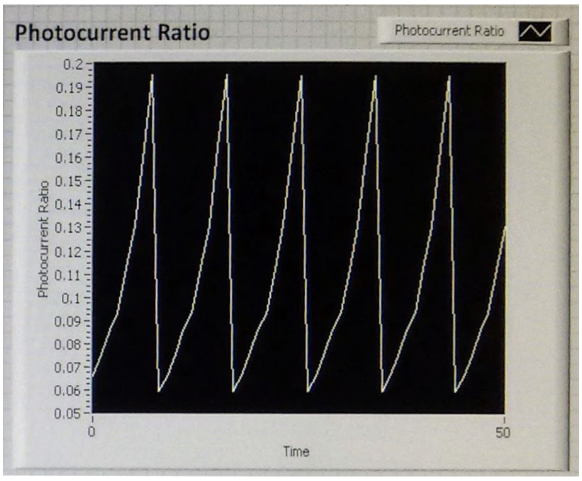

(c)

Figure 3.12: Screenshots from LabVIEW™ of (a) instantaneous optical spectrum (b) wavelength sweep and (c) resulting photocurrent ratio sweep

3.2.3 Polarisation Sensitivity

The measurements shown in the previous sections correspond to TE-polarised optical input with respect to the device. In this section we investigate the performance of the 2-section wavelength monitor for various states of the polarisation of the optical input.

3.2.3.1 Measurement Setup

In order to evaluate the effects of input polarisation on the wavelength monitoring, we need to first know the output polarisation characteristics of the tuneable laser source (TLS) used for the experiments. For this, we compare the direct output of the TLS on a photodetector (Newport® 818-IR Germanium-photodetector) with the output of the TLS passed through an in-line fibre polariser (ILP - Thorlabs® ILP1550PM). The ILP is designed to pass linearly polarised light while blocking the orthoganally polarised light from an randomly or unpolarised light source.

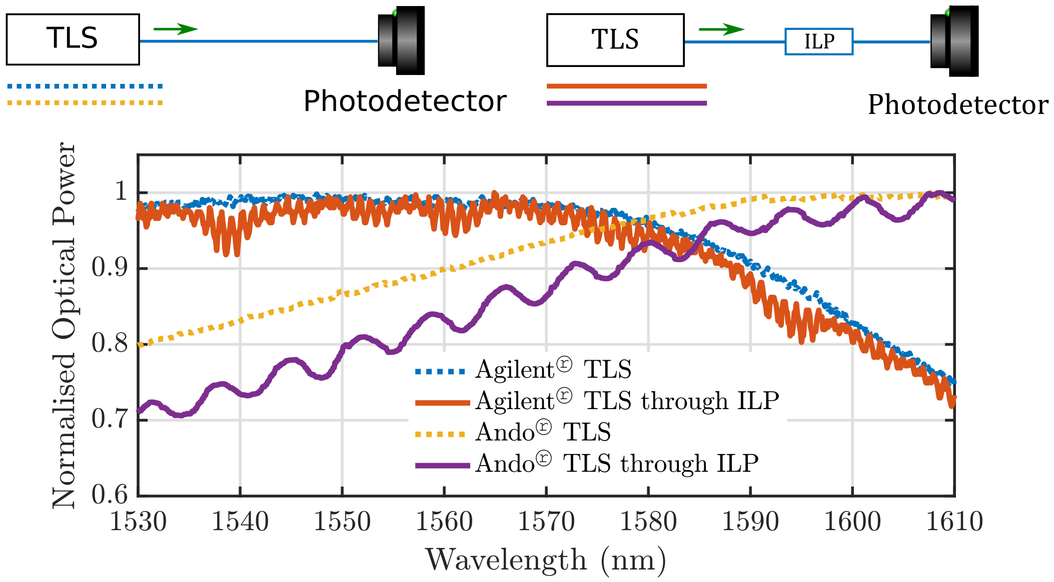

Figure 3.13: Polarisation wobble in two different tuneable laser sources

As shown in Figure 3.13, we see the output through the ILP is oscillating whereas the direct output from the TLS is not. This means that the output polarisation from the TLS has a wobble with a certain period with respect to wavelength which is converted into oscillations in power when passed through an ILP. This is further verified by repeating the experiment for TLS from two different vendors (Agilent® and Ando®). We observe similar power oscillations in both cases, but with different periods, indicating that polarisation wobble with respect to wavelengths is indeed present in both the tuneable laser sources, but because of differences in the internal workings, the period of this wobble is different.

To rule out the ILP causing the observed oscillations, we run the optical output of the Agilent® TLS through a different polariser (Thorlabs® PBC1550SM). This is shown in Figure 3.14, where we observe power oscillations from the output of the two different polarisers further confirming that the polarisation wobble arises from within the TLS.

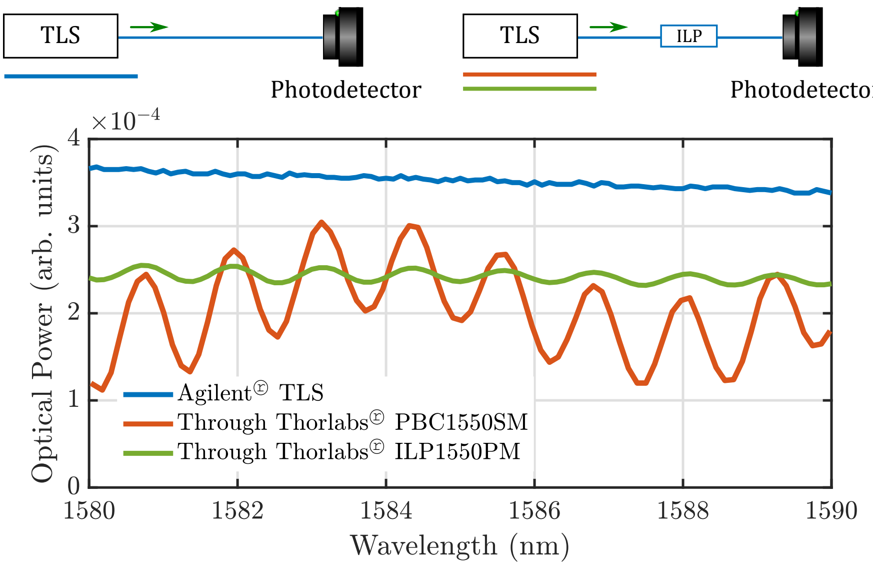

Figure 3.14: Polarisation wobble in the Agilent® TLS using two different polarisers

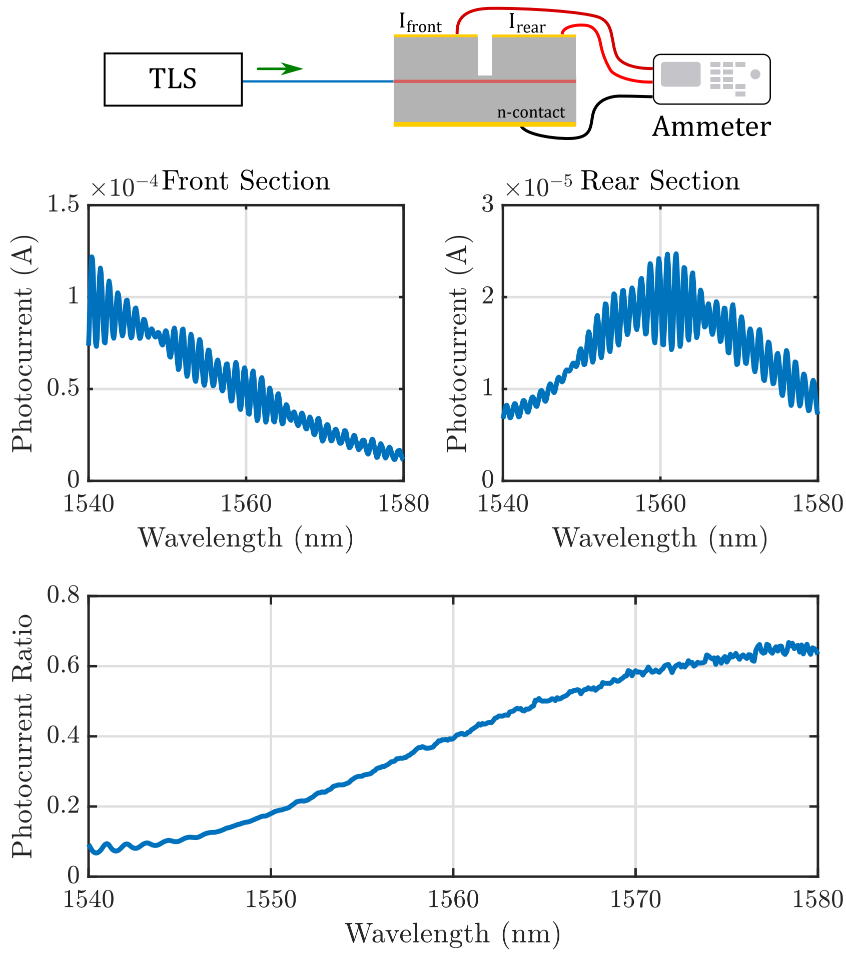

Figure 3.15: Photocurrents in the 2-section wavelength monitor directly coupled to the Agilent® TLS

When we couple the output of the Agilent® TLS directly to our 2-section wavelength monitor, we can see the oscillations picked up in the measured photocurrents, shown in Figure 3.15. The period of these oscillations are around 1.1nm, which is the same period as the oscillations observed when the output from the TLS was passed though a linear polariser. From this we can infer that this waveguide photodetection scheme is very sensitive to input polarisation in the individual sections' photocurrents. But, from Figure 3.15 we also see that the photocurrent ratio is not majorly affected by this polarisation sensitivity since the polarisation wobble from the TLS varies within possibly a narrow range.

3.2.3.2 Response to input polarisation

To understand the polarisaion sensitivity of our wavelength monitor better, we need to test it under the whole range of input polarisation states. In order to achieve this, we couple the output of the TLS to an in-line fibre polariser (ILP). At the end of the ILP, we now have linearly polarised light. It is important to keep in mind that although using the ILP has resulted in a theoretically pure linear polarisation, the polarisation-wobble from the TLS is now converted into a power fluctuation which is still present in this linearly-polarised output which can be seen in Figure 3.16. But as shown earlier (Figure 3.8), the photocurrent ratio is not very sensitive to power fluctuations.

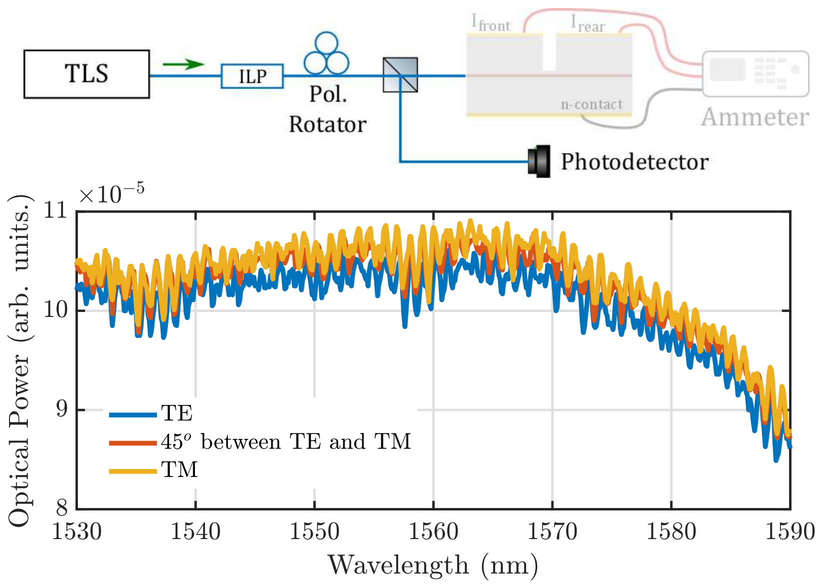

Figure 3.16: Power oscillations resulting from the polarisation-wobble in Agilent® TLS coupled to a commerical photodetector

We pass this linearly-polarised light through a polarisation rotator (half-wave plate). By rotating the half-wave plate though 45^o, we can rotate the polarisation vector of the linearly-polarised light by 90^o, i.e. all the way from TE to TM with respect to the wavelength monitor. This is shown in Figure 3.17 where we observe that the most ideal response is obtained for TE polarised light. As the polarisation state changes from TE towards TM, we observe that the photoresponse in the front section goes down uniformly for all wavelengths. On the other hand, in the rear section, the photoresponse goes down for longer wavelengths, but goes up for shorter wavelengths. An interesting feature to note is the crossover point around 1540nm where the photoresponse in the rear section is the same regardless of the state of polarisation of the input light. The investigation of this stationary point in Figure 3.17 is worthy of future work.

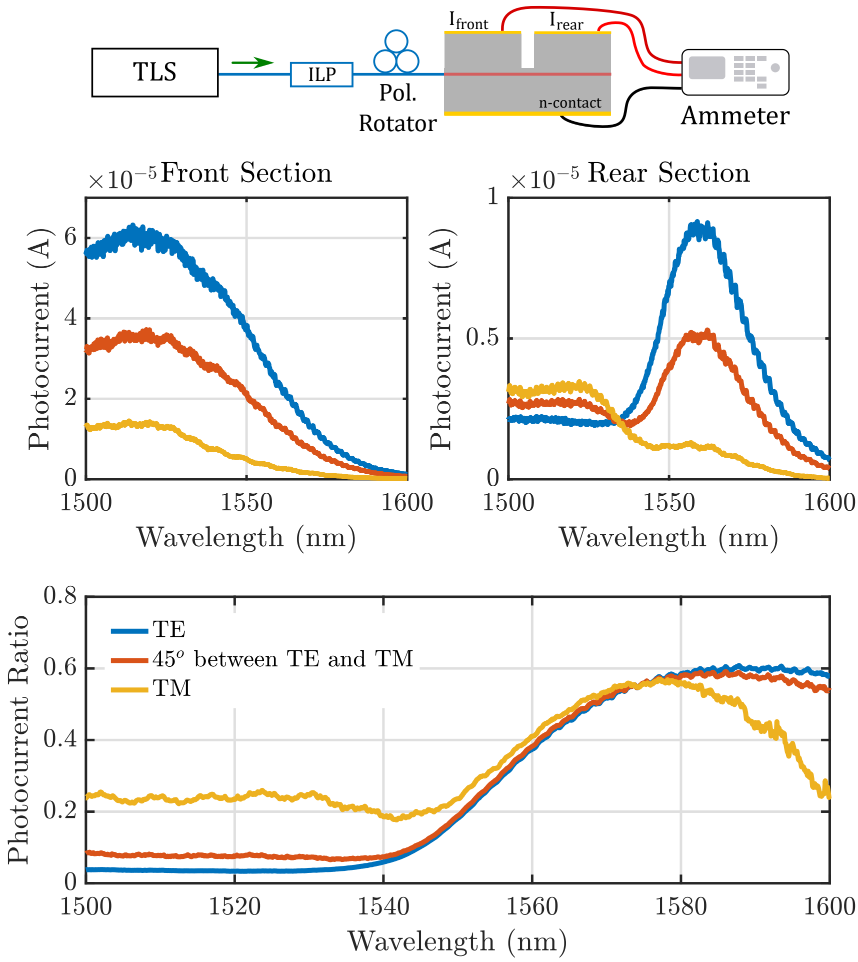

Figure 3.17: Photocurrents in the 2-section wavelength monitor coupled via an ILP and a polarisation rotator to the Agilent® TLS

3.3 Summary

A 2-section Fabry-Pérot-like device was described in this chapter that can output a parameter which is a measure of the wavelength of its input light. The theory behind its operation was presented along with a simulation of the expected photoresponse which matched experimental results. This device can be used as a wavelength monitor in applications which require sensing of the optical wavelength or frequency and furthermore in devices which require not only sensing but also stabilisation of wavelength. The latter has been demonstrated experimentally by using the wavelength monitor in a PID control loop to monitor and stablise the wavelength of a 3-section tuneable slotted Fabry-Pérot laser described (Chapter 2) and fabricated as part of this thesis work. The accuracy of stabilisation is within 15 GHz in frequency around a wavelength of 1550nm. The accuracy and time needed for stablisation can be improved greatly by using custom on-board electronics in place of laboratory equipment and automation software used to prove the concept in this thesis.

The wavelength range of operation and sensitivities achieved by this 2-section wavelength monitoring device makes it a suitable candidate for use in telecommunication applications. Since it has the same epitaxial layer structure and waveguide geometry as the slotted Fabry-Pérot laser in Chapter 2, it can be integrated easily into the same device without the need for any selective area bandgap engineering techniques. At this point in the thesis we have two components (tuneable laser and a wavelength monitor) needed towards building an optical transmitter for telecom applications. The process of integration of these two components and other necessary components like a modulator and related issues are further explored in the following chapters.

References

[1] "G.692: Optical interfaces for multichannel systems with optical amplifiers." `https://www.itu.int/rec/T-REC-G.692-199810-I/en`. (Accessed on 01-Sep-2019).

[2] H. Nasu, T. Takagi, T. Shinagawa, M. Oike, T. Nomura, and A. Kasukawa, "A highly stable and reliable wavelength monitor integrated laser module design," *Journal of Lightwave Technology*, vol. 22, pp. 1344–1351, May 2004.

[3] H. Nasu, T. Takagi, T. Shinagawa, M. Oike, T. Nomura, and A. Kasukawa, "A highly stable and reliable wavelength monitor integrated laser module design," *Journal of Lightwave Technology*, vol. 22, pp. 1344–1351, May 2004.

[4] Y. Park, S.-T. Lee, and C.-J. Chae, "A novel wavelength stabilization scheme using a fiber grating for WDM transmission," *IEEE Photonics Technology Letters*, vol. 10, pp. 1446–1448, Oct 1998.

[5] M. Imaki, S. Yamamoto, M. Sato, Y. Nishimura, K. Masuda, S. Takagi, A. Adachi, J. Yamashita, and Y. Hirano, "Wideband athermal wavelength monitor integrated wavelength temperature-tunable DFB-LD module," *Electronics Letters*, vol. 37, pp. 1035–1036, Aug 2001.

[6] B. Mason, S. P. DenBaars, and L. A. Coldren, "Tunable sampled-grating DBR lasers with integrated wavelength monitors," *IEEE Photonics Technology Letters*, vol. 10, pp. 1085–1087, Aug 1998.

[7] C. Sookdhis, T. Mei, and H. S. Djie, "Wavelength monitoring with low-contrast multimode interference waveguide," *IEEE Photonics Technology Letters*, vol. 17, pp. 822–824, April 2005.

[8] H. Li, S. Zhong, X. Yang, Y. J. Chen, and D. Stone, "Full coverage mul-

tichannel wavelength monitoring circuit using centre-offset phased-array waveguide grating," *Electronics Letters*, vol. 34, pp. 2149–2151, Oct 1998.

[9] "JDSU S4245." `http://www.acronymeo.com/jdc25gb4setu.html`. Accessed: 2018-02-23.

[10] "Finisar S7500." `https://www.digikey.com/products/en?FV=fffc0307,ffe0005f&k=tunable`. Accessed: 2018-02-23.

[11] X. Wu, P. E. Jessop, D. M. Bruce, B. J. Robinson, and D. A. Thompson, "Inline quantum-well waveguide photodetectors for the measurement of wavelength shifts," *Journal of Lightwave Technology*, vol. 15, pp. 2278–2283, Dec 1997.

[12] A. Alping, R. Tell, and S. Eng, "Photodetection properties of semiconductor laser diode detectors," *Journal of Lightwave Technology*, vol. 4, pp. 1662–1668, Nov 1986.

[13] A. S. Davydov, "Theory of Urbach's Rule," *physica status solidi (b)*, vol. 27, no. 1, pp. 51–56, 1968.

[14] Y. Varshni, "Temperature dependence of the energy gap in semiconductors," *Physica*, vol. 34, no. 1, pp. 149 – 154, 1967.

[15] I. Vurgaftman, J. R. Meyer, and L. R. Ram-Mohan, "Band parameters for III–V compound semiconductors and their alloys," *Journal of Applied Physics*, vol. 89, no. 11, pp. 5815–5875, 2001.

Chapter 4

Monolithic Integration

In the previous chapters two components, namely a tuneable laser based on a slotted Fabry-Pérot design and a 2-section wavelength monitor were presented and discussed as standalone devices. This chapter deals with the integration of these components onto the same substrate along with other components like an optical modulator and a semiconductor optical amplifier that are necessary in our pursuit of creating a complete low-cost optical transmitter module for telecommunication applications. In the first few sections, the theory behind the modulator design is presented, followed by experimental results from an integrated device. The chapter concludes with a section discussing the results obtained from an integrated wavelength monitor.

4.1 Electro-optic Effects in Semiconductors

In broad terms, the interaction between electrical and optical fields gives rise to electro-optic effects. Perhaps the most well-known electro-optic effect is the amplification of light by stimulated emission of radiation, which is the basis of lasers (in the presence of an optical resonator) and semiconductor optical amplifiers (SOAs, in the absence of an optical resonator). The next well-known electro-optic effect is the detection of light by photo-generation of carriers. This is typically done using a reverse-biased p-i-n junction where the incident light generated electrical carriers that are transmitted to an external circuit.

In this chapter, we will discuss the electro-optic effects used for modulation and switching where changes in properties like absorption and refractive indices in guided-wave devices are caused by an applied electric field. More specifically these kinds of electro-optic effects can further be classified into field effects and carrier effects. There are three main field-induced effects: the linear electro-optic effect (Pockels effect), the quadratic electro-optic effect (Kerr effect) and electro-absorption effects. On the other hand, refractive index changes can also be brought about by carrier injection or depletion [1]. This effect is widely used in silicon-based devices since the field-induced electro-optic effects are very weak in silicon [2]. In this work, since we work with InP based devices we will limit our discussion to field-induced effects.

Electro-optic effects manifest themselves in the propagation of guided waves by affecting the susceptibility of the material, χ. For an isotropic material, χ is real, but in general it is complex and can be written as

$$\chi = \chi' - j\chi'' \tag{4.1}$$

where χ' and χ'' are the real an imaginary components of the susceptibility respectively. For a lossless isotropic material $\chi' = n^2$ and $\chi'' = 0$, where n is the refractive index of the material. In the presence of an electro-optic effect, χ changes by a quantity $\Delta\chi$ given by

$$\Delta\chi = \Delta\chi' - j\Delta\chi'' \tag{4.2}$$

For plane waves affected by a change in susceptibility, we obtain [3] :

$$\begin{aligned} E(z,t) &= \left[E e^{j\omega t - j\omega\sqrt{\mu_0\epsilon_0 n^2}z}\right] e^{-j\omega\sqrt{\mu_0\epsilon_0}\frac{\Delta\chi'}{2n^2}z} e^{-\frac{\omega\sqrt{\mu_0\epsilon_0 n^2}\Delta\chi''}{2n^2}z} \\ I(z) &= \frac{2}{\sqrt{\mu_0/n^2\epsilon_0}}|E(z,t)|^2 \\ &\approx \left[\frac{2E^2}{\sqrt{\mu_0/n^2\epsilon_0}}\right] e^{-\frac{\omega\sqrt{\mu_0\epsilon_0 n^2}\Delta\chi''}{2n^2}z} \end{aligned} \tag{4.3}$$

where $E(z,t)$ is the electric field component of the plane wave and ω is the angular frequency. The attenuation coeffecient, α is given by:

$$\begin{aligned} \frac{dI}{dz} &= -\alpha I \\ \text{with } \alpha &= \frac{\omega\sqrt{\mu_0\epsilon_0}\Delta\chi''}{n} \end{aligned} \tag{4.4}$$

After propagating a distance z, we see from Equation 4.3 that the wave gets an additional phase shift of $\omega\sqrt{\mu_0\epsilon_0}\frac{\Delta\chi'}{2n}z$ and from Equation 4.4 that the intensity is attenuated by $e^{-\alpha}$ with $\alpha = \frac{\omega\sqrt{\mu_0\epsilon_0}\Delta\chi''}{n}$.

We observe that a change in the real part of the susceptibility $\Delta\chi'$ leads to a change in phase-shift due to a change in the refractive index, and the change in the imaginary part of the susceptibility $\Delta\chi''$ leads to a change in the absorption of the material.

Electro-optic effects that exploit the change $\Delta\chi'$ can be further divided into the linear electro-optic effect (or Pockels Effect) or the quadratic electro-optic effect (or Kerr Effect) depending on whether $\Delta\chi'$ is linearly or quadratically proportional to the applied electric field. Pockels effect is present only in crystals that lack inversion symmetry, whereas Kerr effect is present in all transparent materials [4] and in the presence of both Pockels and Kerr effects, Pockels effect tends to dominate. One of the designs for modulators that uses these *electro-refractive* effects is the Mach-Zehender modulator (MZM) where the light is split into two branches and a phase shift in one of the branches is controlled such that when the light recombines, it interferes either constructively or destructively leading to modulation of the signal.

On the other hand, electro-optic effects that exploit the change $\Delta\chi''$ are known as electro-absorption effects. In this work, the modulator design is based on this electro-absorption effect which is explained further in the following section.

4.2 Electro-Absorption Mechanisms

In semiconductors, the mechanism of absorption and emission of light happens via electrons and holes. At low temperatures and low carrier densities, the Coulomb interaction between electrons and holes leads to the formation of exciton pairs [5], which are held together by a binding energy E_b. For stimulated absorption to occur the following three conditions have to be met : an energy level in the conduction band must be empty; an energy level in the valence band must contain an electron; and the energy of the incident photon must exceed the bandgap energy minus the binding energy, i.e. $h\nu > E_g - E_b$. In bulk semiconductors this Coulomb interaction is experienced in three dimensions with the n^{th} bound state exciton energy given by:

$$\begin{aligned} E_b^{3D} &= -\frac{R_y}{n^2} \\ \text{where} \quad R_y &= \frac{m_r q^4}{2\hbar^2(4\pi\epsilon_s)^2} \end{aligned} \tag{4.5}$$

where R_y is the Rydberg enegry of the exciton [6], m_r is the reduced mass of the carriers and ϵ_s is the permittivity of the material.

4.2.1 Franz-Keldysh Effect

At room temperatures the thermal energy of the particles is much higher than the binding energy of the exciton in bulk semiconductors (Equation 4.5) and hence their exciton spectra can be observed only at low temperatures and thus can be neglected for this discussion. In the presence of an external electric field, it is possible for a photon to be absorbed whose energy is less than the bandgap energy. This phenomenon was first studied by Franz and Keldysh [7, 8] and is known as the *Franz-Keldysh effect*.

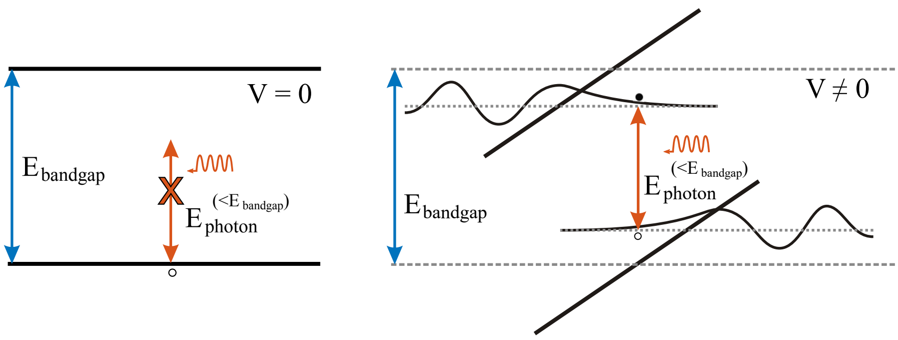

(a) (b)

Figure 4.1: Band diagrams under (a) zero applied electric field - absorption below bandgap energy not possible and (b) non-zero applied electric field exhibiting Franz-Keldysh effect

Figure 4.1 (b) shows the tilted band structure in a semiconductor with an applied electric field. The electron and hole wavefunctions now exhibit an Airy function-structure compared to plane waves under zero electric field.

The tails of the wavefunctions leak into the classically forbidden bandgap [9] and thus absorption coefficient is now more complex as shown in Figure 4.2. This change in absorption $\Delta\alpha$ with change in applied electric voltage ΔV is used in making electro-absorption modulators. Maximising the change in absorption for a given change in electric field $(\Delta\alpha/\Delta V)$ is desirable to achieve efficient modulators. In this regard the Franz-Keldysh effect in bulk semiconductors can be enhanced by using quantum well structures, as explained in the next section.

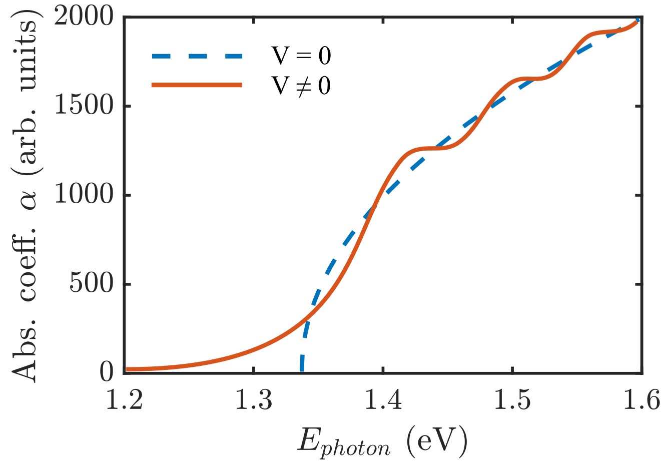

Figure 4.2: Franz-Keldysh in InP showing change in absorption with applied electric field[9]

4.2.2 Quantum-confined Stark Effect

Due to better confinement of electrons and holes compared to bulk semiconductors, quantum well structures exhibit different electro-absorption behaviour. Owing to the small dimensions, the Coulomb interaction between the electrons and holes is considerably higher than in bulk semiconductors (where we neglected it in the previous section for the discussion of the Franz-Keldysh effect), and is experienced in two dimensions instead of three due to the spatial confinement. In a 2-D case, the n^{th} bound state exciton energy given by:

$$E_b^{2D} = -\frac{R_y}{\left(n - \frac{1}{2}\right)^2} \tag{4.6}$$

For the $n = 1$ state we see that the binding energy in 2D (Equation 4.6) is four times that in 3D (Equation 4.5). This increased energy means that the exciton spectra are visible at room temperature and in the presence of applied electric field. Figure 4.3 (b) shows the tilting of the bands under an electric field. E_{cv} is the energy difference between E_{e1} (the lowest energy level for electrons in the conduction band) and E_{hh1} (the highest energy level for heavy holes in the valence band), and stimulated transition of heavy hole excitons take place just under $E_{e1} - E_{hh1}$. Under the tilting of the bands, the quantum mechanical solution for the energy levels leads to a reduction in E_{cv}, i.e. $E_{cv}(V) < E_{cv}(0)$ [3]. This means that light absorption happens at lower photon energies, or longer wavelengths. This effect is known as the *quantum confined Stark effect* or QCSE. Figure 4.4 shows the measured absorption spectra (using Bentham

PVE300 kit) from an InAsP/InGaP multiple quantum well structure for different electric fields where the red-shift in the exciton peak can be observed [10].

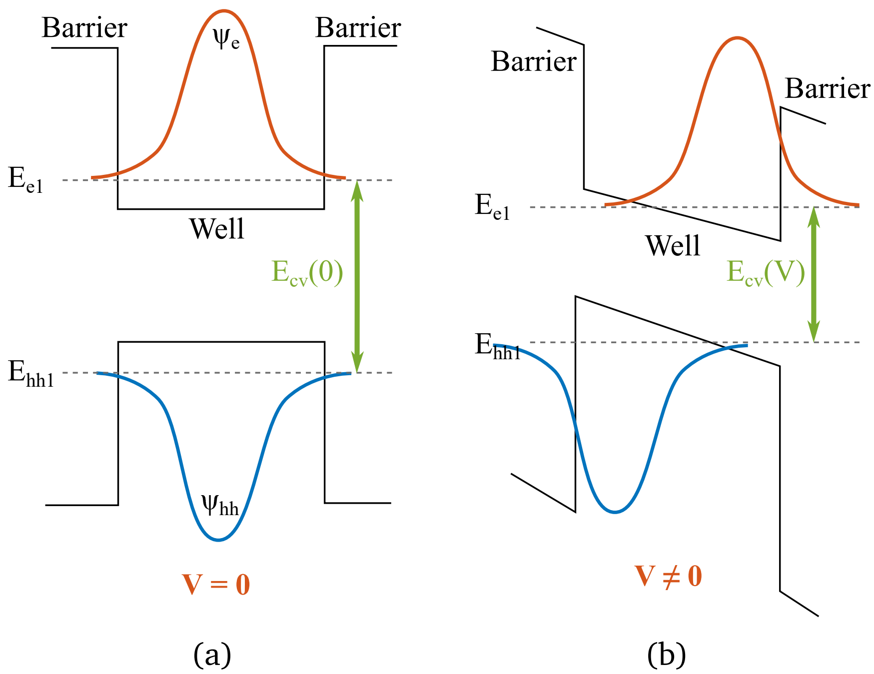

Figure 4.3: Band diagrams of a quantum well under (a) zero electric field and (b) non-zero electric field

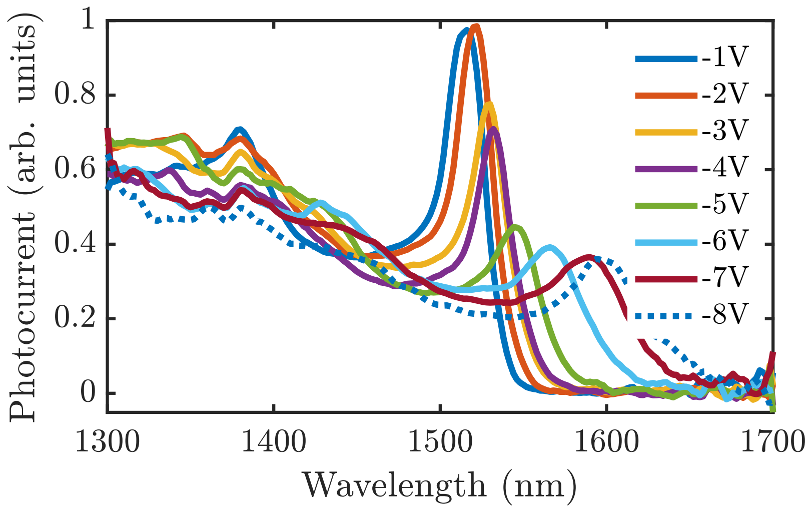

Figure 4.4: QCSE in InAsP/InGaP MQW structure showing change in absorption with applied electric field measured on an IQE 13-17 substrate (Appendix A)

As with the Franz-Keldysh case, this change in absorption $\Delta\alpha$ can be used in designing modulators but the $\Delta\alpha/\Delta V$ is larger for MQW structures using QCSE compared to bulk semiconductors using the Franz-Keldysh effect (FKE). A few reasons for using the FKE (and thus bulk semiconductors) over QCSE are that for QCSE can be obtained when the applied electric field is perpendicular in direction to the quantum wells, whereas for FKE it can be any direction, and the fact that absorption in QW structures is easier to saturate compared to bulk materials because of the band edge discontinuity between the well and the barrier some photo-generated carriers are retained and not completely carried away by the bias voltage [3]. In the context of this thesis work, these disadvantages of QCSE are not relevant for the following reasons: the lasers are made using a waveguide geometry on a p-i-n structure and are already based on MQW structures parallel to the surface of the material, the electric field in such a case is perpendicular to the quantum wells and the optical power from the laser does not get to the high-power region that causes saturation in QW absorption. Thus, QCSE is an ideal candidate to be exploited in making an integrated modulator for such lasers.

4.3 Design and Fabrication

4.3.1 Angled Facets

For a laser it is beneficial to have maximum reflectivity at the facet for increasing the feedback to achieve higher lasing power and efficiency. But for other waveguide devices such as an SOA or a modulator, a higher reflectivity at the facet is detrimental to their performance. This is because, in the context of these devices, we would like to avoid the formation of a resonant cavity and rather have the optical field make a single pass through them. One of the ways to control the reflectivity at the facet is by changing its angle with respect to the waveguide [11].

The reflectivity of a facet as a function of its angle with respect to the waveguide can be calculated using the method described in [12]. The loss due to the difference in refractive index of the two materials can be computed using the Fresnel coefficients. Setting this aside for now, we can look at the loss due to the tilted facet. The phase mismatch between the guided reflected wave and the transmitted wave is the reason for the optical loss. If these were perfectly aligned (as in the case for non-angled facets), the transmission coefficient would be unity. This phase factor can be written as $e^{i(2\theta)\beta x}$, where x is the transverse direction and β is the propagation constant of the guided TE mode. The transmission coefficient's amplitude can now be written as [13]

$$c = \frac{\beta}{2\omega\mu_0 P_0} \int_{-\infty}^{\infty} |E_y|^2 \, e^{i(2\theta)\beta x} dx \tag{4.7}$$

where E_y is the y-component of the electric field of the fundamental TE mode, ω is the angular frequency of light, μ_0 is the magnetic permeability of vacuum and P_0 is the optical power of the fundamental TE mode. Combining Equation 4.7 with the Fresnel coefficient of a reflected plane wave between the two materials $R_f(\theta)$, we can write the final loss from the angled facet, $R(\theta)$, as:

$$R(\theta) = R_f(\theta) \, |c|^2 \tag{4.8}$$

The Fresnel reflection coefficient for TE light with an angle of incidence θ and angle of transmission θ_t between two materials of refractive indices n_1 and n_2 is given by:

$$R_f(\theta, \theta_t) = \left| \frac{n_1 \cos\theta - n_2 \cos\theta_t}{n_1 \cos\theta + n_2 \cos\theta_t} \right|^2 \tag{4.9}$$

Using Snell's Law :

$$n_1 \sin\theta = n_2 \sin\theta_t \tag{4.10}$$

equation 4.9 can be re-written as:

$$R_f(\theta) = \left| \frac{n_1 \cos\theta - n_2 \sqrt{1 - \left(\frac{n_1}{n_2} \sin\theta\right)^2}}{n_1 \cos\theta + n_2 \sqrt{1 - \left(\frac{n_1}{n_2} \sin\theta\right)^2}} \right|^2 \tag{4.11}$$

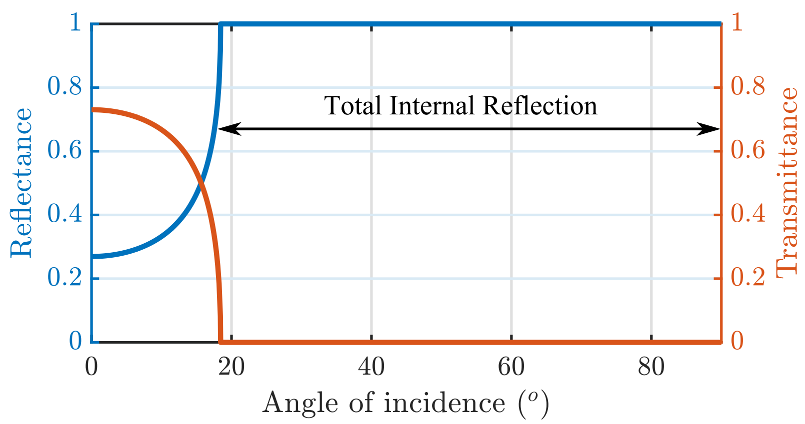

Figure 4.5: Fresnel reflectance and transmittance at an interface between InP and air

The reflectance obtained from Equation 4.11 along with the corresponding transmittance is plotted in Figure 4.5. Using the expressions for the fundamental TE mode [14], Equation 4.8 can be written as:

$$R(\theta) = R_f(\theta) \left[\frac{WU^2 \left\{ \left(W^2 - \left(\frac{\beta\theta d}{2}\right)^2 \right) \dfrac{\sin(\beta\theta d)}{\beta\theta d} + W\cos(\beta\theta d) \right\}}{(1+W)\left[U^2 - \left(\frac{\beta\theta d}{2}\right)^2\right]\left[W^2 + \left(\frac{\beta\theta d}{2}\right)^2\right]} \right]^2 \tag{4.12}$$

U, W and k are the normalized transverse propagation constant and the normalized transverse decay parameter and the wavenumber in free space respectively, given by:

$$\begin{aligned} U &= \frac{d}{2}\sqrt{n_1^2 k^2 - \beta^2} \\ W &= \frac{d}{2}\sqrt{\beta^2 - n_2^2 k^2} \\ k &= \frac{2\pi}{\lambda} \end{aligned} \tag{4.13}$$

where n_1 and n_2 are the effective refractive indices of the core and the cladding respectively, λ is the wavelength and d is the width of the core region.

Using the values for effective refractive indices and geometrical parameters from the previous chapters (Figure 2.8) and combining equations 4.11 and 4.12 we can plot the reflection from an angled facet as a function of the tilt angle as shown in Figure 4.6.

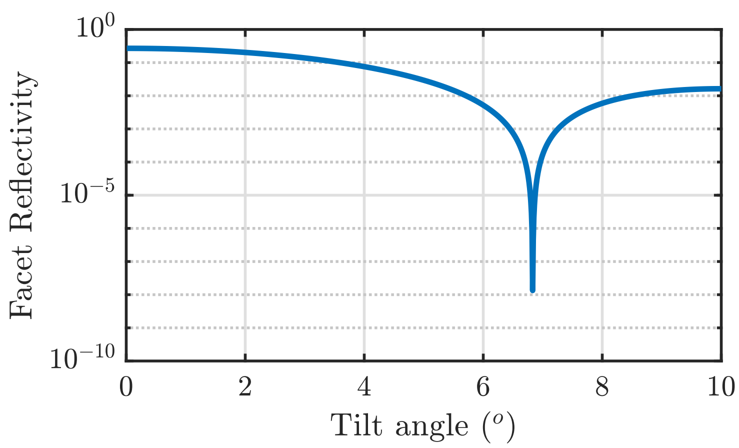

Figure 4.6: Reflection from an angled facet

We observe that there is a dip in the reflectance at an angle of around 7^o. We exploit this minimum in the reflectance curve for the devices in this thesis making the angle of their etched facets to be 7^o tilted with respect to the waveguide. Not only does the 7^o angle help at the output facets [15], but they also enhance performance between the laser and the modulator sections by reducing the optical crosstalk between them thus improving wavelength stability. This is discussed in further detail in the next chapter.

4.4 Experimental results

The 3-section slotted Fabry-Pérot laser described in section 2.4.2 was integrated on the same device along with the 2-section wavelength monitor from section 3.2, a modulator section and an booster SOA section using the fabrication steps described in Section 2.3.2 and in Appendix B. An etched facet separation was used on either side of the laser separating it from the wavelength monitor at the rear and the modulator section at the front. The main design targets for the modulator and SOA sections were set as part of the DISCUS project [16] which partly funded this thesis work. The long-reach passive optical network configuration (LR-PON) as proposed in the DISCUS project called for a modulator speed of 10 Gb/s and optical power of about 0 dBm in the fibre. Experimental results from these individual components contained within the integrated devices are presented in detail in the following sub-sections.

4.4.1 Integrated Modulator

The modulator in the integrated device is a Fabry-Pérot ridge waveguide section of length 80μm adjacent to the 3-section tuneable laser as seen in the microscope image in Figure 4.7. It can be driven electrically via a GSG contact. Two windows are opened in the 'Etched Facet' fabrication step (Appendix B) providing a deep etch in order to achieve the ground contact with the n-substrate.

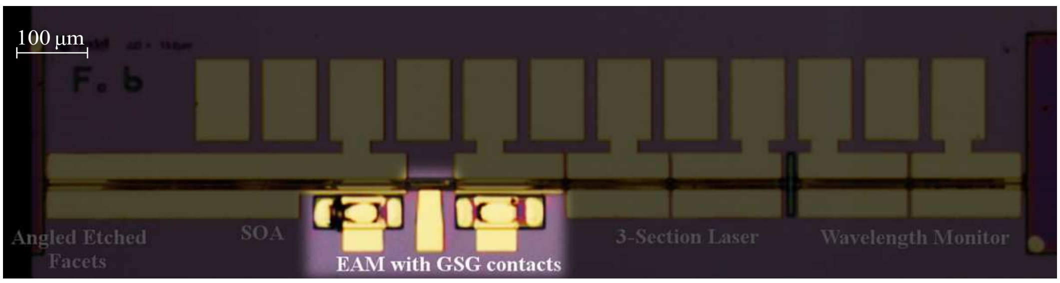

Figure 4.7: Microscope picture of an integrated transmitter device highlighting the modulator section

This section acts as an absorber when reverse-biased that attenuates light coming from the laser. Thus, the modulating action is achieved by switching the electrical drive from high reverse bias ('off' state or '0') to low reverse bias ('on' state or '1'). Two versions of this integrated device were fabricated with different kinds of separation between the laser and the modulator section - one with an angled slot (Figure 4.8 (a)) and another with an deep etch (Figure 4.8 (b)). The angled slot is similar to the slots in the slotted Fabry-Pérot laser and is defined in the lithography step for the ridge waveguide. The deep etch separation is an etch that is about 5μm deep and is defined as in the lithography step for an 'etched facet'.

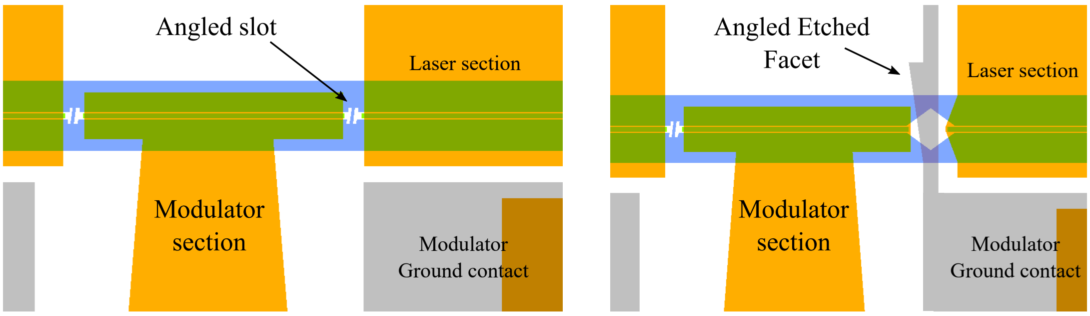

(a) (b)

Figure 4.8: Schematic of a modulator separated from the laser section by an (a) angled slot and (b) angled etched facet

From experimental results it is observed that under DC bias both of these designs show stable wavelength operation. When the modulator is driven with a 3 Gb/s pseudo random bit sequence (PRBS), the device with the angled slot separation loses its single-modedness. This can be attributed to insufficient optical isolation between the laser and the modulator sections. These measurements are shown in Figure 4.9. The angled deep etch separation is, thus, necessary for wavelength-stable operation of the integrated device. From a device with a deep etch separation, stable operation was observed for many channels, only one of which has been shown in the lower half of Figure 4.9 for illustative purposes. Furthermore, we observe that power attenuation caused by the operation of the modulator section (extinction ratio) is around 10 dB across the difference wavelength channels of the tuneable laser. A more in-depth small signal frequency response, S_{21} measurement on this integrated device was carried out in collaboration with the Photonics Systems Group at Tyndall National Institute - in particular with Daniel Carey *et al* [17]. The S_{21} measurements from four different wavelength channels is shown in Figure 4.10.

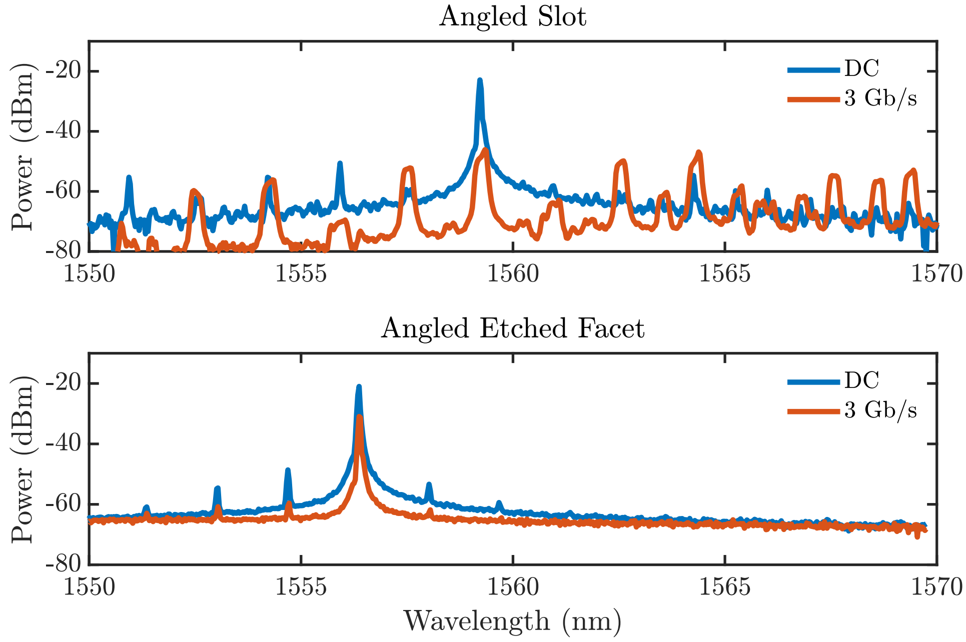

Figure 4.9: Optical spectra measured under fixed DC bias of modulator and a 3 Gb/s PRBS signal

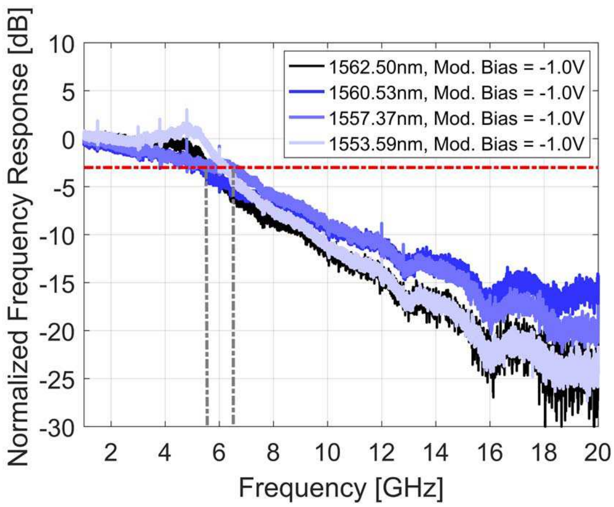

Figure 4.10: Normalized small-signal frequency response of the integrated transmitter for four arbitrarily chosen lasing modes[17]

It can be observed that the 3dB bandwidth of the modulator section ranges between 5.5 and 6.5 GHz for different wavelength channels of the laser, which is sufficient for operation at 10 Gb/s as demonstrated by a clean eye-diagram measurement which was carried out entirely within the scope of this thesis - Figure 4.11. The operation bandwidth and thus speed can be improved even further by using high-k dielectrics such as BeznoCycloButene (BCB) underneath the contact pads to reduce the capacitance of the device [18].

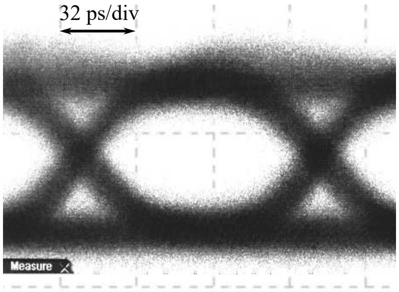

Figure 4.11: Eye diagram at 10 Gb/s using a PRBS signal on the integrated device with a 1V peak-to-peak driving voltage

4.4.2 Integrated SOA

Integrated semiconductor optical amplifiers (SOAs) are routinely used in photonic devices to amplify optical power from the laser source [19, 20]. In our case, the SOA might be especially useful in obtaining a constant optical power output from the transmitter since the laser yields produces varying output powers for different wavelength channels. Additionally, an SOA booster section can also be used to compensate for ageing effects of the laser and to shut off the transmitter during the process of network reconfigurations [20]. The SOA section can also provide a gating function which is necessary for burst-mode operation used frequently in Passive Optical Networks (PONs) [21].

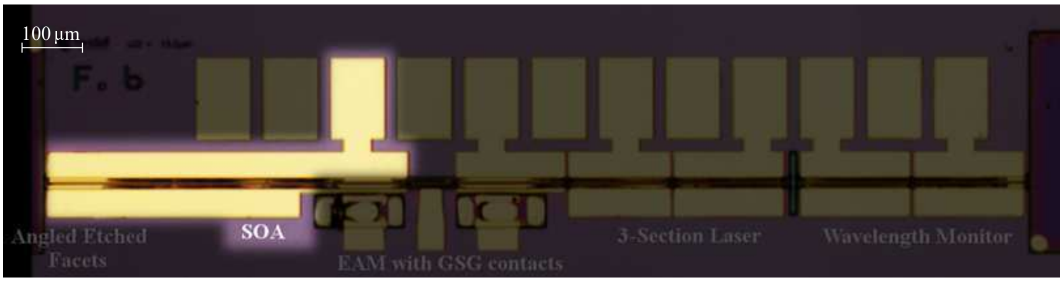

Figure 4.12: Microscope picture of an integrated transmitter device highlighting the SOA

In our design we use a 675μm-long SOA section which is forward biased. An angled slot separation is used between the modulator and the SOA. The output facet of the SOA is an angled etched facet angled at 7^o to reduce unwanted reflections. The SOA is a simple, long ridge waveguide that shares the same active layers as the laser and the modulator sections.

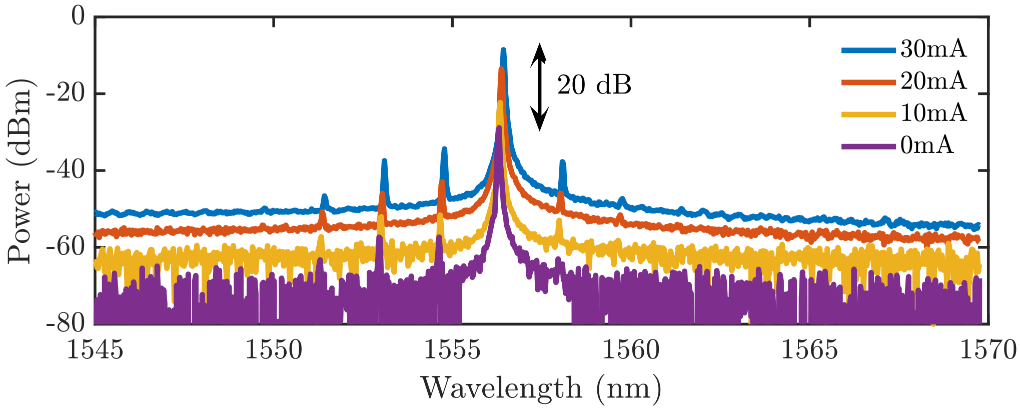

Figure 4.13: Output optical power of the laser showing the effect of the SOA booster

Figure 4.13 shows the optical spectra from the integrated device when the laser currents are fixed to obtain a particular wavelength channel, and the SOA current is swept between 0 and 30mA. We observe that this results in a 20dB change in peak output power. It should be noted that process of boosting the output power results in a wavelength shift of about 0.1nm for an SOA current of 30mA, which is most likely a thermal effect. This can be compensated by adjusting the temperature of the device in the package using a thermo-electric cooler (TEC) as is routinely done in commercial devices.

4.4.3 Integrated Wavelength Monitor

A suitable and highly convenient design for a monolithically integrable wavelength monitor was discussed in Chapter 3. However it was presented as a standalone device with the input light being coupled to it using a lensed from an external laser source which was either a commercially available tuneable laser or a 3-section slotted Fabry-Pérot device from this thesis. In this section, we discuss the same wavelength monitor design but integrated with the 3-section laser presented in Section 2.4.2. Figure 4.14 (a) shows a microscope image of a 3-section FP laser (left) integrated with a 2-section wavelength monitor (right) separated by a trench which is defined using the fabrication steps for an etched facet. This trench is zoomed in and shown in Figure 4.14 (b). The 7^o angle described in the previous section can be seen here.

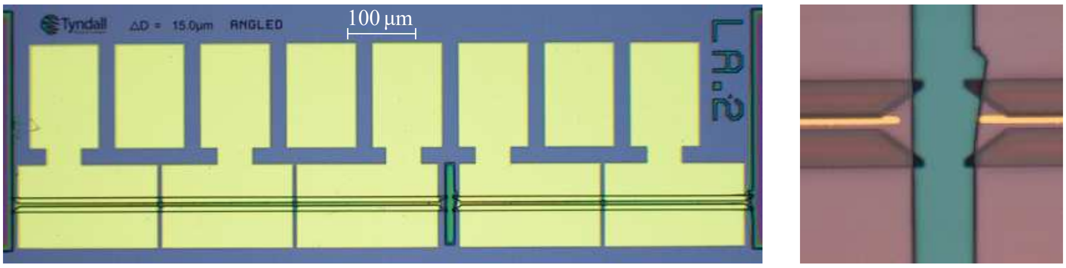

(a) (b)

Figure 4.14: Microscope image of (a) an integrated 3-section laser and 2-section wavelength monitor and (b) trench separating the laser and the wavelength monitor

The main objective of the trench is to provide electrical isolation between the laser and the wavelength monitor sections. At the same time, light from the laser also needs to be coupled into the wavelength monitor to enable its function in determining the wavelength. A wider trench results in better electrical and thermal isolation, but in poorer optical coupling. Thus, there is a trade-off between these effects. In order to determine an appropriate width for the trench, an experiment was carried out using devices fabricated with a multi-section tuneable laser separated from a single section Fabry-Pérot laser by a trench of varying widths as shown in Figure 4.15.

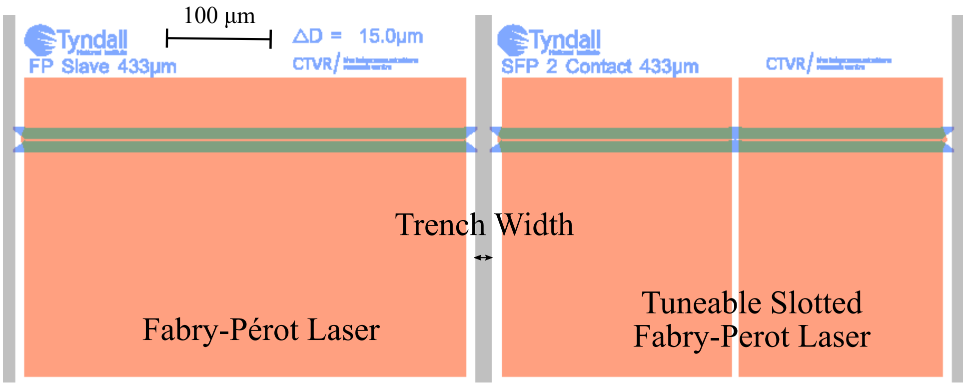

Figure 4.15: Schematic of the devices used in the experiment to determine ideal trench width

The Fabry-Pérot laser was injected with current and the output power from the facet was measured using an Newport™ 818-SL photodetector. Simultaneously, the nearest section of the tuneable laser on the other side of the trench was biased at 0V and the resulting photocurrent was measured. Figure 4.16 shows these two photocurrents plotted against each other.

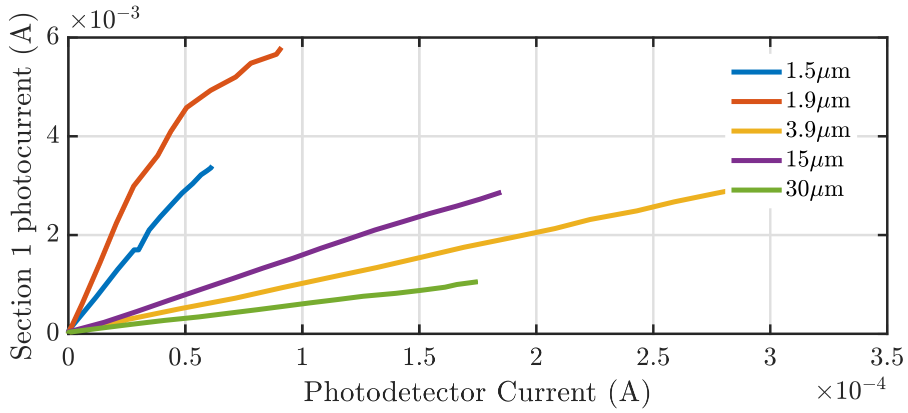

Figure 4.16: Photocurrent observed in the near section of the tuneable laser as a function of optical output power of the FP laser

We observe that although the narrower trenches yield in higher light coupling, the photoresponse has better linearity for widths greater than about 2μm. Additionally, an experiment was carried out where the 2-section SFP laser was maintained at a constant bias and the resulting single-moded lasing spectrum was recorded. Then the spectrum of the FP laser biased above threshold was recorded with the SFP laser turned off. Finally, both were turned on and the spectrum was recorded. The results are plotted in Figures 4.17 and 4.18 for devices with varying trench widths.

As expected, the 2-section SFP laser produces a spectrum with a higher SMSR that is referred to as *single-moded* in this discussion. The FP laser produces a standard Fabry-Pérot spectrum with multiple modes of similar power. The spectra for the SFP laser was measured at the right facet and that for the FP laser was measured at the left facet of the device from Figure 4.15. For trench widths of 1.5μm and 3.9μm, when both the SFP and FP lasers are switched on, the resulting spectrum is completely different from either of the SFP and FP laser spectra working alone as seen in Figures 4.17(a) and (b). This indicates a strong optical feedback between the two devices on either side of the deep trench.

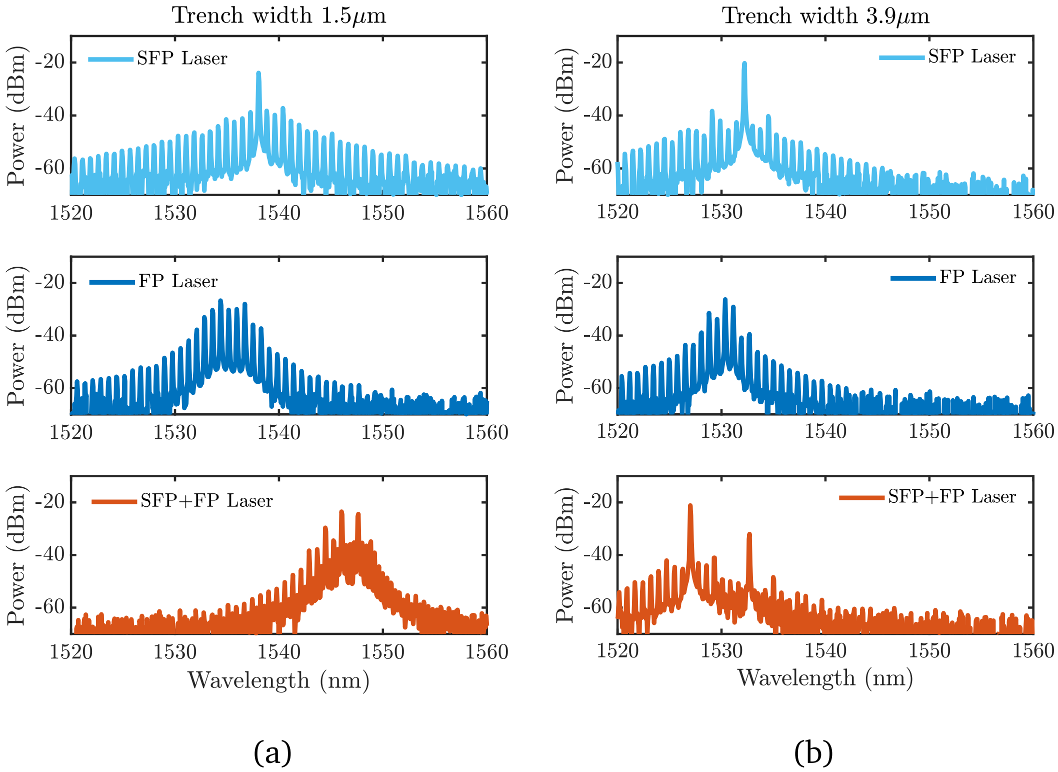

Figure 4.17: Spectra resulting from the SFP laser alone, FP laser alone and from both SFP and FP laser biased together for a trench width of (a) 1.5μm (b) 3.9μm

On the other hand, for a trench width of 30μm, the resultant spectrum of both the SFP and FP lasers operating together is identical to the FP laser working alone as seen in Figure 4.18(b). In this case, the trench seems to be too wide and the light from the SFP laser is completely lost and not coupled into the waveguide of the FP laser. However for a trench that is 15μm wide, in the combined spectra of the SFP and FP laser, we observe the single-mode spectrum from the SFP laser on top of the spectrum from the FP laser as seen in Figure 4.18(a). This indicates that 15μm is probably a good trade-off between being too narrow and too wide for a deep trench between the two sections.

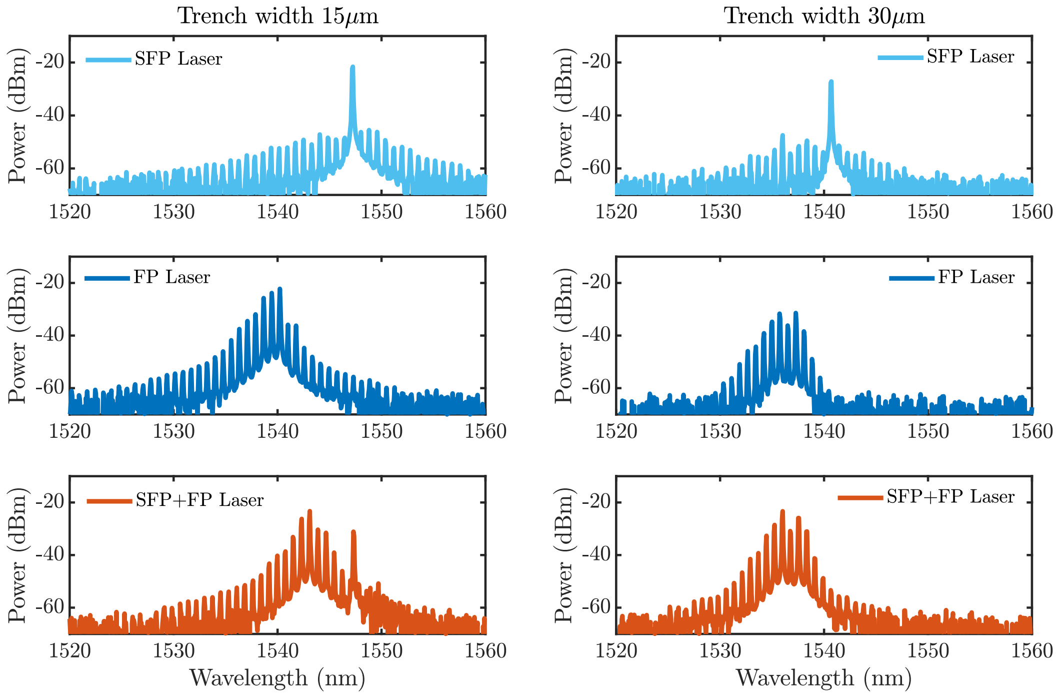

(a) (b)

Figure 4.18: Spectra resulting from the SFP laser alone, FP laser alone and from both SFP and FP laser biased together for a trench width of (a) 15μm and (b) 30μm

In summary, following from the results and discussion above, we choose 15μm as the width of the trench between the laser and the wavelength monitor as it produces good signal linearity while unlikely to produce optical feedback.

Coming back to the device which integrates the 3-section slotted Fabry-Pérot laser and the 2-section wavelength monitor together (Figure 4.14 (a)), measurements were carried out where the three tuning currents of the laser were swept between 0 and 40mA in steps of 2mA, while also reading the photocurrents generated in the two sections of the wavelength monitor of the same device just behind the laser. The front facet of the laser was fibre coupled into an optical spectrum analyser and the peak wavelength and the SMSR were measured. Plotting the photocurrent ratio versus the peak wavelength we obtain the curve in Figure 4.19(a). The corresponding curve from a standalone device is shown as an overlay for comparison.

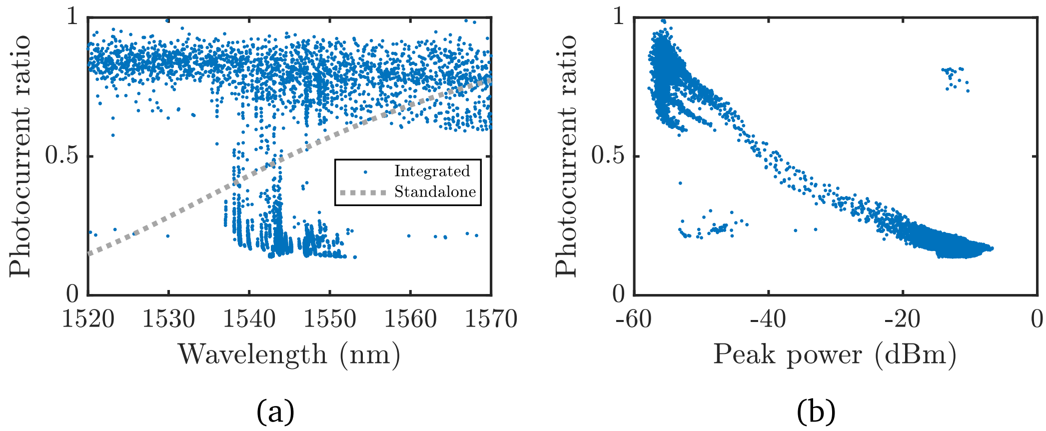

Figure 4.19: Photocurrent ratio as a function of the (b) laser wavelength and (b) peak power for an integrated laser-cum-wavelength monitor on IQE substrate

Figure 4.19 contains 9261 points, i.e. one point each in the 3-dimensional sweep of three laser section currents - 0 to 40 mA in steps of 2 mA - $21\times21\times21$ (=9261). This means that the plots contains points both below and above lasing threshold. It appears that the photocurrent ratio in the wavelength monitor has a value of closer to 1 when the laser is below threshold and a value closer to 0 when the laser is above threshold - irrespective of what the wavelength is. This is further verified when we plot the photocurrent ratio as a function of the peak optical power in Figure 4.19(b). We observe a clear correlation between increase in peak power and decrease in the photocurrent ratio. This strongly indicates the presence of unwanted optical crosstalk between the laser and the wavelength monitor. This is discussed in further detail in the following chapter.

The results described above are based on device fabricated on commercially available laser material from IQE. To investigate if there is an optical path between the laser and the wavelength monitor via the substrate, another epitaxial material was tested. This structure, called A1779 from now, has a very similar layer stack as the IQE material but with the additional of a 1μm thick layer of InGaAs below the active MQW region (refer Appendix A). This layer was intended as a sacrificial layer for in the micro-transfer-print process[22]. In our case this layer could be used as an absorbing layer which might get rid of unwanted optical paths through the substrate between the various sections on our integrated device.

The same device as shown in Figure 4.14(a) was fabricated on A1779 wafer using the same fabrication process as was used on an IQE wafer. The photocurrent ratio versus laser wavelength for this device is shown in Figure 4.20(a)

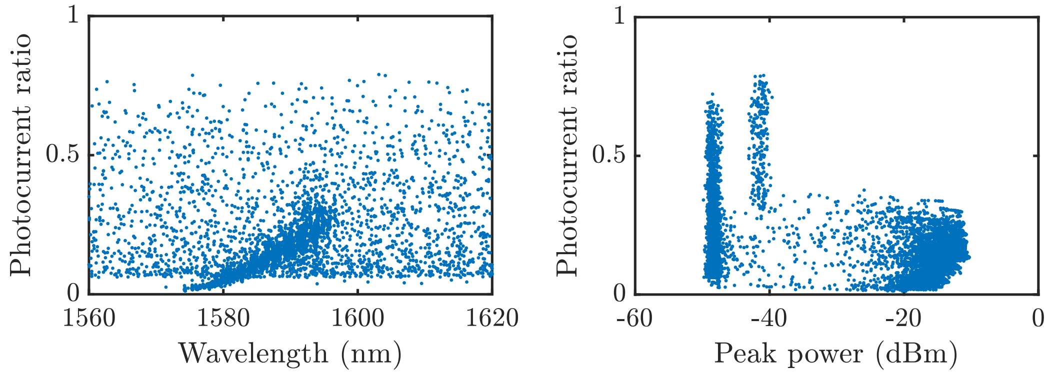

(a) (b)

Figure 4.20: Photocurrent ratio as a function of the (b) laser wavelength and (b) peak power for an integrated laser-cum-wavelength monitor on A1779 substrate

In this case, we observe that indeed there seems to be a pattern emerging in the photocurrent ratio versus wavelength plot. And the peak power does not seem to be as much correlated to the photocurrent ratio as in the previous case on an IQE substrate as can be seen from Figure 4.20(b). The absolute value of the Person Correlation Coefficient between the ratio and the peak power is 0.44 compared to 0.97 for the integrated device on IQE substrate. (a value of 0 implies completely uncorrelated and a value of 1 implies fully correlated).

Figure 4.20(a) contains both all points from the laser current sweep irrespective of whether the laser is below or above threshold and also whether it is single-moded or not. Filtering this plot to include only above threshold points that have SMSR of at least 20dB, we obtain Figure 4.21. Also shown in the same figure is a measurement made on a standalone wavelength monitor device on A1779 substrate with external injection from a commercially available tuneable laser source. It is evident from this plot that the integrated device on A1779 substrate works much better than that on the IQE substrate without the InGaAs absorbing layer beneath the MQW layers.

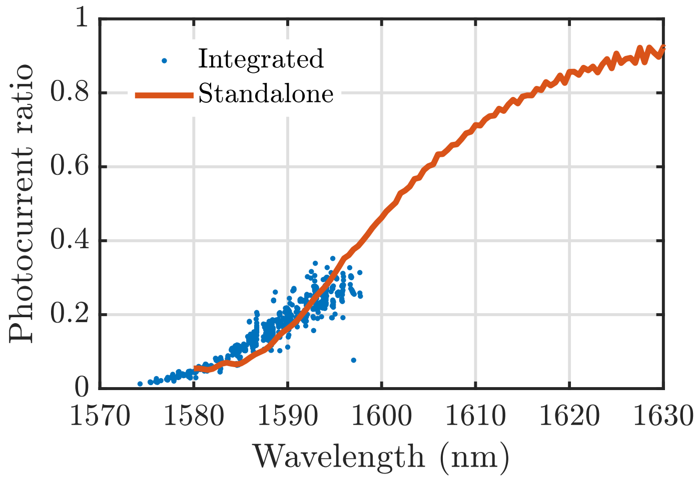

Figure 4.21: Photocurrent ratio as a function of the laser wavelength (SMSR>20dB) for an integrated laser-cum-wavelength monitor on A1779 substrate

4.5 Summary

Continuing from the previous chapters where standalone versions of a tuneable laser and a wavelength monitor were presented, this chapter presented an integrated device that contains the 3-section slotted Fabry-Pérot laser from Chapter 1, the 2-section wavelength monitor from Chapter 2, a modulator and an SOA booster integrated on to the same device. The modulator showed an extinction ratio of about 8-10dB, 3dB-bandwidth in the small-signal frequency response of about 6GHz and a clean eye diagram up to speeds of at least 10 Gb/s for a peak-to-peak drive voltage of 1V. It was shown that an angled deep etch separation was needed for wavelength-stable operation of the modulator. The SOA booster section was shown to be able to provide an optical gain/attenuation range of 20dB for a drive current range of 30mA.

Finally, results from the integrated wavelength monitor showed that on an IQE wafer, the device suffered from possibly heavy optical crosstalk between the laser and the wavelength monitor sections. A proposed solution would be to use an absorbing layer underneath the active MQW layer to get rid of parasitic reflections resulting from possible light leaking into the substrate at the location of the deep etches. In the next chapter, this optical crosstalk along with electrical and thermal crosstalks are discussed in more detail leading to a more robust design of the integrated optical transmitter.

References

[1] R. Soref and B. Bennett, "Electrooptical effects in silicon," *IEEE journal of quantum electronics*, vol. 23, no. 1, pp. 123–129, 1987.

[2] L. Liu, J. V. Campenhout, G. Roelkens, R. A. Soref, D. V. Thourhout, P. Rojo-Romeo, P. Regreny, C. Seassal, J.-M. Fédéli, and R. Baets, "Carrier-injection-based electro-optic modulator on silicon-on-insulator with a heterogeneously integrated III-V microdisk cavity," *Opt. Lett.*, vol. 33, pp. 2518–2520, Nov 2008.

[3] W. S. C. Chang, *Fundamentals of Guided-Wave Optoelectronic Devices*. New York, NY, USA: Cambridge University Press, 1st ed., 2009.

[4] A. Chen and E. J. Murphy, *Broadband optical modulators : science, technology, and applications*. Boca Raton, FL : CRC Press, 2012. Includes bibliographical references and index.

[5] I. Merkulov and V. Perel', "Effects of electron-hole interaction on electro absorption in semiconductors," *Physics Letters A*, vol. 45, no. 2, pp. 83 – 84, 1973.

[6] S. Chuang, *Physics of Optoelectronic Devices*. Wiley Series in Pure and Applied Optics, Wiley, 1995.

[7] W. Franz, "Einfluß eines elektrischen Feldes auf eine optische Absorptionskante," *Zeitschrift Naturforschung Teil A*, vol. 13, pp. 484–489, June 1958.

[8] L. V. Keldysh, "Behavior of Non-metallic Crystals in Strong Electric Fields," *Soviet Journal of Experimental and Theoretical Physics*, vol. 6, p. 763, 1958.

[9] A. S. Davydov, "Theory of Urbach's Rule," *physica status solidi (b)*, vol. 27, no. 1, pp. 51–56, 1968.

[10] *RF Photonic Technology in Optical Fiber Links*. Cambridge University Press, 2002.

[11] P. A. Besse, J. S. Gu, and H. Melchior, "Reflectivity minimization of semiconductor laser amplifiers with coated and angled facets considering two-dimensional beam profiles," *IEEE Journal of Quantum Electronics*, vol. 27, pp. 1830–1836, Jun 1991.

[12] D. Marcuse, "Reflection loss of laser mode from tilted end mirror," *Journal of Lightwave Technology*, vol. 7, pp. 336–339, Feb 1989.

[13] L. Kurbatov, S. Shakhidzhanov, L. Bystrova, K. VV, and K. SI, "Investigation of superluminescence emitted by a gallium arsenide diode," *Soviet Physics Semiconductors-USSR*, vol. 4, no. 11, pp. 1739–+, 1971.

[14] D. Marcuse, *Light transmission optics*. Van Nostrand Reinhold New York, 1972.

[15] R. Lemos Alvares Dos Santos, D. D'Agostino, H. Rabbani Haghighi, M. Smit, and X. Leijtens, "Fabrication and characterization of etched facets in InP for advanced packaging of Photonic Integrated circuits," in *Proceedings of the 19th Annual Symposium of the IEEE Photonics Benelux Chapter, 2-4 November 2014, Enschede, The Netherlands* (S. Garcia Blanco, K. Boller, M. Sefunc, and D. Geuzebroek, eds.), pp. 107–110, University of Twente, 2014.

[16] M. Ruffini, N. Doran, M. Achouche, N. Parsons, T. Pfeiffer, X. Yin, H. Rohde, M. Schiano, P. Ossieur, B. O'Sullivan, R. Wessäly, L. Wosinska, J. Montalvo, and D. B. Payne, "Discus: End-to-end network design for ubiquitous high speed broadband services," in *2013 15th International Conference on Transparent Optical Networks (ICTON)*, pp. 1–5, June 2013.

[17] D. Carey, P. Ramaswamy, G. Talli, C. Antony, B. Roycroft, B. Corbett, and P. D. Townsend, "Characterization of a Low-Cost, Monolithically Integrated, Tunable 10G Transmitter for Wavelength Agile PONs," *IEEE Journal of Quantum Electronics*, vol. 54, pp. 1–12, Dec 2018.

[18] Y. Cheng, J. Pan, Y. Wang, F. Zhou, B. Wang, L. Zhao, H. Zhu, and W. Wang, "40-Gb/s Low Chirp Electroabsorption Modulator Integrated With DFB Laser," *IEEE Photonics Technology Letters*, vol. 21, pp. 356–358, March 2009.

[19] A. J. Ward, D. J. Robbins, G. Busico, E. Barton, L. Ponnampalam, J. P. Duck, N. D. Whitbread, P. J. Williams, D. C. J. Reid, A. C. Carter, and M. J. Wale, "Widely tunable DS-DBR laser with monolithically integrated

SOA: design and performance," *IEEE Journal of Selected Topics in Quantum Electronics*, vol. 11, pp. 149–156, Jan 2005.

[20] D. M. Adams, C. Gamache, R. Finlay, M. Cyr, K. M. Burt, J. Evans, E. Jamroz, S. Wallace, I. Woods, L. Doran, P. Ayliffe, D. Goodchild, and C. Rogers, "Module-packaged tunable laser and wavelength locker delivering 40 mW of fibre-coupled power on 34 channels," *Electronics Letters*, vol. 37, pp. 691–693, May 2001.

[21] K. Taguchi, K. Asaka, S. Kimura, K. Suzuki, and A. Otaka, "Reverse bias voltage controlled burst-mode booster SOA in λ-tunable ONU transmitter for high-split-number TWDM-PON," *IEEE/OSA Journal of Optical Communications and Networking*, vol. 10, pp. 431–439, April 2018.

[22] R. Loi, J. O'Callaghan, B. Roycroft, C. Robert, A. Fecioru, A. J. Trindade, A. Gocalinska, E. Pelucchi, C. A. Bower, and B. Corbett, "Transfer Printing of AlGaInAs/InP Etched Facet Lasers to Si Substrates," *IEEE Photonics Journal*, vol. 8, pp. 1–10, Dec 2016.

Chapter 5

Crosstalk Evaluation

The advent of Erbium-doped fibre amplifiers (EDFAs) and arrayed waveguide gratings (AWGs) [1] gave rise to a rapid growth in the deployment of networks employing wavelength division multiplexing (WDM) techniques [2]. This in turn led to increasing complexity in photonic integrated circuits (PICs) starting from a few components [3] to more than 400 integrated components on a single chip [4, 5]. In order to reduce cost, it is preferable to pack as many components as possible in a fixed area of a semiconductor chip. However, active devices start to interact with each other undesirably as the distance between them reduces. This interaction is commonly referred to as crosstalk.

The major contributors to crosstalk are electrical leakages, caused due to low-impedance shunting paths within the chip, thermal crosstalk resulting from the heat generated due to the driving currents, and optical crosstalk due to light coupling between adjacent waveguides or through the substrate. This chapter describes the observation, calculation and measurement techniques for the various modes of crosstalk between the laser and wavelength monitor.

To illustrate the ramifications of crosstalk within the device, figure 5.1 compares the responses of a standalone wavelength monitor and an integrated device incorporating a tuneable laser and a wavelength monitor. In figure 5.1 (a), the light injected from an external tuneable laser (Agilent 81600B) using a lensed fibre into the 2-section standalone wavelength monitor. The wavelength is varied in steps of 0.01nm and the photocurrents are measured. On the other hand, in figure 5.1 (b), both the laser and the wavelength monitor are on the same chip. The tuning currents of the 3-section laser are varied in steps of 2mA which results in discrete wavelength tuning. For each of these tuning currents, the peak wavelength of the single mode spectrum is measured using an OSA (Ando AQ-6315A @ 0.05nm resolution) and the photocurrents generated in the two sections of the wavelength monitor are measured.

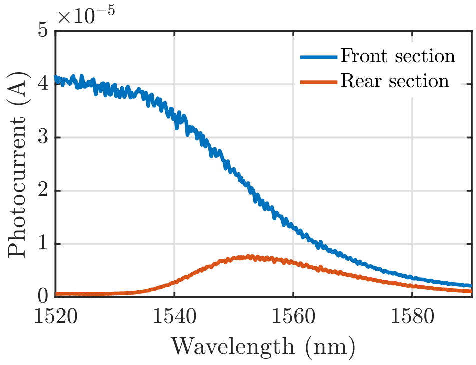

(a)

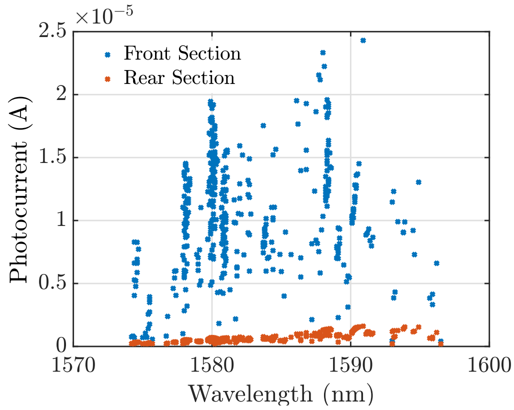

(b)

Figure 5.1: Comparison of (a) standalone and (b) integrated wavelength monitor photocurrents as a function of wavelength

We can see that, for many wavelengths, there are more than one value of photocurrent readout. This is due to the fact that different tuning currents produce the same optical wavelength (albeit with different power and SMSR). This shows that varying the drive currents of the laser, keeping the wavelength constant, affects the photocurrents in the wavelength monitor. This could be due to the drive currents leaking into the wavelength monitor's photocurrents, or higher driver currents producing heat which is conducted to the wavelength monitor causing its readouts to shift, or different drive currents producing different optical power levels which could couple through the substrate to the wavelength monitor in different strengths, or a combination of all the above crosstalk effects.

In the following sections, we try to measure and analyse each of the possible causes separately and discuss solutions to mitigate the effects of such crosstalk.

5.1 Electrical Crosstalk

The separation between the laser and the integrated wavelength monitor in this first generation device consisted of a deep (5 μm) etch with a length of 100 μm as shown in Figure 5.2. This etch goes through the active region well into the substrate.

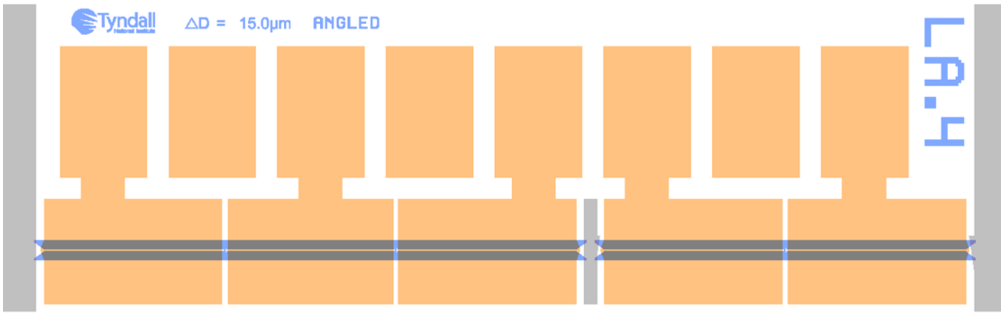

Figure 5.2: Schematic of a first generation device showing the isolation between laser and wavelength monitor sections

This means that for the drive currents of the laser to leak into the wavelength monitor sections, one or more of the following scenarios must exist. The dieletric isolation underneath the metallic contact pads could be conducting. Or the diode structure of the device might have a large leakage current in reverse bias. It is also possible that the current could be leaking through the p-doped layer above the intrinsic layer, or that the etching process for the deep facet between the laser and wavelength monitor sections could leave a conducting residue on the sidewalls.

The hypothesis of the conducting-dielectric was easily ruled out by conforming that probing two different points on the dielectric directly or two different dummy metallic contact pads (which were not connected to any active part of the device) yielded an open circuit. Figure 5.3 shows the reverse bias leakage currents for the diode structures. The reverse bias current around 1V to 2V is not sufficient to cause crosstalk issues with the measured photocurrents in the wavelength monitor sections, since it is much lower than the generated photocurrents.

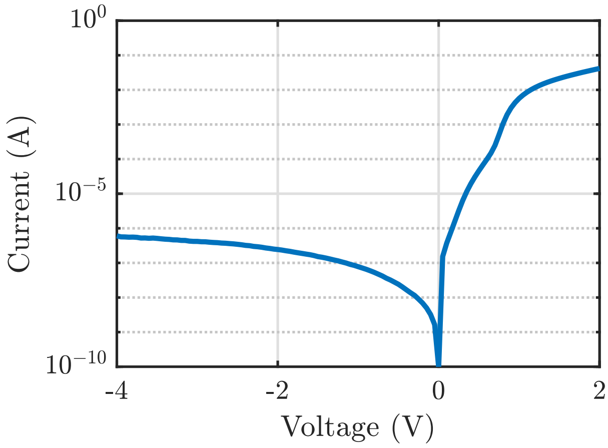

Figure 5.3: I-V characteristics of the laser diode structure

The next possible pathway of the leakage of the currents could be through the p-doped layer on top of the intrinsic layer of the diode. To test this, two test devices (Figure 5.4) with similar geometry to the integrated device were considered. When two adjacent devices were probed on the same side of the deep isolation etch (Fig. 5.4 (a)), the measured resistance was a few kilo-Ohms. On the other hand, when two devices were measured on either side of the deep isolation etch (with no possible pathway through the p-doped layer), the resistance was found to be in the order of mega-Ohms. This proves that the deep etch is indeed isolating and there is no unwanted conducting residue left over from the etching process.

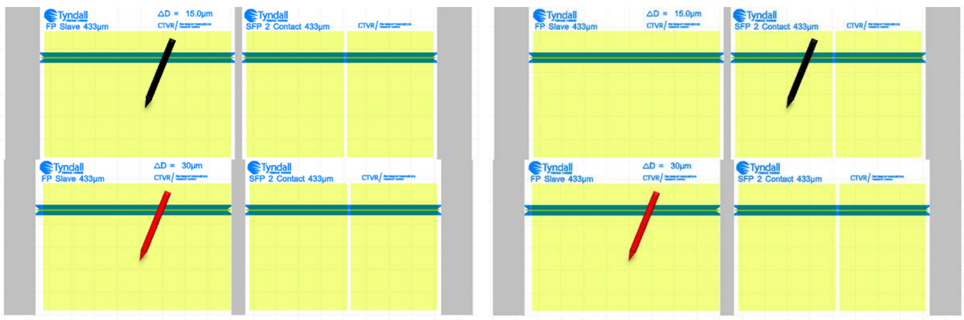

(a) (b)

Figure 5.4: Devices with a continuous deep isolation etch between the two sections of the device

Furthermore, p to p resistance measurements were carried out on adjacent devices in cleaved bars (Figure 5.5 (a)) of simple Fabry-Pérot lasers. There were no isolation etches between these devices. The p-p resistance as a function of separation is plotted in Figure 5.5 (b). We can see that the slopes of the resistance curves are consistent with the widths of the cleaved bars. Assuming the resistivity of the p (Zn) doped InP layer to be 2 x 10^{-5} Ω cm, we can calculate the thickness of the conducting layer to be 50nm, which is consistent with the processed device structure.

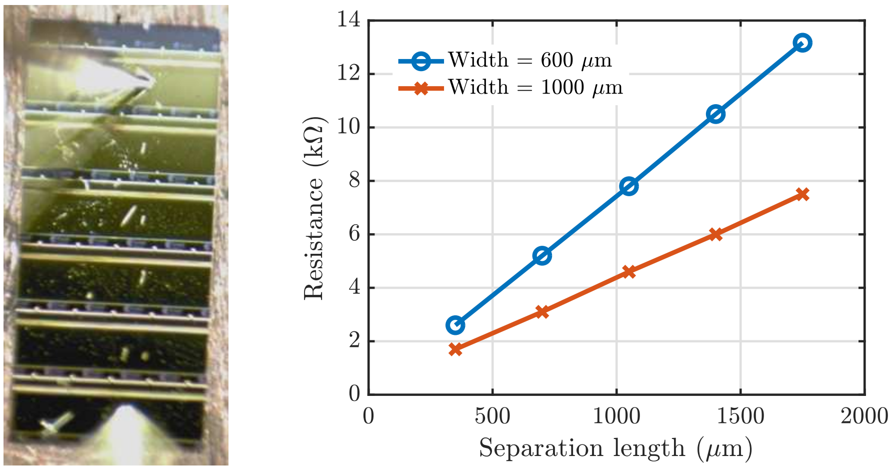

(a) (b)

Figure 5.5: (a) Microscope image of a cleaved bar of Fabry-Pérot lasers (b) Resistance vs Separation length of adjacent devices in two different cleaved bars

From the above discussion, we can infer that the leakage in the integrated devices (Figure 5.2) is indeed through the p-doped layer as illustrated in Figure 5.6.

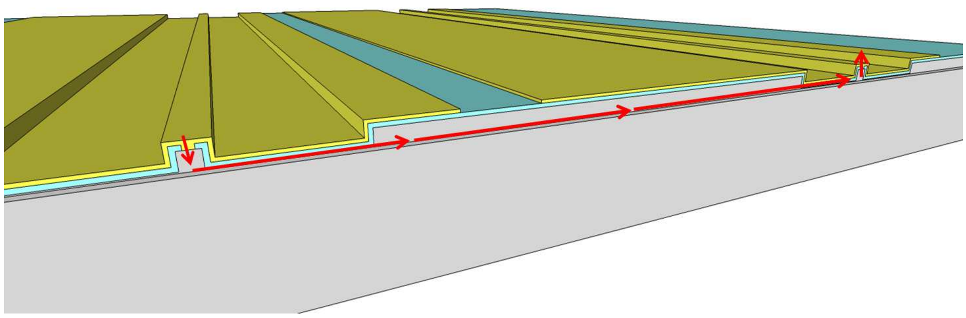

Figure 5.6: Illustration of the eletrical leakage path along the p-doped layer

The solution to overcome this leakage would be to isolate the whole device by having a deep etched trench not only on a limited area between laser and the wavelength, but to etch out the complete length, thus allowing no possible pathway through the p-doped layer. This is shown in the mask design for the second iteration in Figure 5.7.

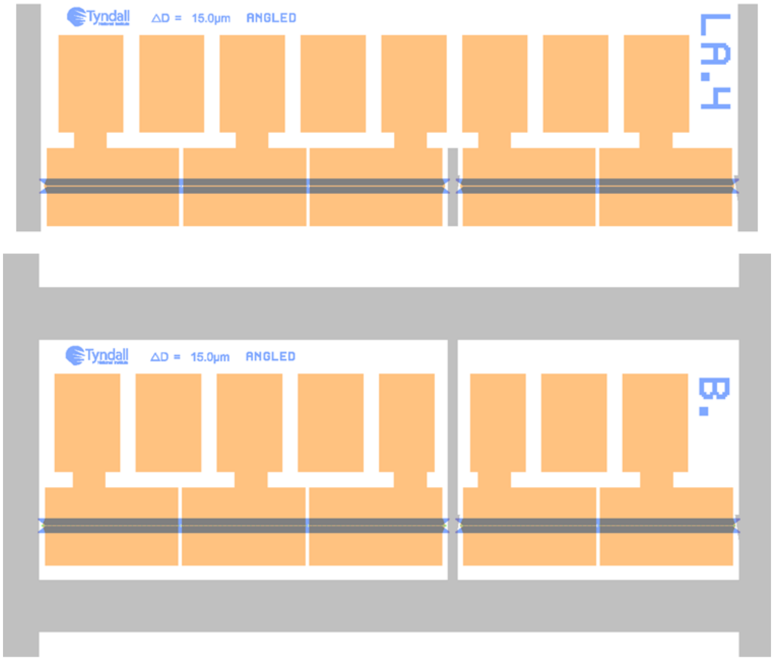

Figure 5.7: Design change to isolate electrical crosstalk between laser and wavelength monitor sections

The p-to-p resistance between the rear laser section and the front wavelength monitor section changed from a few kΩ's in the previous design to about 10MΩ in the new design with the deep trench all around the device. This addresses the electrical crosstalk between the laser and wavelength monitor effectively.

5.2 Thermal Crosstalk

To test thermal effects within the chip, measurements were performed on a device with the laser operating at fixed wavelength. The optical spectrum was measured using an OSA for different temperatures by controlling the thermo-electric cooler (TEC) attached to the chuck where the device was placed. The results are plotted in Figure 5.8(a). The shift in the peak wavelength as a function of temperature is extracted from Figure 5.8(b) to be 0.1nm/^{o}C.

We can now use this value of wavelength shift vs temperature to indirectly infer the temperature at various locations on the chip. This is shown in Figure 5.9 where a device's peak wavelength (and thus temperature) is monitored for various electrical injected powers in neighbouring devices. The separation between the devices is 500 μm.

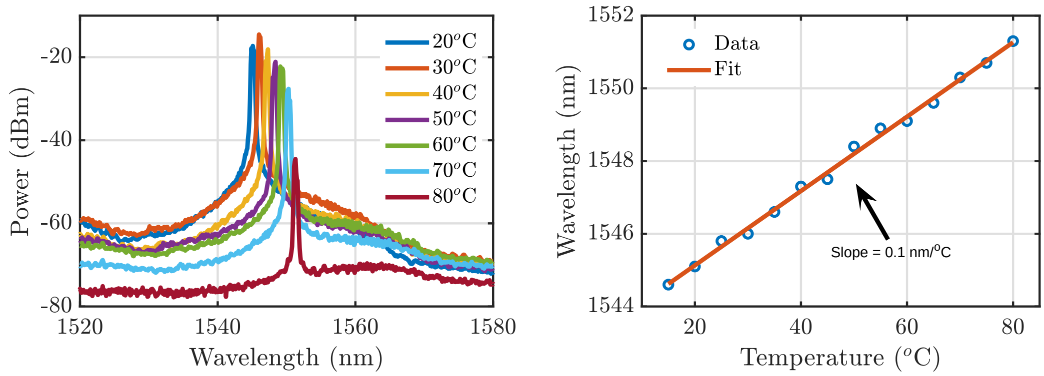

(a) (b)

Figure 5.8: (a) Optical spectrum of a single-mode channel from the laser at different temperatures (b) Fit of peak wavelength shift vs temperature

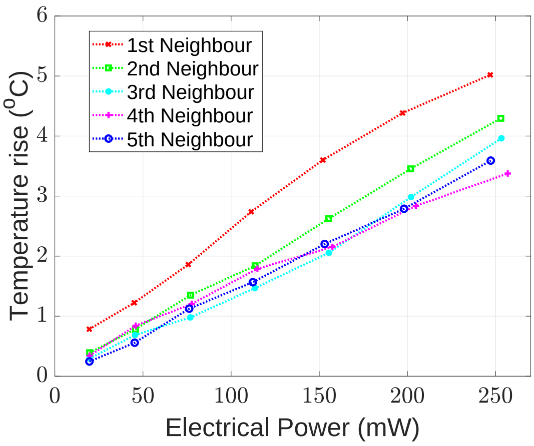

Figure 5.9: Temperature rise in a device as a function of the injected electrical power in neighbouring devices

We can infer from the slopes of the plots in Figure 5.9 that the thermal cross talk varies from 18.6^{o}C per Watt of electrical power injected 500μm away, to 12.8^{o}C/W injected 2500μm away. This information is useful for designing devices in the future with better thermal performance without having to sacrifice power consumption by adjusting TEC in the device packaging to achieve thermal stability.

5.3 Optical Crosstalk

As seen in the previous chapter, especially from Figures 4.19 and 4.20, optical crosstalk was shown to affect the performance of the wavelength monitor when it was integrated with a laser on the same chip. To investigate the consequences of light from the laser not being waveguided into the wavelength monitor, experiments were carried out where light from an external laser source was coupled into a standalone wavelength monitor using lensed fibre and deliberately misaligned to its input facet.

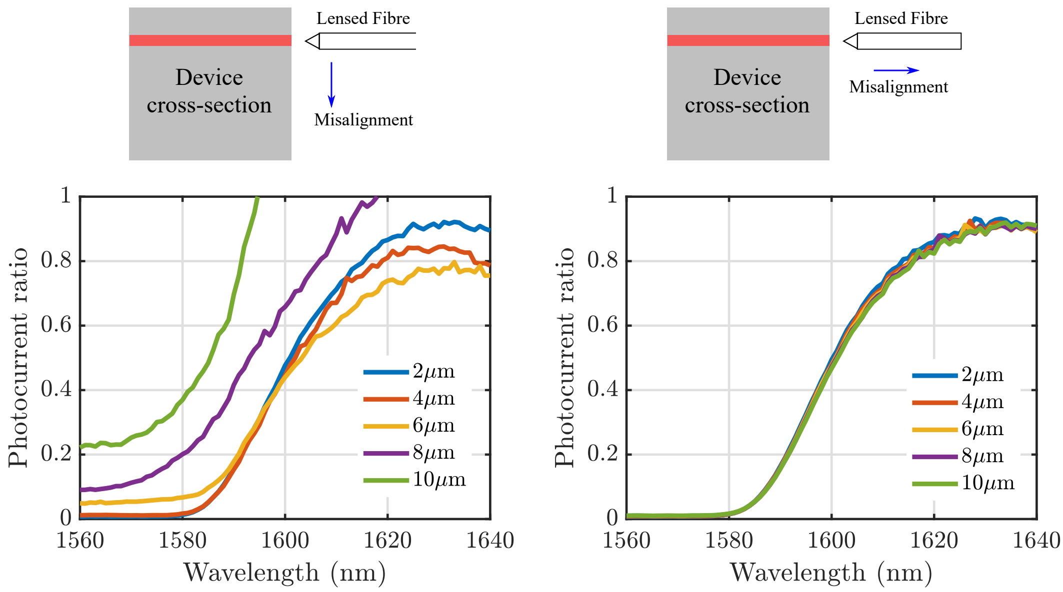

(a) (b)

Figure 5.10: Photocurrent ratio in the wavelength monitor with the input misaligned (a) into the substrate (Z-axis) and (b) away from the facet (X-axis)

The results are shown in Figure 5.10. We observe that when the fibre is misaligned to the substrate the photocurrent ratio, and thus the performance of the wavelength monitor is affected drastically. On the other hand, when the fibre is misaligned by moving it longitudinally away from the facet, the performance remains unaffected. This shows that while designing an integrated version, if the light from the laser has a path into the substrate, the wavelength monitor ceases to function well. In order to get rid of substrate leakage in the integrated device we had tested an epitaxial structure (called A1779) with a 1 μm thick InGaAs layer underneath the active MQW core layers. The integrated wavelength monitor showed considerably better performance than those on the IQE wafer (Figure 4.21).

To verify that substrate leakage is indeed the cause of this unwanted behaviour, the lasing facet was imaged using an infrared camera as shown in Figure 5.11. The lasing power and the camera parameters were kept constant between the images. We observe a glow from the bottom of the n-substrate in the IQE wafer in Figure 5.11(a). This glow was consistently observed in all designs on the IQE wafer. On the other hand, in Figure 5.11(b), there is no glow from the substrate for a device on A1779. This proves that the InGaAs layer is very helpful and essential in mitigating optical leakage to the substrate, and hence optical crosstalk between the laser and the wavelength monitor sections.

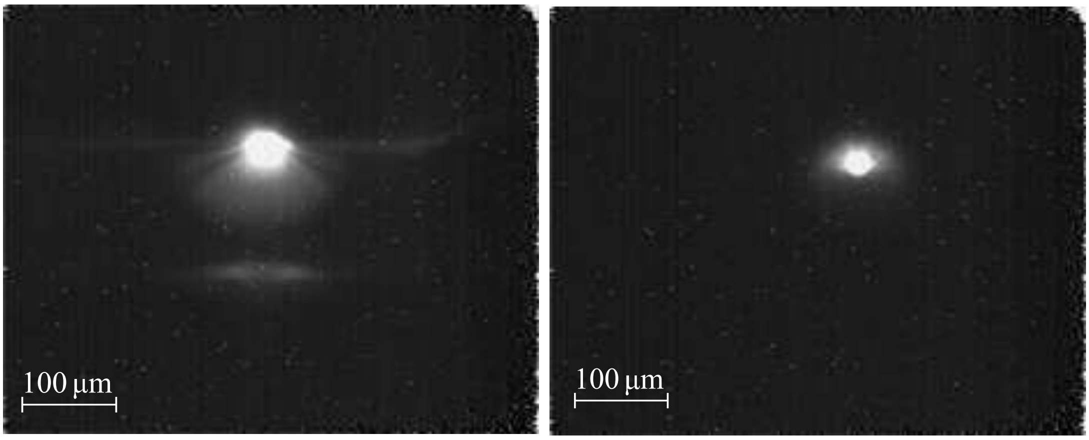

(a) (b)

Figure 5.11: Infrared camera image of the lasing facet of an integrated device on (a) IQE wafer (b) A1779 wafer

In the previous chapter, an integrated laser and wavelength monitor on A1779 wafer was demonstrated to match the results from a standalone wavelength monitor for wavelength channels on the lower end of the spectrum (Figure4.21). There appear to be no points on the longer wavelength end mainly because of the fact that the material becomes more and more transparent for higher wavelengths, and the integrated laser is unable to provide wavelengths on the higher side of the wavelength monitor's photocurrent ratio curve. To prove the concept that if the integrated laser were able to lase at longer wavelengths, the integrated wavelength monitor should still work efficiently, an experiment was carried out where light from an external laser source was injected, not directly into the wavelength monitor (as before), but instead into the laser output facet. So, for a device like the one shown in Figure 4.14 (a), light is injected from the left facet. In order for this light to be able to reach the wavelength monitor on the other end of the laser, the three sections of the laser and biased just up to transparency. The photocurrents in the wavelength monitor are now measured and the ratio is plotted in Figure 5.12 as a blue dotted line. For quick reference, the expected curve from a standalone wavelength monitor where the light is directly injected into it, is plotted as a dashed grey line.

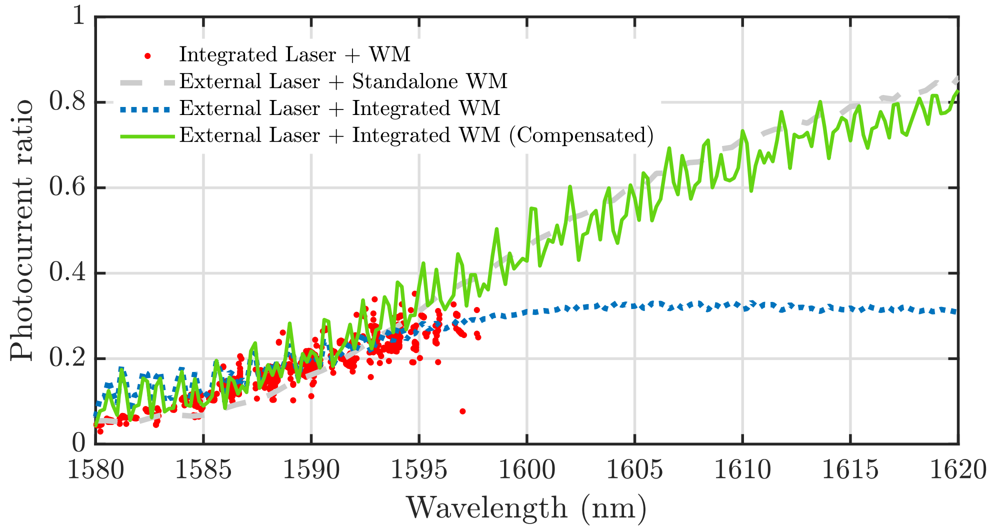

Figure 5.12: Photocurrent ratio versus wavelength plot for an integrated WM with external injection into the integrated laser sections (biased to transparency)

We observe that these two curves do not match up as they should. Since the injection of light via the laser facet involves a small bias current to achieve transparency, the photocurrents generated in the wavelength monitor sections only due to this bias was noted keeping the external laser source turned off. When we subtract these photocurrents, caused due to spontaneous emission from the laser section, from the photocurrents obtained on external injection and then calculate the ratio, we obtain the solid green curve in Figure 5.12. This shows good agreement with the curve obtained from direct external injection into the standalone wavelength monitor. From this experimental result we can confirm that the integrated laser and wavelength monitor can work for the entire wavelength range, provided the laser can lase at all the wavelength channels (a way to achieve this would be using quantum well intermixing [6, 7])

5.4 Summary

In this chapter, three kinds of crosstalks were studied - electrical, thermal and optical - within the context of the integrated transmitter device discussed in this thesis.

A slot along the waveguide provides a kew kΩ's of electrical isolation between the sections that divides the waveguide into. This isolation is not enough to have between the laser and a wavelength monitor since the photocurrent readouts are very sensitive to electrical crosstalk. It was observed that a deeply etched trench between the laser and the wavelength monitor (and all around the device making sure to p-to-p conduction path remains) of about 5μm deep results in an electrical isolation of about 10MΩ. It can be concluded that this trench is necessary for the integration of the wavelength monitor design described in this thesis work.

From experiments on thermal crosstalk, it was determined that the wavelength of the laser shifts by about 0.1nm/^{o}C. And for every mW of electrical power injected 500μm away from a device, its temperature rises by about 0.018^{o}C. Although the effects of this type of thermal heating due to drive currents can be mitigated by the use of a TEC inside the package for the integrated device, it can be very useful to design the photonic chip in such a way that the power consumption of the TEC can be minimised. This is very beneficial especially in commercial applications with very strict specifications for power consumption of a packaged optical device.

In order to make conclusive remarks on optical crosstalk, measurements were made by injecting light through a lensed fibre intentionally misaligned with the device facet. From these measurements, it is inferred that injecting light into the waveguide of the wavelength monitor is crucial, although the power of this injected light is not very crucial. On an IQE wafer the light from the on-chip laser was leaking into the substrate at the interface to the wavelength monitor which was confirmed by infrared camera images. An epitaxial structure with 1μm thick InGaAs underneath the active MQW layers got rid of this problem because of the absorptive properties of InGaAs. The infrared images on this wafer confirmed that no light was leaking into the substrate. This was further proved by externally injecting light into the on-chip laser sections having them biased on transparency and providing a path for the external light to reach the on-chip wavelength monitor. In this case, the integrated wavelength monitor was shown to work as good as a standalone wavelength monitor. There are opportunities for making this performance even better with less noise in the wavelength monitor readouts. The following chapter presents some directions for future work along these lines.

References

[1] M. K. Smit, "New focusing and dispersive planar component based on an optical phased array," *Electronics Letters*, vol. 24, pp. 385–386, March 1988.

[2] L. A. Coldren, S. C. Nicholes, L. Johansson, S. Ristic, R. S. Guzzon, E. J. Norberg, and U. Krishnamachari, "High Performance InP-Based Photonic ICs—A Tutorial," *J. Lightwave Technol.*, vol. 29, pp. 554–570, Feb 2011.

[3] U. Koren, T. L. Koch, B. I. Miller, G. Eisenstein, and R. H. Bosworth, "Wavelength division multiplexing light source with integrated quantum well tunable lasers and optical amplifiers," *Applied Physics Letters*, vol. 54, no. 21, pp. 2056–2058, 1989.

[4] S. W. Corzine, P. Evans, M. Fisher, J. Gheorma, M. Kato, V. Dominic, P. Samra, A. Nilsson, J. Rahn, I. Lyubomirsky, A. Dentai, P. Studenkov, M. Missey, D. Lambert, A. Spannagel, R. Muthiah, R. Salvatore, S. Murthy, E. Strzelecka, J. L. Pleumeekers, A. Chen, R. Schneider, R. Nagarajan, M. Ziari, J. Stewart, C. H. Joyner, F. Kish, and D. F. Welch, "Large-Scale InP Transmitter PICs for PM-DQPSK Fiber Transmission Systems," *IEEE Photonics Technology Letters*, vol. 22, pp. 1015–1017, July 2010.

[5] R. Stabile, A. Albores-Mejia, and K. A. Williams, "Monolithic active-passive 16x16 optoelectronic switch," *Opt. Lett.*, vol. 37, pp. 4666–4668, Nov 2012.

[6] K.-H. Lee, K. Thomas, A. Gocalinska, M. Manganaro, E. Pelucchi, F. H. Peters, and B. Corbett, "SiNx-induced intermixing in AlInGaAs/InP quantum well through interdiffusion of group III atoms," *Journal of Applied Physics*, vol. 112, no. 9, p. 093109, 2012.

[7] S. Shen, G. Li, Z. Lin, C. Lee, and Y. Chiu, "Power-enhancement broadband cascaded integration of electroabsorption modulator and semiconductor optical amplifier by local quantum well intermixing," in *2014 IEEE Photonics Conference*, pp. 278–279, Oct 2014.

Chapter 6

Conclusions and Future Work

This chapter presents a summary of key conclusions drawn in this thesis. Some results from the use of the devices discussed in this thesis in real world telecommunication systems are highlighted in order to put the work in a practical context. Finally, areas for future work are discussed.

6.1 Summary of Results

Tuneable lasers will be a key requirement in transmitter modules of next generation optical communication networks for data transmission in the upstream direction. The lasers need to be wavelength-stabilised and cost is a critical factor since they will be widely used in consumer products. In **Chapter 1**, the state-of-art of tuneable transmitter modules were presented and the a motivation for this thesis work was established on the fact that currently used tuneable lasers in the downstream direction are too expensive for widespread use in consumer products, and current designs for integrated wavelength monitors use passive waveguides made using spatially selective bandgap engineering techniques which are not cost-effective and make integration with a laser challenging.

This thesis demonstrates a low-cost tuneable transmitter module using a slotted Fabry-Pérot laser, monolithically integrated with a modulator, wavelength monitor and a semiconductor optical amplifier (SOA). In **Chapter 2**, a 3-section tuneable slotted Fabry-Pérot design was presented which had a discrete tuning range of about 20nm which covers half the C-band. The wavelength channels obtained from this laser can be further fine-tuned by adjusting the temperature between 16-22^{0}C with a sensitivity of approximately 0.1nm/^{0}C. The theory behind slotted Fabry-Pérot lasers was presented explaining the benefits of a multi quantum well layer structure to obtain good optical gain and waveguiding, and how slots along the waveguide introduce reflections that aid in longitudinal mode selection. A time-domain travelling wave model was presented that can simulate the behaviour of slotted lasers. The steps involved in the fabrication of the device were presented in detail. In **Chapter 3** a design for a 2-section wavelength monitor was presented which shared a very similar geometry to that of the laser. The theory behind its operation was outlined along with a simulation of the expected photoresponse which matched experimental results. Using the wavelength monitor in a PID control loop to monitor and stablise the wavelength of a 3-section tuneable slotted Fabry-Pérot laser. The accuracy of stabilisation is within 15 GHz in frequency around a wavelength of 1550nm. The accuracy and time needed for stablisation can be improved greatly by using custom on-board electronics in place of laboratory equipment and automation software used to prove the concept in this thesis.

Monolithic integration of the laser and the wavelength monitor along with a modulator and an SOA was presented in **Chapter 4**. The modulator is an absorbing section with Ground-Signal-Ground (GSG) pads that was shown experimentally to be capable of delivering data rates of up to 10 Gb/s with a peak-to-peak driving voltage of 1V using Non-return-to-zero on-off-keying (NRZ-OOK) modulation. The modulator showed an extinction ratio of about 8-10dB, 3dB-bandwidth in the small-signal frequency response of about 6GHz and a clean eye diagram up to speeds of at least 10 Gb/s. It was shown that an angled deep etch separation was needed for wavelength-stable operation of the modulator. The SOA booster section was shown to be able to provide an optical gain/attenuation range of 20dB for a drive current range of 30mA. Results from the integrated wavelength monitor showed that on an IQE wafer, the device suffered from possibly heavy optical crosstalk between the laser and the wavelength monitor sections. A proposed solution would be to use an absorbing layer underneath the active MQW layer to get rid of parasitic reflections resulting from possible light leaking into the substrate at the location of the deep etches. All of these different optical components employ the same epitaxial structure as the tuneable laser, thus requiring no regrowth, making monolithic integration easily achievable. Along with the fact that the slots required for tuning of the laser are fabricated in the same step as the ridge waveguide, presenting no additional complexity during the fabrication process, makes the whole transmitter module low-cost and compatible for use in Optical Network Units (ONUs) in the consumers' premises in a Fibre-to-the-Home (FTTH) scenario. In **Chapter 5** we explored the challenges of integration such as electrical, optical and thermal crosstalk between the various active components within a single device and suggested design rules that will help mitigate this crosstalk such as having a deep isolation etch of at least 5μm depth between the laser and the wavelength monitor section, which increases the p-to-p resistance from a few kΩ to about 10MΩ. Furthermore, a 7^0 angled etch between the laser and the modulator sections reduces the back reflections mitigating the optical crosstalk between the two components. It is also concluded that injecting light into the waveguide of the wavelength monitor is crucial, although the power of this injected light is not very crucial. On an IQE wafer the light from the on-chip laser was leaking into the substrate at the interface to the wavelength monitor which was confirmed by infrared camera images. An epitaxial structure with 1μm thick InGaAs underneath the active MQW layers got rid of this problem because of the absorptive properties of InGaAs. The infrared images on this wafer confirmed that no light was leaking into the substrate. This was further proved by externally injecting light into the on-chip laser sections having them biased on transparency and providing a path for the external light to reach the on-chip wavelength monitor. In this case, the integrated wavelength monitor was shown to work as good as a standalone wavelength monitor.

6.2 Future Work

To obtain all the wavelength channels from the integrated laser, the three tuning currents along with the chip temperature need to be controlled. Since the performance of other optical components on the same chip also rely on the chip temperature, it could be very useful to control the temperature of the laser locally using microheaters. Initial tests were carried out using chromium heating strips near ridge waveguides and measuring the temperature change in the ridge by Fabry-Pérot transmission measurements as illustrated in Figure 6.1. It was observed that a 6^{o}C change in ridge temperature can be brought about using a heater power of about 20mW. The designs can be optimised further and could result in a less complicated tuning map for the slotted Fabry-Pérot laser.

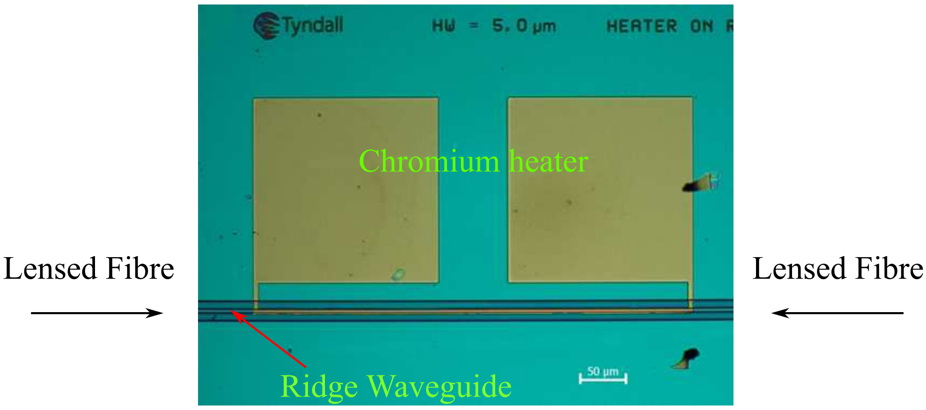

Figure 6.1: Chromium heater adjacent to ridge waveguide for localised heating testing

Another possible avenue of future work is using quantum well intermixing to selectively alter the bandgap of certain areas on the wafer [1, 2]. This can lead to the laser lasing at longer wavelengths, and also covering a wider tuning range, for example the whole C-band. Wide tuneability at low-cost is a hot topic of interest in the commercial market. In addition to increasing the tuning range of the laser, this could also lead to a better performance of the modulator by decreasing its insertion loss significantly. Introducing high-k dielectrics like BCB under the RF contact pads should also boost the speed of the modulator by lowering its capacitance [3].

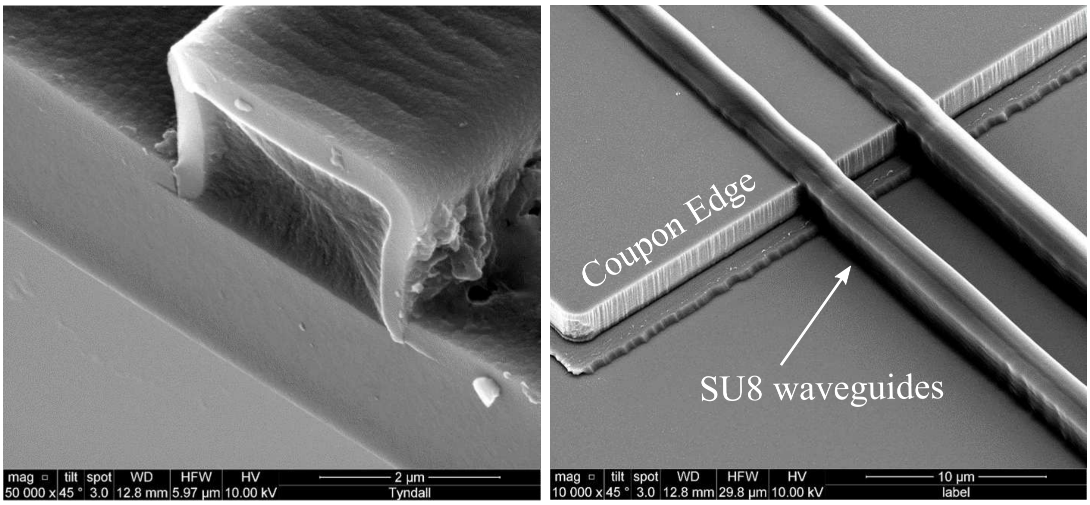

(a) (b)

Figure 6.2: SEM image of (a) cross-section of an SU8 waveguide and (b) the edge of a transfer-printed coupon with SU8 waveguide over it. SEM images credit: James O'Callaghan

To eliminate optical crosstalk due to leakage of light into the substrate completely, a very interesting approach could be to use micro-transfer-printing[4]. After fabrication, the common substrate could be stripped off from underneath the entire device and the various components could be 'printed' separately on other substrates and optically connected via passive waveguides made from a polymers like SU8 or on a platform like Silicon-on-Insulator for making silicon photonics chips. Some preliminary experiments were carried out as part of this thesis work by defining SU8 waveguides and observe their conformity going over transfer-printed coupons. These SEM images are shown in Figure 6.2.

All the discussion above was at device level. To put this device in context, some results from measurements at systems-level carried out at the Photonics Systems Group (PSG) by Daniel Carey *et al* are presented below. As part of this thesis work, an open eye-diagram at 10Gb/s was demonstrated in Chapter 4 directly from the device (back-to-back). But to place the device in a real-world setting, bit-error-rate measurements were carried out at the PSG lab using upto 50km of fibre transmission length. From these measurements plotted in Figure 6.3, it can be seen that the device is capable of achieving error-free transmission up to a distance of 50km [5].

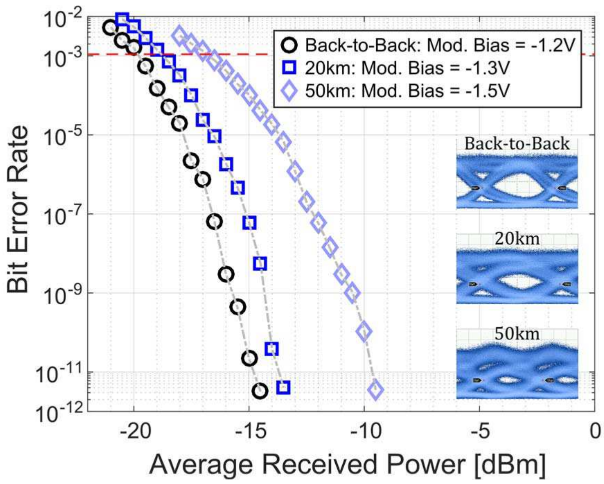

Figure 6.3: Transmission performance comparison at 1557.37nm [5]

One of the many associated costs during the production of an optical device can be attributed to calibration. This can be reduced using the following scheme: upon purchase and setup, the laser is first coarsely calibrated offline by the consumer by generating an internal look-up table for the wavelength monitor. Then the device is connected to the network, and a downstream reference signal can be used to match the internal calibration to an absolute wavelength reference provided by the network. Additionally, measurement of the linewidth of the laser could be a potential next step in the characterisation of this device. Optimisation of the linewidth has the potential to open up the possibilities of application of this device beyond optical telecommunications.

Low-cost tuneable optical transceivers have become a sought-after entity for next-gen telecom networks. Thus, in conclusion, any work towards packaging this device into a wavelength-stabilised tuneable transmitter module is a future avenue worth pursuing.

References

[1] K.-H. Lee, K. Thomas, A. Gocalinska, M. Manganaro, E. Pelucchi, F. H. Peters, and B. Corbett, "SiNx-induced intermixing in AlInGaAs/InP quantum well through interdiffusion of group III atoms," *Journal of Applied Physics*, vol. 112, no. 9, p. 093109, 2012.

[2] S. Shen, G. Li, Z. Lin, C. Lee, and Y. Chiu, "Power-enhancement broadband cascaded integration of electroabsorption modulator and semiconductor optical amplifier by local quantum well intermixing," in *2014 IEEE Photonics Conference*, pp. 278–279, Oct 2014.

[3] Y. Cheng, J. Pan, Y. Wang, F. Zhou, B. Wang, L. Zhao, H. Zhu, and W. Wang, "40-Gb/s Low Chirp Electroabsorption Modulator Integrated With DFB Laser," *IEEE Photonics Technology Letters*, vol. 21, pp. 356–358, March 2009.

[4] R. Loi, J. O'Callaghan, B. Roycroft, C. Robert, A. Fecioru, A. J. Trindade, A. Gocalinska, E. Pelucchi, C. A. Bower, and B. Corbett, "Transfer Printing of AlGaInAs/InP Etched Facet Lasers to Si Substrates," *IEEE Photonics Journal*, vol. 8, no. 6, pp. 1–10, 2016.

[5] D. Carey, P. Ramaswamy, G. Talli, C. Antony, B. Roycroft, B. Corbett, and P. D. Townsend, "Characterization of a Low-Cost, Monolithically Integrated, Tunable 10G Transmitter for Wavelength Agile PONs," *IEEE Journal of Quantum Electronics*, vol. 54, pp. 1–12, Dec 2018.

Appendix A

Epitaxial Structures

Layer	Material	Thickness (nm)	Doping level (cm^{-3})	Dopant	Comment
26	InGaAs	40	>$1x10^{19}$	Zn	
25	InGaAs	80	~$1x10^{19}$	Zn	
24	InP	1500	~$1x10^{18}$	Zn	
23	InGaAsP	6	~$5x10^{17}$	Zn	
22	InP	40	~$1x10^{17}$	Zn	
21	CIL (InGaAs)	(2-5)			Minimal thickness
20	$(Al_{.9}Ga_{.1})_{.47}In_{.53}As$	40			
19	$(Al_{.7}Ga_{.3})_{.47}In_{.53}As$	75			
8 x 6	$(Al_{.45}Ga_{.65})_{.51}In_{.49}As$	10			Tensile strained barrier ~-0.3%
7 x 6	$(Al_{.25}Ga_{.75})_{.3}In_{.7}As$	6			Compressive strained quantum well ~1.1%
6	$(Al_{.45}Ga_{.65})_{.51}In_{.49}As$	10			Tensile strained barrier~-0.3%
5	$(Al_{.7}Ga_{.3})_{.47}In_{.53}As$	75			
4	$(Al_{.9}Ga_{.1})_{.47}In_{.53}As$	40	$1x10^{18}$	Si	
3	InP	1500	$1x10^{18}$	Si	Lower cladding
2	InGaAs	1000	~$1x10^{18}$	Si	Etch release layer
1	InP	100	$1x10^{18}$	Si	buffer
	InP substrate			N-type	

Figure A.1: Epitaxial structure of laser material - A1779

Table A.1: Epitaxial structure of laser material from IQE

Material	x	y	Strain (ppm)	PL (nm)	Thickness (μm)	Dopant	Doping level (cm^{-3})
GaIn$_x$As	0.53				0.2	Zinc	$>1.5\times10^{19}$
GaIn$_x$As$_y$P	0.71	0.62		1300	0.05	Zinc	$>3.0\times10^{18}$
InP					1.6	Zinc	$>1.5\times10^{18}$
GaIn$_x$As$_y$P	0.85	0.33		1100	0.02	Zinc	$=1.0\times10^{18}$
InP					0.05	Zinc	$=7.0\times10^{17}$
Al$_x$GaIn$_y$As	0.90	0.53			0.06	Zinc	$=4.0\times10^{17}$
Al$_x$GaIn$_y$As	0.90-0.72	0.53			0.06	Undoped	
Al$_x$GaIn$_y$As	0.44	0.49	-3000	1100	0.01	Undoped	
Al$_x$GaIn$_y$As x5	0.24	0.71	12000	1530	0.006	Undoped	
Al$_x$GaIn$_y$As x5	0.44	0.49	-3000	1100	0.01	Undoped	
Al$_x$GaIn$_y$As	0.72-0.90	0.53			0.06	Undoped	
Al$_x$GaIn$_y$As	0.90	0.53			0.06	Silicon	$=1.0\times10^{18}$
Al$_x$GaIn$_y$As	0.90-0.86	0.53			0.01	Silicon	$=1.0\times10^{18}$
InP					$\sim$ 400	Silicon	$=3.0\times10^{18}$

Appendix B

Fabrication Sequence

Abbreviations and names used in this section:

BOE	Buffered Oxide Etch
DI	De-Ionised water
DUV	Deep Ultra-violet
ESL	Etch Stop Layer
EBR	Edge Bead Removal
HMDS	HexaMethylDiSilazane
ICP	Inductively-coupled Plasma
LOR	Lift-off resist
PECVD	Plasma-enhanced Chemical Vapour Deposition
SEM	Scanning Electron Microscope
TCE	Trichloroethylene
TLM	Tranmission Line Measurements

B.1 Level 1: Ridge Metal Deposition

Overview

This is to establish the p contacts for the lasers. They are deposited first so as to minimize contact resistance.

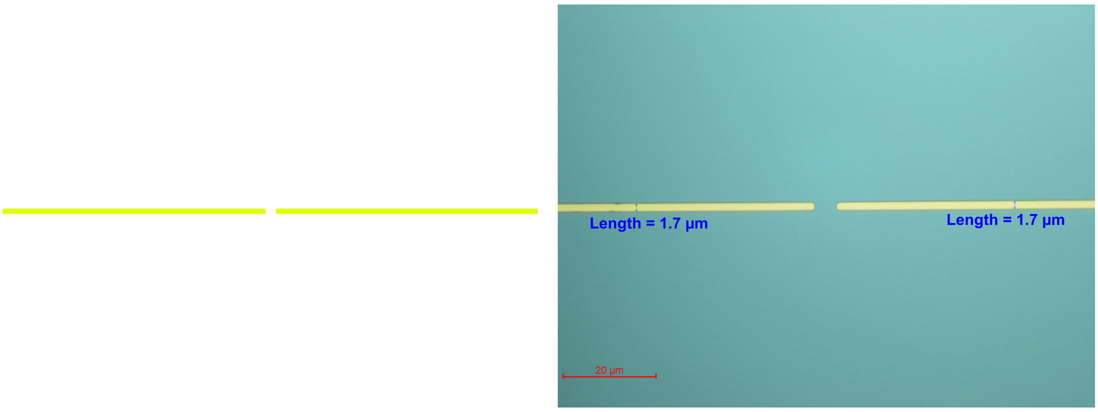

Spin and prep

- Clean mask Dehydrate bake on hotplate 200°C for 10 min
- Spin on HMDS at 4000 rpm 50s
- Spin on LOR10A at 4000 rpm 50s
- Hotplate 150ºC for 3 mins
- EBR
- Spin on HMDS at 4000 rpm 50s
- Spin on S1805 at 4000rpm 50s
- EBR
- Hotplate 115ºC for 120s

Lithography

- Expose mask level 1 using MA6 UV mode using leveling pieces Contact – Vacuum, Pre vac 5s, Full vac 10s. Exposure time – 12s. Align perp. to major flat (CRITICAL DIMENSION – 1.5μm CRITICAL MISALIGNMENT - N/A)

- Develop for 75s in MF319
- Rinse DI 30s
- Blow dry N_2
- Post Bake 90°C 30 minutes in oven
- Inspect Quality
- Record images

Metal Deposition

- Dip in BOE:DI 1:10 for 10s
- Rinse DI 30s
- Blow dry N_2 30s
- Load for a flat evaporation - 10nm Ti and 110nm Au
- Unload and Lift off in 1165 solvent at 90°C – leave for 30 minutes
- Rinse DI 30s
- Blow dry N_2
- Inspect Quality
- Record images

B.2 Level 2: Ridge Lithography and Etch

Overview

This is to establish ridge waveguide and slots for mode control of the laser.

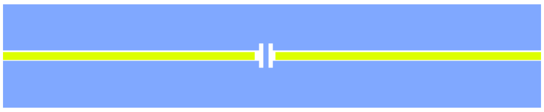

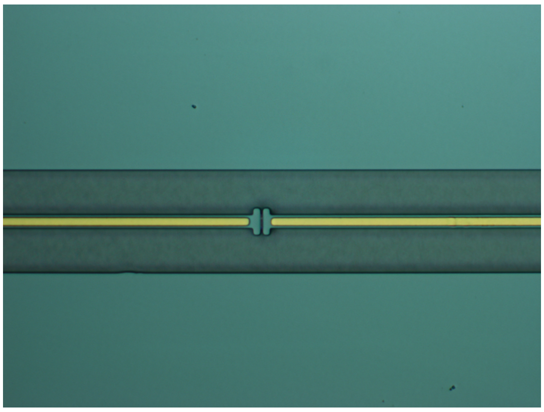

Hard mask deposition

- Hard Mask Deposition Deposit 100nm SiO_2 PECVD and 400nm SiO_2 via sputter on Oxford sputterer using OxideStandard recipe. Include two Si Monitor pieces.
- Note down Job number, Deposition Time, and Actual thickness.

Spin and prep

- Clean mask
- Dehydrate bake on hotplate 200°C for 10 min.
- Spin on HMDS at 4000 rpm 60s
- Spin on UV26 at Dynamic Spin J 1000rpm 20s, 3000rpm 10s, 4000rpm 20s
- EBR
- Hotplate 130°C for 60s

Lithography

- Expose mask level 2 using MA6 DUV mode using leveling pieces Contact – Vacuum, Pre vac 5s, Full vac 10s, Exposure time – 12s CRITICAL DIMEN-

SION – 0.8μm CRITICAL MISALIGNMENT – 0.5μm

- Post Exposure Bake (PEB) at 110°C for 60s
- Develop for 25s in MF CD26
- Rinse DI 30s
- Blow dry N_2
- Inspect Quality
- Record images

Hard Mask Etch

- ICP Machine: STS Chemistry:CF4:CHF3 recipe OXIDEETCH.rec. Record Carousel no., Etch time, Etch rate.
- O_2 plasma 100W 10 minutes
- Remove resist 1165 solvent at 90°C – leave for 30 minutes
- Rinse DI 30s
- Blow dry N_2
- O_2 plasma 100W 5 minutes
- Tencor step height - Record file
- Inspect Quality
- Record images

Material Etch

- ICP Machine: Oxford Target Depth 1.6μm Chemistry: $Cl_2/CH_4/H_2$ YH recipe etch. Record Etch time, Etch rate.
- Tencor step height - Record file
- Inspect Quality
- Record images

Material Wet Etch

- Etch InP to InGaAsP ESL cap layer in 1:4 H_3PO_4:HCl Depth 1.85μm
- Rinse DI 30s
- Blow dry N_2
- Tencor step height - Record file
- Inspect Quality
- Record images
- SEM inspection to ensure the slots are fully etched.
- Record images

Ridge Hard Mask Removal

- ICP Machine: STS Chemistry:CF_4:CHF_3 recipe OXIDEETCH.rec. Record Carousel no., Etch time, Etch rate.
- Tencor step height - Record file
- Inspect Quality
- Record images
- Test TLM

B.3 Level 3: Facet Lithography and Etch

Overview

This is to form the etched facet of the lasers. The quality of the facet etch is paramount as it will have a significant impact on the performance of the device. After the facet etch the remaining hard mask should be approximately 200nm thick and should be measured very accurately for further etches. This remaining hard mask acts as the sidewall passivation for the p-contacts.

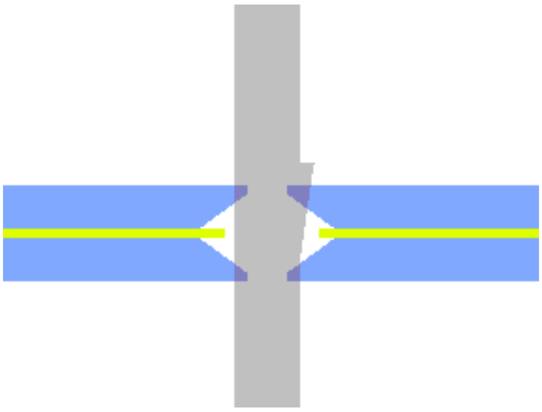

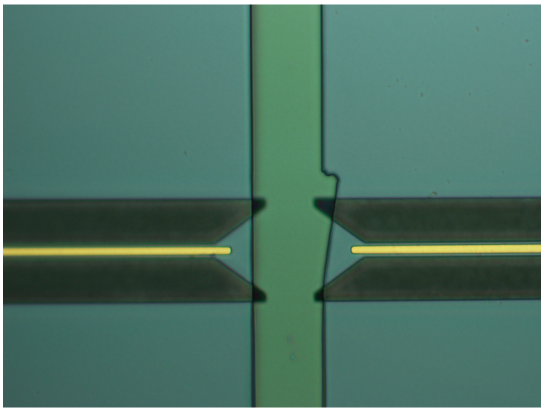

Hard Mask Deposition

- Deposit 100nm SiO_2 via Sputter on Oxford sputterer using OxideStandard recipe. Include two Si Monitor pieces. Record Job number, Deposition Time, Actual thickness
- Deposit 500nm SiNx via PEVCD MFSIN recipe. Include two Si Monitor pieces. Record Job number Deposition Time Actual thickness.

Spin and prep

- Clean mask
- Spin on HMDS 4500 rpm 30s
- Spin AZ5214E 4500 rpm 50s
- Hotplate 110°C 90s

Lithography

- Expose mask level 3 using MA6 UV mode using leveling pieces Contact – Vacuum, Pre vac 5s, Full vac 10s, Exposure time – 16s
  CRITICAL DIMENSION – 50μm CRITICAL MISALIGNMENT – 1μm
- Develop for 27s in AZ400K:DI 1:4
- Rinse DI 30s
- Blow dry N_2
- Inspect Quality
- Record images

Hard Mask Etch

- ICP Machine: STS Chemistry:CF_4:CHF_3 recipe OXIDEETCH.rec. Record Carousel no., Etch time, Etch rate.
- O_2 plasma 100W 5minutes in PICO asher
- Remove resist 1165 solvent at 90°C – leave for 30 minutes
- Rinse DI 30s
- Blow dry N_2
- O_2 plasma 100W 5minutes in PICO asher
- Tencor step height - Record file
- Inspect Quality
- Record images

Material Etch

- ICP Machine: Oxford Target Depth 5.0μm Chemistry: $Cl_2/CH_4/H_2$ JOC EF recipe etch. Record Etch time, Etch rate.
- Tencor step height - Record file
- Inspect Quality
- Record images
- SEM inspection to ensure quality of etched facet.

- Record images

Ridge Hard Mask Removal

- ICP Machine: STS Chemistry:CF_4:CHF_3 recipe OXIDEETCH.rec. Record Carousel no., Etch time, Etch rate
- Tencor step height - Record file
- Inspect Quality
- Record images
- Test TLM

Oxide Planarisation

The purpose of this is to straighten to sidewalls so that there will not be a break in the metal when to bondpads are applied. It acts as a rudimentary form of planarization

- Deposit 1500nm SiO_2 via PECVD recipe HFSIO.rec. Include two Si Monitor pieces. Record Job number, Deposition Time, Actual thickness.

Oxide Etch Back

- ICP Machine: STS Chemistry:CF_4:CHF_3 recipe OXIDEETCH.rec. Record Carousel no., Etch time, Etch rate
- Etch back to 650nm on Wafer top surface
- Tencor step height - Record file
- Inspect Quality
- Record images
- Test TLM

B.4 Level 4: Open Oxide Lithography and Etch

Overview

This is to open the contacts on the top of the ridge so as that the p-contacts can be formed when the bondpads are deposited.

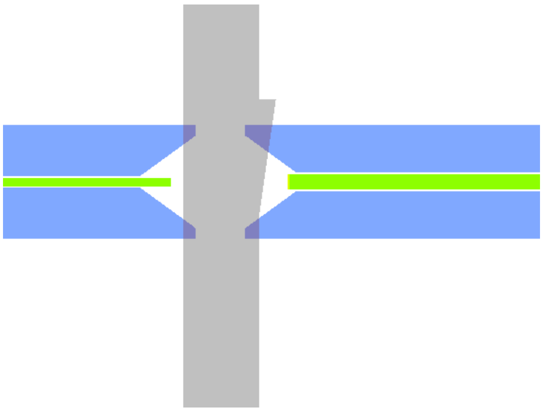
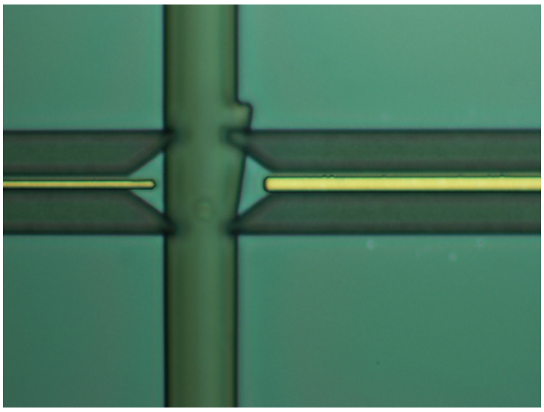

Spin and prep

- Spin on HMDS at 4000rpm 50 sec
- Spin on S1813 at 4000rpm 50 sec
- Hotplate 115°C for 2 mins
- EBR

Lithography

- Expose mask level 4 using MA6 UV mode using leveling pieces Contact – Vacuum, Pre vac 5s, Full vac 10s, Exposure time – 14s, CRITICAL DIMENSION – 2.5μm CRITICAL MISALIGNMENT – 0.5μm
- Develop for 25s MF319
- Rinse DI 30s
- Blow dry N_2
- Inspect Quality
- Record images

Open Oxide Etch

- ICP Machine: STS Chemistry:CF_4:CHF_3 recipe OXIDEETCH.rec etch until 20nm of SiO_2 remains. Record Carousel no., Etch time, Etch rate
- O_2 plasma 50W 2 in PICO asher
- Remove resist 1165 solvent at 90°C – leave for 30 minutes
- Rinse DI 30s
- Blow dry N_2
- Tencor step height - Record file
- Inspect Quality
- Record images

B.5 Level 5: P-Contact Lithography and Metal Deposition

Overview

This is to form the p-contact bondpads for the laser

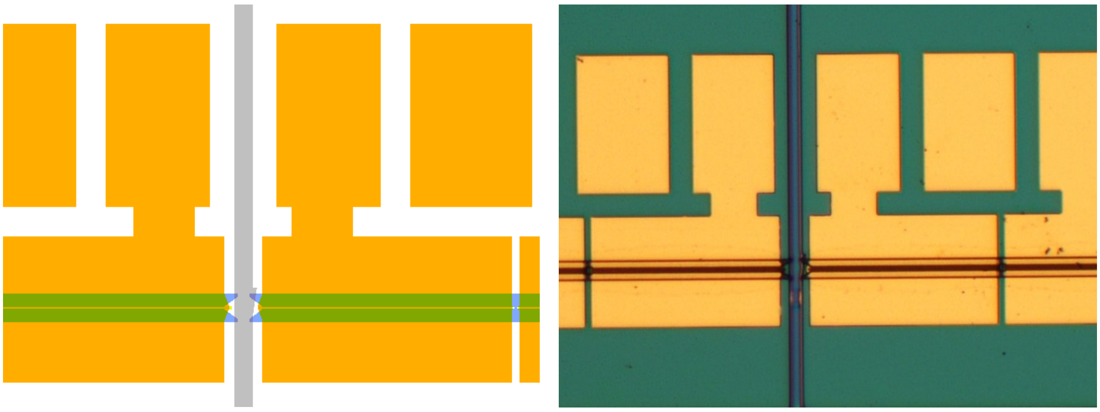

Spin and prep

- Clean mask
- Dehydrate bake on hotplate 200°C for 10 min
- Spin on HMDS at 4000 rpm 50s
- Spin on LOR10A at 4000 rpm 50s
- Hotplate 150°C for 3 mins
- EBR
- Spin on HMDS at 4000 rpm 50s
- Spin on S1813 at 4000rpm 50s
- EBR
- Hotplate 115°C for 120s

Lithography

- Expose mask level 5 using MA6 UV mode using leveling pieces Contact – Vacuum, Pre vac 5s, Full vac 10s, Exposure time – 14s
  CRITICAL DIMENSION – 5μm CRITICAL MISALIGNMENT – 2μm

- Develop for 90s in MF319
- Rinse DI 30s
- Blow dry N_2
- Post Bake 90^{o}C 30 minutes in oven
- Inspect Quality
- Record images

Metal Deposition

- Dip in BOE:DI 1:7 for Until oxide would be over-etched by 30%
- Rinse DI 30s
- Blow dry N_2 30s
- Load for an angled evaporation in the 360^o rotation tool - 10nm Ti Au340nm
- Unload and Lift off in 1165 solvent at 90^{o}C – leave for 30 minutes
- Rinse DI 30s
- Blow dry N_2
- Inspect Quality
- Record images

B.6 Final Step: Substrate Thinning and N-Metal Deposition

Substrate thinning

- Target thickness for thinned chip is 120μm
- Measure starting thickness of chip
- Glue to glass carrier with black wax epitaxial side down (no gaps)
- Measure thickness of chip when adhered to glass carrier
- Thin with bromine methanol

Deposition of n-contacts

- Surface preparation dip – HCl:DI 1:10 for 20s
- Rinse in DI
- Blow dry N_2
- Load as quickly as possible Evaporate n contact - Au:Ge:Au:Ni:Au (14:14:14:10:150nm)
- Remove from carrier and clean in TCE